UNIVERSITY OF CALIFORNIA
SANTA CRUZ

Nonthermal Emission from Galaxy Clusters

A dissertation submitted in partial satisfaction of the
requirements for the degree of

DOCTOR OF PHILOSOPHY

in

PHYSICS

by

Emma Storm

June 2015

This dissertation of Emma Storm is approved:

Professor Stefano Profumo, Chair

Professor Tesla Jeltema, Advisor

Professor Steve Ritz

Tyrus Miller
Vice Provost and Dean of Graduate Studies

Contents

List of Figures

List of Tables

Abstract

Nonthermal Emission from Galaxy Clusters

by

Emma Storm

Galaxy clusters are the most massive gravitationally-bound objects in the universe. The bulk of the mass in a cluster is dark matter, while the dominant baryonic component is a thermal, X-ray emitting plasma. Radio observations of diffuse synchrotron emission indicate that galaxy clusters host a population of cosmic rays; however, the nature of this nonthermal component is not well-understood. In this dissertation, I investigate three sources of nonthermal emission in galaxy clusters. The first is star formation in galaxies, which is correlated to gamma-ray emission. I derive lower limits on the gamma-ray emission for nearby clusters by considering the emission from star formation in cluster galaxies. These lower limits sit about an order of magnitude below current upper limits on gamma rays in clusters and will be an important contributor to gamma-ray emission as upper limits improve over time. Dark matter annihilation, which produces relativistic particles that can result in a broad spectrum of emission in cluster environments, is another source of nonthermal emission. I use nondetections and marginal detections of diffuse radio emission in clusters to constrain dark matter annihilation. I derive limits on the annihilation cross section that are competitive with limits from the nondetection of gamma rays in clusters and show that the best objects for study in the radio are different than those in gamma rays, indicating that dark matter searches in the radio can be complementary to searches in other energy bands. I also investigate the cosmic ray population in the merging cluster A2319, which hosts a previously detected radio halo. I present new observations which reveal a two-component radio halo: a 2 Mpc region that extends far past the observable X-ray emission, and an 800 kpc "core" that is bounded by the X-ray

cold front. I speculate on the origins of this structure, and show that a hadronic origin for this radio halo is disfavored. Finally, I discuss current ideas and future telescopes that will clarify and deepen our understanding of nonthermal emission in clusters.

Acknowledgments

First, I would like to thank my advisor, Tesla Jeltema, for helping me grow into a productive scientist. Tesla, working with you over the past five years has been such a pleasure. Thanks to Stefano Profumo for being an energetic and enthusiastic collaborator. Thanks to Larry Rudnick, for teaching me everything I know about radio astronomy and for being a patient and careful collaborator. A special thanks to Lisa Hunter at ISEE and the rest of the PDP community. My participation in the PDP has made me a more thoughtful and focused researcher, reminded me why I am doing what I am doing, and helped enormously with my confidence as a leader, educator, and scientist.

Finally, of course, thank you to Jacob. Thank you for listening to my daily research troubles and victories. Thank you for working through physics problems with me, for proofreading my proposals, and for helping me with my code. Thank you for entering graduate school a year earlier than me, so I could use you as a model for how to be a graduate student. And thank you for following me to my next academic adventure!

Reprinting of Published Material

The text of this dissertation includes reprints of previously published materials. Chapter 2 is adapted from the article "Gamma Rays from Star Formation in Clusters of Galaxies" from *The Astrophysical Journal*, volume 755, number 2, published in 2012. The full author list is: Emma Storm, Tesla E. Jeltema, and Stefano Profumo. Chapter 3 is adapted from the article "Constraints on Dark Matter Annihilation in Clusters of Galaxies from Diffuse Radio Emission" from *The Astrophysical Journal*, volume 768, number 2, published in 2013. The full

author list is: Emma Storm, Tesla E. Jeltema, Stefano Profumo, and Lawrence Rudnick. Chapter 4 is adapted the article "A Radio and X-ray Study of the Merging Cluster A2319" from the *Monthly Notices of the Royal Astronomical Society*, volume 448, issue 3, published in 2015. The full author list is: Emma Storm, Tesla E. Jeltema, and Lawrence Rudnick. Tesla Jeltema supervised the research that forms the basis for this material.

Chapter 1

Introduction

1.1 Components of a Galaxy Cluster

Galaxy clusters are the most massive, gravitationally-bound objects in the universe. Observations of galaxy clusters in different energy bands can probe different structural components. The hundreds to thousands of galaxies that make up a cluster can be seen from optical observations. X-ray observations reveal that these galaxies are embedded in a hot gas at ∼keV temperatures that makes up $\gtrsim 80\%$ of the baryonic matter in a given cluster (Cavaliere & Fusco-Femiano 1976; Sarazin 1986).

However, the velocities of cluster member galaxies indicate that they are subject to a more significant source of gravity than mass estimates of the ICM from X-ray observations would suggest. The bulk (80%) of the mass in a cluster, typically $10^{14} - 10^{15} M_{\odot}$, is dark matter. Observations of lensed background galaxies behind galaxy clusters can map the distribution of mass, and thus the dark matter distribution, in galaxy clusters (Clowe et al. 2006).

Radio observations of diffuse, ∼Mpc-sized synchrotron emission in some clusters indicate that clusters host cosmic-ray electrons and magnetic fields that permeate the the ICM (Feretti et al. 2012). However, the origins this nonthermal population of particles is unknown. Cosmic-ray electrons may be the products of cosmic-ray proton collisions with particles in the ICM, or they may have been

accelerated by turbulence driven by the formation of clusters (Brunetti & Jones 2014). Some fraction of cosmic rays could be the result of dark matter annihilation or decay (Colafrancesco et al. 2006).

Observations of nonthermal emission in the hard X-ray (> 10 keV) and gamma-ray (> 100 MeV) bands from clusters would help to distinguish between these different potential origins of cosmic rays. However, diffuse emission from clusters has not yet been detected in these high-energy bands (hard X-ray: e.g., Wik et al. 2012, 2014; gamma-ray: e.g., Huber et al. 2013; Ackermann et al. 2014). This dissertation is focused on understanding nonthermal phenomena in galaxy clusters.

1.2 The Intracluster Medium

The intracluster medium (ICM) is a low density ($\sim 10^{-3}$ cm^{-3}) plasma that is heated via shocks and turbulence from structure formation to temperatures in $1 - 15$ keV range. The dominant X-ray emission mechanism is via thermal bremsstrahlung radiation. X-ray observations of this radiation therefore trace the gas density (or, more precisely, the square of the gas density) (Sarazin 1986).

Relaxed, or non-merging, clusters are characterized by symmetric X-ray emission that is centrally peaked and falls off radially with the decreasing gas density. As the intracluster gas near the center of the cluster relaxes, it cools and condenses. This results in a sharp rise in the X-ray surface brightness and a drop in the X-ray temperature in the core of the cluster. Clusters with these observational features are typically called cool-core clusters (Molendi & Pizzolato 2001; Chen et al. 2007; Hudson et al. 2010).

Merging events can leave signatures on the gas distribution in a cluster. The merger history of a cluster can thus be reconstructed by examining its X-ray emission. Brightness discontinuities in the X-ray are clear signals of a disturbed ICM. Shock fronts from mergers are one such signal, and result in compressed intracluster gas that is relatively brighter in X-rays than its surroundings, with a larger temperature and higher pressure on the side of the higher gas density.

However, shock fronts are relatively difficult to detect in the X-ray, as they are often far from the cluster center where the gas density is low, and have only been observationally confirmed in a handful of clusters (Markevitch & Vikhlinin 2007).

Cold fronts are another type of X-ray brightness discontinuity found in clusters. A cold front exhibits a density discontinuity, but the temperature shift is opposite that in shocks: on the side of higher gas density, the temperature is *lower*. The pressure is roughly equal across the cold front. Unlike shocks, cold fronts are not sites of particle acceleration (Markevitch & Vikhlinin 2007). Cold fronts, which are often located $\lesssim$ 150 kpc from the cluster center, are found in a majority ($\sim 60\%$) of nearby, massive clusters (Ghizzardi et al. 2010).

Cold fronts are contact discontinuities that result from cold, dense cluster cores moving through hotter regions of the ICM. Cold fronts are found in both relaxed clusters and clusters undergoing major mergers (where "major merger" means the mass ratio between the merging subclsuters is near $1:1$). A cold front is thought be the result of a major merger that occurred off axis, or a more minor merger event (where the mass ratio is $3:1$ or larger). Such a merger event would disturb the gas in the central subcluster core, causing it to move or slosh around in its gravitational potential well, resulting in a cold front where the dense, cold core encounters hotter, more rarefied gas. A distinctive spiral pattern seen in the X-ray residuals after subtraction of a smooth component is a second indicator of core sloshing (Ascasibar & Markevitch 2006; Markevitch & Vikhlinin 2007).

There are several methods to quantify how disturbed a cluster is from its X-ray emission, which can be used to determine its merger history. One such method is the calculation of the concentration parameter, defined as the ratio of the peak X-ray surface brightness over the ambient brightness (Santos et al. 2008). The concentration parameter effectively differentiates between clusters with undisturbed cores and those with disturbed cores (from e.g., mergers). The centroid shift, which measures the displacement of a cluster's core from its equilibrium position, is another method to quantify cluster disturbance (O'Hara et al. 2006; Poole et al. 2006). These quantitative measurements are often used in conjunction with observations of shocks and cold fronts to understand a cluster's dynamical state (e.g.,

Rossetti et al. 2013).

1.3 Diffuse Radio Emission in Clusters

1.3.1 Morphologies of Diffuse Radio Emission

Radio observations of some galaxy clusters show evidence of diffuse synchrotron emission that is large-scale ($\sim$ 1 Mpc) and not associated with individual galaxies; rather, this emission tends to trace the ICM. There are several different morphologies of observed diffuse radio emission in galaxy clusters.

Giant radio halos fill the cluster volume, tend to trace the ICM of clusters, are unpolarized, and have steep spectra, with $\alpha > 1$, where the flux density $S_\nu \propto \nu^{-\alpha}$. Typical observations of radio halos occur at frequencies near 1 GHz, with flux densities in the few to hundreds of milli-Janskys range at this frequency (mJy; 1 Jy= 10^{-26} W m^{-2} Hz^{-1}). Radio halos tend to be centered near the X-ray peak, with emission distributed across areas $\sim$ 1 Mpc in diameter. Radio halos are typically found in merging clusters, while more relaxed clusters tend not to host radio halos (Buote 2001; Cassano et al. 2010, 2013). There are currently about 50 clusters with detected radio halos (Feretti et al. 2012). While this number might seem to suggest that halos are rare, they are in fact found in a substantial fraction of X-ray bright clusters; approximately 30% of clusters with X-ray luminosities $> 5 \times 10^{44}$ erg s^{-1} host radio halos (Cassano et al. 2011). As discussed in Section 1.3.2, the origins of radio halos are under debate.

Giant radio relics are found primarily near the periphery of clusters. Relics tend to be asymmetrical in shape and $\sim$ 1 Mpc in size along their longest dimensions. Relics are strongly polarized (tens of percent), which indicates some level of organization of the magnetic field in the emission region. Relics generally trace shock fronts from merger events at the edges of clusters, which suggests that the cosmic rays responsible for relic emission are likely accelerated across those shocks. There are approximately 50 known relics in about 40 clusters (Feretti et al. 2012).

Some relaxed, cool-core clusters display diffuse radio emission in the form of radio mini-halos. Mini-halos are limited to the cluster core and typically are tens to hundreds of kpc in diameter. In common with giant halos and relics, mini-halos tend to have steep spectra and low surface brightness. Mini-halos tend to be found in clusters with radio-bright active galactic nuclei (AGN) at their centers. However, the emission from mini-halos is fainter and larger than the radio emission from these central AGN, and appears to be associated with the ICM in the core, rather than the AGN itself. There are so far only about 20 observed mini-halos, because of their smaller size and potential for confusion with radio-bright central AGN (Giacintucci et al. 2014b).

1.3.2 Origins of Radio Halos

The varied morphologies of diffuse radio emission in clusters suggest different physical origins. The diffuse, volume-filling nature of radio halos make their origins particularly difficult to explain, as the cooling times of cosmic-ray electrons are much shorter than diffusion timescales in cluster environments. While the origins of radio halos are still under debate, two prevailing models for cosmic-ray acceleration have developed over the past two decades: the hadronic (or secondary) model, and the re acceleration (or primary) model (e.g., Brunetti & Jones 2014).

In the hadronic model, cosmic-ray protons were accelerated by shocks and turbulence driven by structure formation, or injected into the ICM by accelerators in cluster galaxies such as AGN, and are sufficiently long-lived to diffuse throughout the volume of the cluster (Volk et al. 1996; Berezinsky et al. 1997). These cosmic-ray protons can collide with thermal particles in the ICM. Among the collision products are cosmic-ray electrons, which then synchrotron radiate away their energy *in situ* in the presence of cluster-strength magnetic fields (Dennison 1980; Blasi & Colafrancesco 1999). The hadronic model naturally explains the diffuse nature of radio halos and the observed correlation between X-ray and radio emission in clusters, since both trace the gas density in this scenario. However, cosmic ray proton collisions also produce neutral pions that decay to gamma

rays, and clusters have not yet been detected in the gamma-ray band. Current upper limits on the gamma-ray emission from *Fermi*-LAT severely constrain the hadronic origin model for cosmic rays (Ackermann et al. 2014).

In the reacceleration model, a long-lived mildly relativistic population of seed electrons is reaccelerated to energies sufficient to produce observable synchrotron emission by merger-driven turbulence throughout the cluster (Brunetti et al. 2001, 2004; Brunetti & Lazarian 2011a; Petrosian 2001; Donnert et al. 2013). In this context, the predicted gamma-ray emission from Inverse Compton (IC) scattering is low compared to observed upper limits (e.g., Brunetti & Lazarian 2011a; Brunetti et al. 2012). However, the properties of turbulence in the ICM are poorly understood, which limits the predictive capabilities of this model.

1.3.3 The Radio Halo – Merger Connection

Radio halos and relics are typically found in merging clusters, characterized as such by the level of disturbance in the observed X-ray emission (Cassano et al. 2010). There is an observed correlation between the properties of radio halos and the X-ray properties of their host clusters. Specifically, the power of a radio halo is known to scale with the X-ray luminosity, temperature, and mass of a cluster (Giovannini et al. 1999; Liang et al. 2000; Cassano et al. 2006, 2013).

Deep radio observations of a complete sample of galaxy clusters have allowed for the discovery of a split in the distribution of clusters into those with and without radio halos (Venturi et al. 2007, 2008). Clusters with radio halos exhibit a trend of increasing radio power with increasing X-ray luminosity. This trend spans a decade in X-ray luminosity and two decades in radio power. However, there is also a population of clusters with X-ray luminosities in the same range that span an order of magnitude with no detected radio emission (Brunetti & Lazarian 2007; Cassano et al. 2013). With few exceptions, the clusters that host radio halos are known to be undergoing major mergers, and those clusters with no radio emission are more relaxed (Cassano et al. 2010; Feretti et al. 2012). This correlation between the existence of a radio halo and the dynamical state of a

cluster strongly implies that the the origins of radio halos and the cosmic rays responsible for them are driven by cluster mergers.

However, recent discoveries challenge our understanding of the radio-halo–merger connection. The cluster A2142, which was previously considered a cool-core cluster with radio emission at its center classified as a mini-halo, is now known to host a giant ~ 2 Mpc radio halo (Farnsworth et al. 2013; Rossetti et al. 2013). Another relaxed, cool core cluster, CL1821+643, was recently discovered to host a 1.1 Mpc radio halo (Bonafede et al. 2014). The merging cluster A2319 is now known to host a radio halo that extends far beyond its X-ray emission (Farnsworth et al. 2013), and has a unusual morphology near the center. These discoveries suggest that the connection between radio halos and cluster dynamics may be more complex than previously thought. I discuss my own work on the radio halo in A2319 and its relation to the dynamics of the cluster in Chapter 4.

1.3.4 Magnetic Fields in Clusters

The existence of diffuse synchrotron emission in clusters implies the existence of large-scale magnetic fields distributed throughout the ICM. A simple equipartition argument that sets the cosmic-ray energy density equal to the magnetic energy density yields volume-averaged field strengths of $\sim 0.1 - 1\mu$G (Govoni & Feretti 2004).

However, magnetic fields in clusters are difficult to measure. The best probe of magnetic fields in clusters is via Faraday rotation measures (RMs) of radio emission from galaxies in or behind a cluster. As linearly polarized light travels through a coherent magnetic field, the plane of polarization is rotated by an amount proportional to the strength of the magnetic field along the line-of-sight, the gas density, and the square of the wavelength of light. Synchrotron radiation is generically linearly polarized, so RMs for radio emission from galaxies traveling through a cluster magnetic field can be measured at different frequencies. These RMs can then be used to infer the magnetic field strength of the cluster.

Ideally, a set of background radio sources at multiple projected distances from

the cluster center would be used to measure RMs and then infer the magnetic field strength distribution. Background galaxies are preferable in theory to galaxies in a cluster because there exists the possibility that the RMs observed from cluster member galaxies are due to local effects near the galaxy, rather than the bulk magnetic field of the ICM. Using background galaxies for RMs would avoid this potential issue (Carilli & Taylor 2002).

In practice, few clusters have such a set of background radio galaxies, and even fewer have measured RMs (Kim et al. 1990; Clarke et al. 2001). Only a handful of clusters have RMs for galaxies at multiple projected distances, and these are often from galaxies inside the cluster (Clarke et al. 2001). Inferred magnetic field values are typically $1 - 10$ μG for merging clusters, and higher ($10 - 40$ μG) for relaxed clusters with cool cores (Carilli & Taylor 2002; Govoni & Feretti 2004).

The best studied cluster magnetic field is that of the Coma Cluster. From observations of multiple RMs of cluster member galaxies, the most likely distribution for the field strength of Coma is one that peaks at the center of the cluster at 4.7 μG and fall off as $n_{th}^{0.5}$, where n_{th} is the distribution of intracluster gas measured from the X-ray (Bonafede et al. 2010). This behavior is predicted by simulations of clusters that show the magnetic field strength is roughly symmetric around the cluster and traces the gas density along radial lines from the cluster center (Dolag et al. 2001). This magnetic field model is often applied to other clusters without well-studied RMs, or with an RM for only the central radio galaxy, from which the central magnetic field can be inferred (Vacca et al. 2012).

Lower limits on the magnetic field strength in clusters can be derived from the nondetection of nonthermal X-rays and gamma rays from clusters. The population of electrons responsible for diffuse radio emission should IC scatter background photons to hard X-ray ($\gtrsim 10$ keV) and gamma-ray energies. The relative strength of the IC scattering to synchrotron radiation can constrain the magnetic field. However, magnetic field estimates from upper limits on nonthermal X-ray emission are not particularly constraining; estimates for lower limits on the volume-averaged magnetic field are typically ~ 0.1 μG, far below equipartition estimates and inferred values from RMs (Wik et al. 2012).

Estimates of the magnetic field strength from the nondetection of gamma rays depend strongly on the choice of origin model for the cosmic rays. Assuming a hadronic origin model, magnetic field estimates need to be stronger than current inferred values from RMs to both match the observed level of synchrotron radiation and not exceed the gamma-ray upper limits (Jeltema & Profumo 2011; Brunetti et al. 2012). While this conclusion is useful in constraining the hadronic origin model for cosmic rays, it does not necessarily imply anything about magnetic field strengths in clusters.

1.4 Dark Matter in Clusters

1.4.1 Selected Evidence for Dark Matter

Preliminary evidence for the existence of dark matter came as early as 1933, through the work of Frits Zwicky on galaxy clusters. Zwicky studied the peculiar velocities of galaxies in the Coma cluster, and predicted the mass of the cluster using the virial theorem. He found the mass of the cluster must be substantially larger than the mass inferred from light emitted from the cluster in order for the galaxies to be moving as quickly as observed (Zwicky 1933). In 1970, Vera Rubin and Kent Ford provided the first robust evidence for the existence of dark matter. They found that galactic rotation curves were flat as a function of radial distance from the galactic center, indicating that there must be a substantial amount of mass located well beyond where the bulk of the visible matter is located (Rubin & Ford 1970).

Lensing analyses of galaxy clusters provide some of the strongest observational evidence for the existence of dark matter. A lensing analysis of the Bullet Cluster shows unambiguous evidence for non-baryonic dark matter (Clowe et al. 2006). The Bullet Cluster recently underwent a major merger in the plane of the sky. The X-ray emission traces the bulk of the visible matter in the ICM, while a lensing analysis can provide a mass distribution. In the case of the Bullet Cluster, the baryonic matter, traced by the X-ray emission, and the bulk of the mass, inferred

from lensing, are not located in the same place. This is exactly what is expected in a cluster merger, if dark matter only interacts via gravity, while the ionized ICM is subject to both gravitational and electromagnetic forces. Many such mass analyses of merging galaxy clusters have been performed since this work on the Bullet Cluster, and they generally agree with the Bullet analysis (Harvey et al. 2015).

1.4.2 Particle Dark Matter

There are several constraints from observations (or lack thereof) that any potential candidate for particle dark matter must satisfy. (1) Particle dark matter must be "cold" – that is, non-relativistic. If dark matter were "hot", then structure in the universe would form first on large scales (i.e., the scale of clusters or larger), with smaller structures like galaxies forming later. However, observations indicate that structure in the universe forms hierarchically from small to large, implying that dark matter must be "cold" to produce our universe. This requirement rules out Standard Model neutrinos as a possibility, as neutrinos are relativistic – that is, "hot". (2) Dark matter must also be uncharged, and interact at most very weakly with the electromagnetic sector, in order to explain observations such as the lensing analysis of the Bullet Cluster (and the lack of an observation of any concrete signature of dark matter so far). (3) Finally, a dark matter particle must also be stable on cosmological timescales; if unstable on timescales shorter than the Hubble time, the bulk of dark matter would have already decayed. These last two requirements rule out many Standard Model particles (e.g., protons, neutrons) as potential candidates.

While there are many candidates that satisfy these constraints, a particularly well-motivated possibility is the class of particles called Weakly Interacting Massive Particles, or WIMPS. These are neutral, stable particles that have masses in the GeV to TeV range. A feature of the particles in some WIMP models, such as supersymmetric extensions to the Standard Model (e.g., the neutralino) or Universal Extra Dimensions (e.g., the lightest Kaluza-Klein particle), is that their

interaction cross section is on a scale such that they will naturally produce the observed thermal relic abundance of dark matter (Jungman et al. 1996; Bertone et al. 2005; Hooper & Profumo 2007). These WIMP models are particularly attractive dark matter candidates partially for this reason.

1.4.3 Indirect Detection of Dark Matter

From an astrophysical standpoint, one of the most interesting characteristics of WIMP candidates like the neutralino is that they can continue to self-annihilate to Standard Model particles today. The products of these annihilations generically yield observable emission in a variety of astrophysical environments across the electromagnetic spectrum (e.g., Colafrancesco et al. 2006).

WIMPs can annihilate to quarks, which hadronize and result in the production of neutral pions, which then decay directly to gamma rays. Secondary gamma-ray production is also possible, as annihilation products can include electrons and positrons, which can then IC scatter background radiation, such as ambient starlight or the CMB, up to gamma-ray energies. A third method is the annihilation of dark matter particles directly to monochromatic gamma rays (e.g., final state radiation or internal bremmstrahlung); this would produce a line-like feature at the dark matter particle mass in the gamma-ray energy spectrum, and would be the "smoking-gun" signal of dark matter (e.g., Rudaz & Stecker 1991).

The observable emission from a dark matter annihilation depends on the total amount of dark matter, the dark matter particle mass and annihilation cross section, and the astrophysical emission mechanisms that convert annihilation products into photons. The flux from dark matter annihilation is usually expressed as follows:

$$\Phi = \frac{\langle \sigma v \rangle}{8\pi m_{\chi}^2} \Phi_{ann} \int_{\Delta\Omega} \mathrm{d}\Omega \int_{los} \mathrm{d}l \rho_{DM}^2(l) \tag{1.1}$$

where Φ is the total photon flux from a source, $\langle \sigma v \rangle$ is the velocity-averaged dark matter annihilation cross section, m_{χ}^2 is the dark matter particle mass, and Φ_{ann} is the photon flux per annihilation event that depends on the specifics of the astrophysical processes and environment of the source. The last piece of this

equation, collectively called the J factor, is a line-of-sight integral of the square of the dark matter density of the source(s) studied. Galaxy clusters are particularly good candidates for indirect searches for dark matter annihilation, as they are the most massive dark matter objects in the universe, and because they contain dark matter substructure down to at least the dwarf galaxy mass scale ($10^7\ M_\odot$), which can boost the J factor and thus the total annihilation signal relative to structures with smooth dark matter density profiles.

The majority of indirect detection studies focus on gamma-ray emission, or lack-thereof, as the observable product of WIMP annihilation. Studies on the gamma-ray emission from the Galactic center (e.g., Hooper & Linden 2011), diffuse Galactic emission (e.g., Ackermann et al. 2012a), and the isotropic background (Abdo et al. 2010a) have constrained various WIMP annihilation scenarios. Additional robust constraints have been derived from the nondetection of dwarf spheroidal galaxies (e.g., Geringer-Sameth & Koushiappas 2011; Ackermann et al. 2011, 2014) and galaxy clusters(e.g., Ackermann et al. 2010a; Huang et al. 2012; Arlen et al. 2012). Searches for gamma-ray lines have been performed primarily in the Galaxy (e.g., Weniger 2012; Bringmann et al. 2012; Ackermann et al. 2013), and also in dwarf spheroidal galaxies (Geringer-Sameth & Koushiappas 2012) and galaxy clusters (Hektor et al. 2013). While tentative detections of a dark matter signal have been claimed at times, most have not stood up against further scrutiny. The strongest constraints on dark matter annihilation with gamma-ray observations to date are from the nondetection of dwarf galaxies, where the upper limits on the annihilation cross sections are below the thermal relic limit for dark matter masses $\lesssim 100$ GeV annihilating to quarks and τ-leptons (Ackermann et al. 2015).

However, as noted earlier, WIMP dark matter annihilation can result in the production of electrons and positrons. In the presence of magnetic fields, electrons and positrons will lose energy via synchrotron radiation, which is potentially detectable with radio observations in environments where the magnetic field is on the μG scale, such as galaxies and galaxy clusters. A handful of studies have examined the potential for constraining dark matter annihilation with radio observations in

the Galactic center (Linden et al. 2011; Bringmann et al. 2014), the Large Magellanic Cloud (Siffert et al. 2011), dwarf spheroidal galaxies (Colafrancesco et al. 2007; Spekkens et al. 2013), and using the isotropic radio background (Hooper et al. 2012). I describe my own work on this subject, using galaxy clusters, in Chapter 3.

1.5 Nonthermal Processes in Cluster Galaxies

Galaxies in clusters also produce nonthermal emission in a variety of ways. AGN, which are often found in the central galaxies of relaxed clusters, are obvious examples of cosmic ray accelerators that produce a broad spectrum of nonthermal emission, from radio synchrotron emission up to emission in the gamma-ray band. However, this type of emission from an AGN is clearly associated with the galaxy itself, and not with the separate population of cosmic rays that are distributed throughout the ICM.

Star formation is also tied to the production of nonthermal particles in galaxies. Supernovae, the final stage in the lifecycles of massive stars, are efficient particle accelerators of nuclei, protons, and electrons. Cosmic-ray electrons can synchrotron radiate, observable in the radio band, and IC scatter starlight up to gamma-ray energies. Cosmic-ray protons and nuclei can collide with interstellar matter to produce neutral pions that decay to gamma rays (Völk 1989). Radio and gamma-ray luminosities are tightly correlated with the star-formation rate in star forming galaxies (Condon 1992; Yun et al. 2001; Ackermann et al. 2012b). In galaxy clusters, this correlation between star formation rate and gamma-ray luminosity can be used to set lower limits on the gamma-ray emission from clusters, by considering only the emission from star-forming galaxies. I discuss my work on this subject in Chapter 2.

1.6 Instruments

I use observations from telescopes in several energy bands to understand non-thermal emission from galaxy clusters. In this section, I describe briefly the instruments from which I use data in my dissertation.

1.6.1 *Fermi Gamma-ray Space Telescope*

The *Fermi Gamma-ray Space Telescope* is a gamma-ray observatory launched by NASA on June 11, 2008. *Fermi* hosts two instruments: the primary instrument, the Large Area Telescope (LAT), and the Gamma-ray Burst Monitor (GBM). *Fermi*-LAT is a widefield gamma-ray imaging telescope with an energy range of $\sim$ 20 Mev to $>$ 300 GeV. With a field of view of almost one fifth of the sky, *Fermi*-LAT surveys the entire sky approximately every three hours or two orbits. The point spread function of *Fermi*-LAT is strongly energy-dependent. The 68% (95%) containment angle of the PSF is approximately 4° (9°) at 100 MeV, and 0.15° (0.4°) at 10 GeV for normal-incidence photons. *Fermi*-LAT has not yet detected any gamma-ray emission from galaxy clusters (Ackermann et al. 2014). Gamma-ray emission from nearby galaxy clusters would likely be comparable to the size of the PSF to slightly extended.

Fermi-LAT is a pair-production telescope. When a gamma ray is incident on the LAT detector, it is converted to an electron-positron pair. The direction of incident gamma rays can be reconstructed from the tracks of the electron-positron pairs through the detector, while its energy can be calculated from the energy deposited in a calorimeter. The dominant background is cosmic rays, which produce tracks in the LAT detector and outnumber gamma ray events by many orders of magnitude. An anti-coincidence shield surrounding the telescope rejects the majority of cosmic-ray events, although further rejection is also performed on the ground after data acquisition. Data with several different levels of background rejection are available to users.

Data from the *Fermi*-LAT are publicly available for download almost immediately after acquisition. The main analysis package for *Fermi* is the Fermi Science

Tools, developed jointly by the LAT and GBM instrument teams and the Fermi Science Support Center [1].

1.6.2 *XMM-Newton*

The European Space Agency's (ESA) X-ray Multi-Mirror Mission (*XMM-Newton*) is an X-ray observatory that was launched into space on December 10, 1999. *XMM-Newton* has 3 telescopes: EPIC, an imaging camera; RGS, a spectrometer, and the OM, an optical/UV imager and spectrometer. The primary mode of *XMM-Newton* is pointed observations, although several surveys have been conducted over the lifetime of the instrument.

The EPIC instrument has 3 CCD cameras, 2 of which are identical except for their relative orientation (MOS-1 and MOS-2), and a third (PN). The MOS cameras have smaller pixels than the PN camera, while the PN has better timing resolution. The EPIC instrument operates in the X-ray band $0.15-12$ keV. There are three optical filters that can be set by the observer. The filter wheel limits the field of view to a circle with a diameter of ~ 30 arcmin, leaving the corners of the CCD arrays covered. The angular resolution of the MOS cameras is ~ 5 arcsec, and ~ 12 arcsec for PN. X-ray emission from the ICM of nearby galaxy clusters tend to fill the entire FOV of *XMM-Newton*.

There are several components of the EPIC background. One such background, called the Quiescent Particle Background (QPB), is mainly comprised of stray cosmic rays that interact with the detectors. The QPB is modeled using the unexposed corners of the CCD arrays that are covered by the filter wheel. There are also several known instrumental lines caused by fluorescent X-rays, and can be modeled or excised for spectral analyses. A third background is low-energy (or soft, < 100 keV) protons that travel down the telescope and deposit their energy onto the CCDs. These particles create a highly variable background, typically referred to as flares, that can be removed by examining the light curve of an observation. The primary external background for most observations is the cosmic

[1] fermi.gsfc.nasa.gov/ssc

X-ray background, dominated by diffuse X-ray emission from the galaxy and distant, unresolved X-ray point sources, although this can also serve as a science target.

The main analysis tool for *XMM-Newton* is the Scientific Analysis System (SAS)[2]. The Extended Source Analysis Software (ESAS) is a complementary package specifically designed for analysis of observations of extended sources, such as galaxy clusters (Snowden et al. 2008).

1.6.3 *Jansky Very Large Array*

The Karl G. Jansky Very Large Array (VLA) is an interferometric array of 27 radio telescopes located in New Mexico. The VLA provides continuous coverage of the frequency range $1 - 50$ GHz, which is divided into eight observing bands. Radio emission in galaxy clusters generally follows a power law, $S_\nu \propto \nu^{-\alpha}$. Most observations of galaxy clusters are therefore in the lower frequency bands, typically the L-band ($1 - 2$ GHz).

Interferometers essentially act as spatial filters of flux from the sky. Each telescope in the array records a voltage across its antenna that is proportional to the brightness from the sky at a particular frequency. The voltages from each pair of antennas are correlated – that is, multiplied and averaged together – to yield a measurement of the visibility, which is the basic data form of interferometers like the VLA. Figure 1.1 illustrates the components of a simple, two-antenna interferometer.

In Figure 1.1, two antennas are separated by a baseline b. An incident plane wave will arrive from the sky at antenna 1 with a delay relative to antenna 2 of $\tau_g = \vec{b} \cdot \hat{s}/c = bcos\theta/c$. The correlated visibility R_c (or V_c) for this antenna pair is then equal to the time-average of the product of each antenna's voltage: $R_c = (V^2/2)cos(\omega\tau_g)$, where ω is the frequency of the observation. This argument $\omega\tau_g$ is typically expressed in terms of multiples of the baseline in wavelength: $\omega\tau_g = 2\pi\vec{b} \cdot \hat{s}/\lambda = 2\pi ul$, where $u = b/\lambda$ and l is the component of the unit vector

[2] xmm.esac.esa.int/sas/

$\hat{s}$ in a particular direction, such that $ul = bcos\theta/\lambda$. For a two-dimensional array, the baseline vector b can be written in terms of its components as $\vec{b} = \lambda(u, v)$ and the directional unit vector $\hat{s}$ can be written as $\hat{s} = (l, m)$. For an extended source on the sky, such as a radio halo in a galaxy cluster, the two-dimensional visibility function is related to the intrinsic source brightness as follows:

$$V_\nu(u, v) = \int I_\nu(l, m)\exp(-i2\pi(ul + vm))\mathrm{d}u\mathrm{d}v \tag{1.2}$$

Therefore, the visibility function–that is, the data that the interferometer records, often referred to as *uv* data–is related to the sky brightness of an object via a Fourier transform.

The resolution limit of an interferometer is set by the longest baseline, or largest separation between a pair of antennas. This roughly sets the size of the point source response, or *synthesized beam*. The angular size of the synthesized beam is approximately equal to λ/b_{max}, where λ is the wavelength of the observation and b_{max} is the longest baseline.

The VLA has mobile telescopes that can be moved into four primary configurations (A,B,C,D). The A configuration is the most spread out; it has the longest baselines overall. The spacings on average decrease from the A configuration to the D configuration. The A configuration therefore has the highest overall resolution. In the L-band ($1-2$ GHz), the resolution in the A configuration is 1.3 arcsec, dropping to 46 arcsec for the D configuration.

The shortest baseline sets the largest angular size scale on the sky that can be observed. For the A configuration, in the L-band, the largest angular size is 36 arcsec. This increases to 970 arcsec for the D-configuration, which is the configuration with the shortest set of baselines.

The size of the *primary beam*, or roughly, the field of view, is set by the size of a telescope's dish, and depends on the frequency of the observation. The VLA telescopes have a diameter of 25 m, and the primary beam in radians can be determined by: $\theta_{PB} = \lambda/D$. For an observation in the L-band ($1 - 2$ GHz), the primary beam is about 45 arcmin.

Radio halos are typically $\sim$ 1 Mpc in physical size, which is roughly half a

degree in angular size for nearby clusters. For observations with interferometers, it is advantageous then for observations to take place in the configuration with the shortest baselines, and therefore the maximum angular observing scales; this is the D configuration for the VLA.

The primary analysis packages for calibrating, reducing and analyzing data from the VLA are CASA[3] and AIPS[4].

1.7 Outline

The nondetection of gamma-ray emission from clusters has strongly constrained nonthermal processes in the ICM. However, there must be some gamma-ray emission in clusters, from, at minimum, the galaxies themselves. In Chapter 2, I derive lower limits on the gamma-ray emission in galaxy clusters from cluster member galaxies. The rate of star formation in a galaxy can be determined from its infrared or radio luminosity. Using scaling relations to determine the gamma-ray luminosity from the star formation rate of cluster member galaxies, I place lower limits on the gamma-ray emission from star formation alone in a sample of nearby galaxy clusters. This lower bound on the gamma-ray emission in clusters from star formation is a previously-unrecognized gamma-ray background that will become more important as the upper limits on emission from the ICM improve over time.

Upper limits on the gamma-ray emission from clusters have also been used to constrain the annihilation of dark matter. However, the products of dark matter annihilation are expected to also include electrons and positrons, which produce synchrotron radiation in cluster environments. In Chapter 3, I use nondetections and weak detections of diffuse radio emission from galaxy clusters to constrain dark matter annihilation, and compare these constraints to those from gamma-ray nondetections.

While the nondetection of diffuse radio emission in clusters can be used to constrain dark matter, strong detections of radio halos in some clusters indicates that

[3] casa.nrao.edu
[4] aips.nrao.edu

clusters do host a nonthermal population of cosmic-ray electrons. Observations of a radio halo, especially in conjunction X-ray observations, can yield insight into this nonthermal cosmic-ray population, despite the lack of a secondary handle on this population via gamma-ray observations. In Chapter 4, I present results from radio and X-ray observations of the merging galaxy cluster A2319. I compare the unusual morphology of the radio halo in A2319 to its X-ray emission to explore how the dynamical state of this cluster affects the cosmic ray population responsible for this radio emission. Finally, I conclude with a summary and a discussion of current issues and future work.

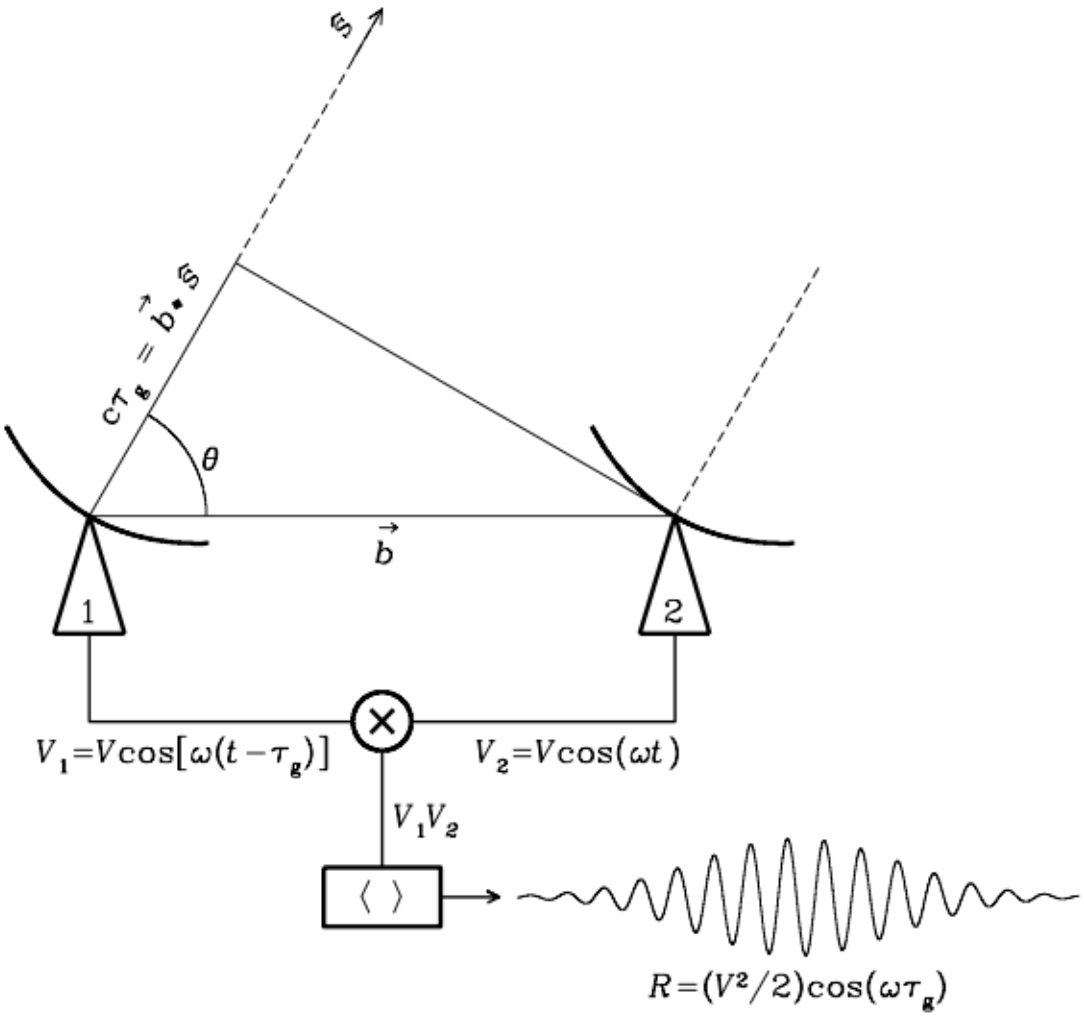

Figure 1.1: A two-dish interferometer. Copied from *Essential Radio Astronomy*, an online course available at: www.cv.nrao.edu/course/astr534/ERA.shtml.

Chapter 2

Gamma Rays from Star Formation in Clusters of Galaxies

Note: This chapter is adapted the following published work: Storm, E., Jeltema, T. E., and Profumo, S., "Gamma Rays from Star Formation in Clusters of Galaxies", 2012, ApJ, 755, 117.

2.1 Introduction

Galaxy clusters contain a dense population of galaxies surrounded by gas distributed throughout the intracluster medium (ICM). The complex environment of galaxy clusters is bound to host, at some luminosity level, processes that lead to the production of gamma rays. In particular, a significant fraction of the gamma-ray emission is thought to be associated with the ICM, and more specifically with cosmic ray populations accelerated by shocks and turbulence within the ICM, as well as, possibly, with dark matter annihilation and decay (first suggested in Totani 2004).

Cosmic rays in the ICM environment can produce gamma rays via multiple processes. Clusters have not, however, been detected yet as gamma-ray sources. The Large Area Telescope (LAT), the primary instrument aboard the *Fermi Gamma-ray Space Telescope*, has placed upper limits on the flux from the best candidate

clusters and used these upper limits to place constraints on the cosmic ray populations in clusters (Ackermann et al. 2010b). Atmospheric Cerenkov telescopes such as H.E.S.S. and MAGIC have also reported null results from observations of selected clusters of galaxies, such as Perseus (Aleksić et al. 2012), Coma (Aharonian et al. 2009a), and A0085 and A0496 (Aharonian et al. 2009b).

In addition to the gamma rays produced by the ICM, the cluster member-galaxies themselves are at some level a source of gamma rays. Ordinary galaxies such as our own Milky Way, its satellite galaxies the Large Magellanic Cloud (LMC) and Small Magellanic Cloud (SMC), and the nearby Andromeda Galaxy (M31) have all been detected in gamma rays (MW: Abdo et al. 2009, LMC: Abdo et al. 2010e, SMC: Abdo et al. 2010c, M31: Abdo et al. 2010d). In addition, the recent detection by the *Fermi*-LAT of four star-forming galaxies, M82, NGC 253 (Abdo et al. 2010b) and NGC 1068 and NGC 4945 (Lenain et al. 2010), allowed for the determination of a quantitative functional relationship between the star formation rate and the gamma-ray luminosity (Ackermann et al. 2012b). While gamma-ray emission has not yet been detected from galaxy clusters, some minimum gamma-ray emission resulting from star formation activity in cluster members must exist. Lower limits on the gamma-ray flux from clusters of galaxies can therefore be determined by considering only the emission from cluster members with ongoing star formation, and can also provide insight into the star-forming population of galaxies within clusters, as compared to the field. This is the scope of the present study. The relations derived in Ackermann et al. (2012b) are used to predict lower limits on the gamma-ray luminosity coming from star formation within cluster members alone, provided total IR and/or radio luminosity measurements for a sample of clusters. We then compare these estimates to the *Fermi* upper limits on the gamma-ray luminosity from the same clusters (Ackermann et al. 2010b), and assess the potential of the *Fermi*-LAT over its lifetime as well as of the future Cerenkov Telescope Array (CTA) for detection of gamma-rays from star-forming galaxies in clusters.

In the following section, we review the sources of multiwavelength emission resulting from star formation in galaxies and clusters. In Section 2.3, we describe

our cluster sample selection and the available IR and radio data. In Section 2.4 we describe our results and present lower limits on the gamma-ray emission from a selection of clusters. We use the lower limits to explore the possibility of detection by various gamma-ray telescopes in Section 2.5, and conclude in Section 2.6.

2.2 Emission from Star Formation

The bulk of the bolometric luminosity of young stars is emitted in the ultraviolet (UV), which is then efficiently reprocessed into infrared (IR) light by dust in the interstellar medium (ISM) within galaxies such that their spectral energy distributions are peaked in the IR (Sanders & Mirabel 1996). The total IR luminosity ($8 - 1000\mu$m) thus traces closely the rate of star formation in a galaxy and is an extinction-free way to measure the star formation rate (SFR) since the ISM is optically thin to IR (Kennicutt 1998). However, the total IR luminosity is not directly measured; rather, single-band measurements (24 μm and 60 μm are commonly employed wavelengths) are converted to total luminosities either integrating over template SEDs (e.g., Dale & Helou 2002) or using relations derived from modeling the dust emission in the ISM (e.g., Sanders & Mirabel 1996). Both techniques are common in the literature and a determination of the total IR luminosity thus depends somewhat on the particular templates or relations used for conversion. Discrepancies between methods developed specifically by Dale & Helou (2002) and Sanders & Mirabel (1996) vary from $\sim 4\%$ for starburst galaxies, which have high SFRs and generally are very IR-bright ($L_{8-1000\mu\mathrm{m}} > 10^{11} L_{\odot}$), to $\sim$ 25% for low-luminosity galaxies, with Sanders & Mirabel (1996) method predicting smaller values for $L_{8-1000\mu\mathrm{m}}$ than those predicted by Dale & Helou (2002).

Massive stars typically end their life-cycles as supernovae, whose remnants (SNRs) are likely accelerators of cosmic ray protons and electrons (e.g., Völk 1989 and references therein). The cosmic-ray electrons interact with magnetic fields within a galaxy and quickly lose their energy through synchrotron radiation in the radio continuum. Measured at 1.4 GHz, the radio luminosity is tightly

correlated with total IR luminosity in star-forming galaxies over several orders of magnitude and is therefore also used as an indicator for SFR (Condon 1992; Yun et al. 2001). This correlation can be explained by a simple model that treats galaxies as "calorimeters" of both UV photons and cosmic-ray electrons (Völk 1989). Cosmic-ray electrons lose most of their energy through synchrotron radiation and UV photons lose most of their energy through absorption and re-emission by dust in the ISM. In this model, if the ratio of synchrotron emission versus total energy losses in the cosmic-ray electron population is large, then the radio luminosity becomes a proxy for SFR. In addition, if UV photons emitted by stars are effectively reprocessed into the IR, then IR luminosity would also trace with SFR. The $L_{1.4\mathrm{GHz}}$–$L_{8-1000\mu\mathrm{m}}$ ratio, which should be constant if both are due mainly to star formation, can be thus be used as an independent indicator of the SFR in galaxies. Active galactic nuclei (AGN), which can have large luminosities in both IR and radio due to processes other than just star formation, and which presumably also contribute to the gamma-ray emission in some clusters, deviate from this IR-radio correlation (Yun et al. 2001). We discuss this caveat in detail for the cluster sample under consideration here.

Gamma rays are expected to scale with SFR in normal, star-forming galaxies, and are thought to arise mostly from cosmic-ray nucleon collisions with the ISM and subsequent decay into charged and neutral pions, which then decay to leptons and gamma rays, respectively. At energy thresholds higher than those required for pion decay the gamma-ray spectrum is the same shape as the underlying cosmic-ray nuclei population, which is controlled by the number of SNRs. Therefore the amplitude of the gamma-ray spectrum can be used as a proxy for SFR. This is supported by observations of the LMC in gamma rays, which has been spatially resolved by *Fermi*-LAT. The LMC's star forming region 30 Doradus is associated with strong diffuse gamma-ray emission, which implies the cosmic-ray proton intensity is also strongest in that region (Abdo et al. 2010e). The secondary cosmic-ray electron population, resulting from charged pion decay, also contributes to the gamma-ray spectrum primarily by inverse-Compton up-scattering of starlight (Ackermann et al. 2012b).

Early in the mission, in all-sky survey mode, *Fermi*-LAT detected two starburst galaxies, M82 and NGC 253 (Abdo et al. 2010b). Those starbursts were also detected in the very-high-energy regime by ground-based gamma-ray telescopes (M82 by VERITAS; Acciari et al. 2009 and NGC 253 by H.E.S.S.; Acero et al. 2009). As first reported in Lenain et al. (2010) and later in Ackermann et al. (2012b), *Fermi*-LAT detected two additional starbursts, NGC 1068 and NGC 4945, which host AGN. Ackermann et al. (2012b) examined a sample of 69 galaxies, mostly consisting of starbursts for which *Fermi*-LAT has upper limits, 9 of which are associated with AGN. The sample includes the four starbursts detected by *Fermi*-LAT and several detected local group galaxies which are not starbursts: the SMC and LMC, the Milky Way, M31, and M33. Ackermann et al. (2012b) found that gamma-ray luminosity scales with total IR and radio luminosities and hence with SFR across several orders of magnitude in luminosity and SFR. The relationships found between SFR and gamma-ray luminosity are power law in nature and differ slightly depending on whether AGN are included in the sample, but the dispersion in the relationships dominate over the differences in the fits.

Star formation in cluster galaxies occurs at slower rates compared to that in field galaxies (see e.g., Reddy & Yun 2004, and references therein). However, the processes that suppress star formation in clusters are not well-understood. Chung et al. (2011) used infrared data from *WISE (Wide-field Infrared Survey Explorer)* to estimate SFRs for a sample of local clusters with known masses and found no correlation between cluster mass and SFR. This implies that clusters processes that scale with mass perhaps only weakly affect star formation, if at all. Ram pressure in particular scales up with cluster mass and is thought to influence star formation. Ram pressure strips gas from a galaxy as it moves through the ICM, removing the raw material needed for star formation. Rates of star formation in cluster galaxies get smaller as the radial distance from the cluster center decreases (Chung et al. 2011 and references therein) which supports the theory that ram pressure stripping strongly influences star formation. In addition, ram pressure is shown to decrease star formation in clusters in simulations (Book & Benson 2010) and in observations of the Virgo cluster (Vollmer et al. 2008). However,

this conflicts with the lack of evidence for a correlation between mass and star formation in local clusters, described by Chung et al. (2011) and others (e.g., Goto 2005). Galaxy-galaxy mergers and interactions also tend to trigger bursts of star formation in clusters, but are most common in poor clusters and groups, (e.g., Martig & Bournaud 2008), while the best clusters for detection in gamma rays tend to be rich and massive. Still many cluster galaxies do show evidence of ongoing star formation, and the density of galaxies within clusters mean that the summed contribution to the gamma-ray emission may be significant.

Cool-core clusters display elevated SFRs in their central galaxies, as compared to non-cool-core clusters (McDonald et al. 2011). These clusters have high density, low temperature cores which suggest that cool gas is steadily flowing into the center (for a review, see Fabian 1994). Therefore the elevated SFR may be due to this mass deposition onto the central galaxy, which would enhance star formation by supplying the brightest cluster galaxy (BCG) with a steady stream of raw material. Egami et al. (2006), however, found only a weakly suggestive relationship between mass deposition rate and SFR in a sample of X-ray selected clusters. In addition to several clusters of galaxies, in this work we also consider the possible gamma-ray emission from star formation in 3 BCGs located in cool-core clusters.

2.3 Methods

We estimate here the gamma-ray luminosity associated with star formation in cluster galaxies from the total infrared luminosity ($8 - 1000$ μm) and from the 1.4 GHz radio continuum luminosity using the relationships in Ackermann et al. (2012b). We restrict our analysis to emission from individual galaxies where there is active star formation, since star formation in clusters only occurs within galaxies. We performed a literature search for IR and radio data for cluster galaxies starting with the list of clusters in Ackermann et al. (2010b), which places upper limits on the gamma-ray flux for the best candidate clusters based on nondetection by *Fermi*-LAT. The clusters in Ackermann et al. (2010b) were selected from the HIFLUGCS catalog of brightest X-ray clusters (Reiprich &

Bohringer 2002). The clusters with the highest mass-to-distance-squared ratios were selected for analysis. Additionally, several clusters with nonthermal radio emission were included in the list of Ackermann et al. (2010b). We performed a literature search for radio and IR data on all of the clusters in that list, excluding several that were close to the galactic plane or that had high redshifts (with the exception of the Bullet Cluster). We excluded AGN from our calculated luminosities, since AGN can be bright in IR and radio but the emission is not due to active star formation. The results of the literature search are presented in Table 1 and the corresponding estimated gamma-ray luminosities are summarized in Table 2; the upper limits provided by Ackermann et al. (2010b) are also included in Table 2. In looking for IR and radio data, we preferentially searched first for total IR ($8 - 1000$ μm) and 1.4 GHz luminosity functions (LFs) of clusters with Schechter fits. We found fitted total IR LFs for two clusters, Coma (Bai et al. 2006) and the Bullet Cluster (Chung et al. 2010). While we found a radio LF for Coma (Miller et al. 2009) and several far-IR ($100 - 500$ μm) LFs for Virgo (Davies et al. 2010), they were presented as raw data and were not fit with Schechter functions, and we were therefore unable to use these LFs.

We expanded the search to include lists of luminosities of individual cluster members. Reddy & Yun (2004) presented $L_{1.4\mathrm{GHz}}$ and $L_{60\mu\mathrm{m}}$ for members in 7 clusters. Rieke et al. (2009) found a tight correlation between $L_{60\mu\mathrm{m}}$ and $L_{8-1000\mu\mathrm{m}}$ and derived a relationship for converting one to the other; we used this relation to convert the 60 μm data in Reddy & Yun (2004) to total IR. We converted each radio and IR galaxy luminosity to gamma-ray using the relationships in Ackermann et al. (2012b) that exclude AGN, then summed up the gamma-ray luminosities of individual galaxies to obtain a total cluster gamma-ray luminosity. We excluded galaxies classified as Seyferts or LINERs, which are typically AGN, from our calculations. Any galaxies not identified as Seyferts or LINERs that had one anomalously large luminosity (radio or IR) as compared to the other were checked in the literature, and those identified as hosting an AGN were also excluded. In Reddy & Yun (2004), only cluster members detected in both radio and IR were included, so total cluster luminosities using that data are most likely

underestimates in both IR and radio. In the cases for which we had luminosity functions, we first integrated the LF, then converted this total cluster luminosity to gamma-ray. Since the relationship between IR and gamma-ray luminosity is slightly steeper than linear, this procedure results in an overestimate of the true total gamma-ray luminosity by $\sim 20\%$. This, however, is smaller than the intrinsic dispersion in the relationship reported in Ackermann et al. (2012b), which we take as the uncertainty in our estimates of gamma-ray luminosities.

Uncertainties in galaxy IR and radio luminosities were not reported in the papers we found. We therefore report the uncertainties in the estimated gamma-ray luminosities as the dispersion in the power-law relationships derived in Ackermann et al. (2012b). For $L_{0.1-100\mathrm{GeV}}$ estimated from $L_{8-1000\mu\mathrm{m}}$, the uncertainty is 0.25 dex (excluding AGN). For $L_{0.1-100\mathrm{GeV}}$ estimated from $L_{1.4\mathrm{GHz}}$, the uncertainty is 0.19 dex (excluding AGN). While Ackermann et al. (2012b) provides uncertainties in the fit parameters, the scatter in the $L_{0.1-100\mathrm{GeV}}$-$L_{8-1000\mu\mathrm{m}}$ and $L_{0.1-100\mathrm{GeV}}$-$L_{1.4\mathrm{GHz}}$ relationships dominate over the fit parameter uncertainties.

In cool core clusters, there is evidence for active star formation in the central cluster galaxies (McDonald et al. 2011). We found radio fluxes for the brightest cluster galaxy that are not associated with AGN in 3 cool core clusters, Ophiuchus, A2029, and A2142, and included them in our sample. While Ophiuchus is close to the galactic plane, we include it as a representative cool-core cluster. The gamma-ray luminosities estimated from these clusters are most likely severe underestimates, but it is interesting to note that for cool core clusters the BCG alone can have a significant predicted gamma-ray emission due to increased star formation.

We note that there is observed large-scale ($\sim$ 1 Mpc) diffuse radio emission from the ICM of some galaxy clusters, which indicates the existence of cosmic rays that may also be responsible for as-yet-undetected gamma-ray emission. (Ferrari et al. 2008). These ICM cosmic rays are accelerated primarily by shocks and turbulence in the ICM, as opposed to SNRs in cluster galaxies, and are not related to star formation in galaxies. Observations of clusters in the IR are always associated with individual galaxies (see e.g., Coppin et al. 2011). We thus choose

to consider only the radio and IR emission from galaxies themselves in order to place conservative lower limits on the gamma-ray emission from clusters from star formation in cluster galaxies alone.

2.4 Results

We present our results in Table 1 and 2 and in the associated Figures 1 and 2. Table 1 shows the IR and radio luminosities for the clusters under consideration, while Table 2 presents our calculation for the gamma-ray luminosity lower limits, and compares the latter with the upper limits from Ackermann et al. (2010b). Finally, Figures 1 and 2 show the calculated gamma-ray luminosities as a function of the IR and radio luminosities, respectively.

For several clusters the lower limits on gamma-ray luminosity predicted from star formation are within an order of magnitude or so of the upper limits derived in Ackermann et al. (2010b). The lower limit luminosity of the BCG (IC 1101) in the cool-core cluster A2029 in particular is quite close to the upper limit. The core of A2029 shows extended radio emission which suggests it hosts an AGN (Taylor et al. 1994). A2029 has also been observed in X-rays, but it is unclear whether the X-ray emission is due to an AGN since the emission is not point-source-like and does not fit a power-law spectrum, as is typical for X-ray AGNs (Clarke et al. 2004). Additionally, the star formation rate calculated nominally from the presented radio luminosity in McDonald et al. (2011) using the relationship in Kennicutt (1998) yields an SFR that is higher than that of any local starburst galaxy; therefore is it most probable that only a fraction of the radio luminosity is due to star formation. However, the large ratio of far UV to Hα emission suggests that the BCG of A2029 is an older starburst galaxy with ongoing star formation activity (McDonald et al. 2011), so it is included in our sample.

The Bullet Cluster may not be detectable by *Fermi*-LAT due to its distance ($z \simeq 0.3$). It is, however, an interesting cluster, with a total IR LF available in the literature and a high IR luminosity, and was therefore included in our sample. If a cluster similar in mass and activity to the Bullet existed nearby it would

likely be observed in gamma rays. The Bullet Cluster's predicted emission from star formation is much lower than the upper limit on its gamma-ray luminosity given its distance, but this lower limit on the Bullet's gamma-ray luminosity is comparable to the detection threshold for a closer cluster with similar mass such as Coma (although the IR LF is a different shape than that of Coma (Chung et al. 2010)).

We present two total IR luminosities for the Coma cluster, one calculated from the total IR luminosity function (Bai et al. 2006) and the other from a sum of individual member luminosities (Reddy & Yun 2004). The galaxy sample used to calculate the LF in Bai et al. (2006) does include 3 AGN, but their contribution to the total luminosity is negligible. We therefore used the relation in Ackermann et al. (2012b) that excludes AGN, as for all other clusters. As expected, the gamma-ray luminosity as calculated from the IR LF is larger than the gamma-ray luminosity calculated from summing individual galaxy luminosities.

2.5 Discussion

2.5.1 Detections with *Fermi*-LAT

Given the lower limits presented in the previous section, we examine here which clusters, if any, may be detectable by *Fermi*-LAT over the course of the instrument's lifetime. *Fermi*-LAT is an all-sky survey telescope, covering the full sky every 2 orbits, or 3 hours. It was launched in June 2008 and is currently funded through at least 2016; it is expected to be operational for a total of 10 years. Its sensitivity gets better over time, and if we assume a 10-year flux sensitivity of $\sim 3 \times 10^{-9}$ cm^{-2} s^{-1} for detecting a point source with photon index $\alpha_\gamma = 2.2$ at the 5σ level, which is the best fit value for star-forming galaxies from Ackermann et al. (2012b), then several clusters have lower limit fluxes that are above or within a factor of 2-3 of this sensitivity limit, including A2029, Virgo, Coma, A1367, and Hydra, with the flux of A2029 strictly over the 3×10^{-9} cm^{-2} s^{-1} limit. The photon index $\alpha_\gamma = 2.2$ is chosen as it is the value used in Ackermann et al.

(2012b) to predict upper limits on gamma-ray luminosities from non-detected starburst galaxies. However, Virgo is a large, extended object, and it hosts a bright AGN, M87, which may make it difficult to detect emission in excess of this gamma-ray point source. Recently, Han et al. (2012a) claimed a detection of diffuse gamma-ray emission from the central 3° region of the Virgo Cluster due to dark matter annihilation; however further analysis is needed to confirm or deny this claim.[1]. Additionally, the BCG in A2029 may also host an AGN, which would also make detection of gamma-ray emission from the cluster as a whole potentially difficult. Coma specifically is a good candidate for detection. Recent radio observations of Coma show diffuse radio emission in the form of a halo and a relic (Brown & Rudnick 2011), indicating the existence of non-thermal processes throughout the cluster, which imply the existence of gamma rays, and as shown here star formation in the galaxies within Coma can also give significant gamma-ray emission.

2.5.2 Prospects for Detection with Ground-based Gamma-ray Telescopes

Galaxy clusters have not yet been detected by ground based gamma-ray telescopes, such as H.E.S.S., MAGIC or VERITAS. Recent studies of the Perseus cluster by MAGIC did not yield a detection apart from the central AGN, NGC 1275 and a radio galaxy, IC 310 (Aleksić et al. 2012). However, the gamma-ray spectrum of NGC 1275 as measured by MAGIC drops off above 630 GeV, which means that Perseus is a good potential candidate for detection in this energy range. The lower limit gamma-ray flux of Perseus above a TeV, about 1×10^{-19} cm^{-2} s^{-1}, is approximately six orders of magnitude smaller than the upper limits reported in Aleksić et al. (2012) and well below the sensitivity limits of current atmospheric Cerenkov telescopes. The gamma-ray emission associated with star formation in

[1]Since the publication of our paper, there has been more work on the claimed gamma-ray excess in Virgo. Upon further analysis, several groups, including the authors of the original paper, found no evidence for excess emission from Virgo or any other cluster (Macías-Ramírez et al. 2012; Han et al. 2012b).

Perseus is therefore unlikely to be detected by ground-based instruments.

We also investigated whether the next-generation ground-based telescopes, such as the CTA, would be able to produce a detection of galaxy clusters. As described in Actis et al. (2011), the effective area of CTA is typically the limiting factor for a given observing time, usually about 25-50 hours. If we assume a constant power law spectrum for the gamma-ray emission from star-forming galaxies in clusters with a photon index $\alpha_\gamma = 2.2$, we can estimate the lower limits on the flux from the clusters in our sample from 100 GeV to 10 TeV, which is the primary target energy range for CTA. The cluster with the largest flux in this range is A2029 with 2.6×10^{-15} cm^{-2} s^{-1}; Virgo and then Coma have the next highest fluxes at 6.7×10^{-16} cm^{-2} s^{-1} and 1.5×10^{-16} cm^{-2} s^{-1}, respectively. A1367 and Hydra also have predicted fluxes that are a factor of ~ 2 lower than Coma's. Using the flux of Virgo, the required effective area of CTA for 50-hour observation would be about 8 km^2; CTA will ideally cover at tens of km^2, at least. These estimates assume no spectral breaks at higher energies; as described in Ackermann et al. (2012b), starburst galaxies appear to have a spectrum described by a single power law, but the spectra of local galaxies such as the Milky Way are better described with an exponential cutoff or broken power law. We therefore take these very high energy fluxes to be optimistic predictions. We conclude that the performance of CTA may allow for the detection of gamma rays from star formation in galaxy clusters for potentially several clusters.

2.6 Conclusions

In this chapter, we calculated lower limits on the gamma-ray emission from galaxy clusters considering only cluster member galaxies with active star formation using observed IR and radio luminosities for selected, nearby massive clusters. Employing the relationships derived in Ackermann et al. (2012b) for *Fermi*-LAT detected galaxies, we converted IR and radio cluster luminosities into gamma-ray luminosities. Several clusters have lower limits on their gamma-ray emission that are within about an order of magnitude of the upper limits based on the

Fermi-LAT non-detections from Ackermann et al. (2010b), implying that star formation could contribute at the level of $\sim 10\%$ to cluster gamma-ray emission. Thus, nonthermal emission in the form of gamma rays from star formation is an important background to the gamma-ray emission from the ICM. As upper limits on the gamma-ray emission from clusters improve over time, this background from star formation will become increasingly relevant. Looking towards the future, CTA may be able to detect this gamma-ray emission from star formation for anticipated instrumental performance and design.

Table 2.1: IR and Radio Luminosities

Name	$\log(L_{8-1000\mu m})$ ($L_\odot$)	Ref.	$\log(L_{1.4\mathrm{GHz}})$ (W Hz^{-1})	Ref.	D_L (Mpc)
Coma (LF)[a]	11.75	2	...	...	100
Coma	11.32	1	23.16	1	100
AWM7	10.80	1	22.28	1	69.2
Perseus	10.53	1	22.05	1	72.3
Hydra	11.10	1	22.68	1	57.1
A1367	11.48	1	23.25	1	96.6
Virgo	10.86	1	22.42	1	19.4
Bullet	12.63	3	...	...	1479
Ophiuchus[b]	...	...	22.68	4	118
A2029[b]	...	...	24.86	4	339
A2142[b,c]	...	...	22.68	4	401

Notes. D_L is luminosity distance, retrieved from the NASA/IPAC Extragalactic Database (NED). The NED is operated by the Jet Propulsion Laboratory, California Institute of Technology, under contract with the National Aeronautics and Space Administration.

([a]) LF is luminosity function. See the text for details.

([b]) The data for these clusters is for BCGs only, not the full clusters.

([c]) The radio luminosity for the BCG of A2142 is an upper limit.

References. (1) Reddy & Yun (2004); (2) Bai et al. (2006); (3) Chung et al. (2010); (4) McDonald et al. (2011).

Table 2.2: Upper and Lower Limits on Gamma-ray Luminosities

Cluster Name	$\log(L_{0.1-100\mathrm{GeV}})$ (from $L_{8-1000\mu\mathrm{m}}$) ($\pm$0.25 dex) Lower Limit	$\log(L_{0.1-100\mathrm{GeV}})$ (from $L_{1.4\mathrm{GHz}}$) ($\pm$0.19 dex) Lower Limit	$\log(L_{0.1-100\mathrm{GeV}})$ Upper Limit
Coma (LF)[a]	41.07	...	42.55
Coma	40.50	41.07	42.55
AWM7	40.01	40.17	42.15
Perseus	39.73	39.93	43.55
Hydra	40.28	40.55	41.74
A1367	40.70	41.19	42.07
Virgo	40.04	40.29	41.61
Bullet	42.06	...	44.66
Ophiuchus[b]	...	40.66	43.45
A2029[b]	...	43.06	43.46
A2142[b]	...	40.66	43.54

Notes. Luminosities are reported in erg s^{-1}. The uncertainties in the lower limit luminosities are from Ackermann et al. (2012b) and are a measure of the dispersion in the relationships used to calculate $L_{0.1-100\mathrm{GeV}}$. Upper limits on gamma-ray luminosity (Column 4) assume a power-law spectrum with $\alpha_\gamma = 2$ in converting from the $0.2 - 100$ GeV energy band, as in Ackermann et al. 2010b, to $0.1 - 100$ GeV for direct comparision with lower limits estimated from IR and radio luminosities.

([a]) LF is luminosity function. See the text for details.

([b]) The data for these clusters is for BCGs only, not the full clusters.

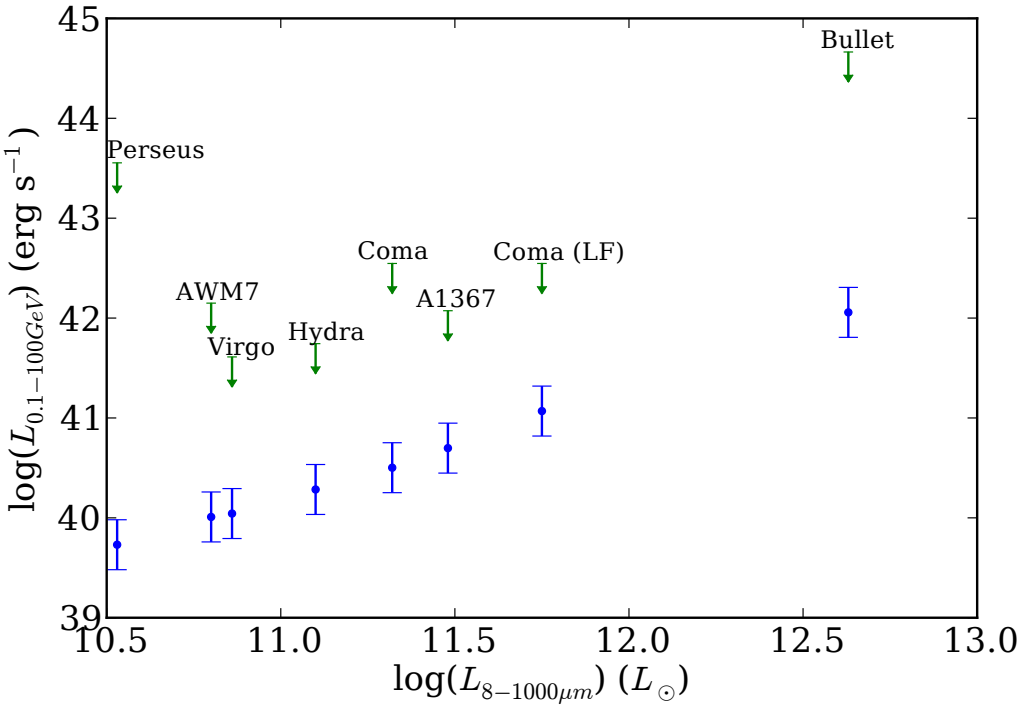

Figure 2.1: Gamma-ray luminosity versus total infrared luminosity. Blue points correspond to lower limits on gamma-ray luminosity from star formation, calculated using relations in Ackermann et al. (2012b). The uncertainties are reported in Ackermann et al. (2012b) and are a measure of the dispersion in the $L_{0.1-100\mathrm{GeV}}$–$L_{8-1000\mu\mathrm{m}}$ relationship. Green arrows correspond to upper limits from Ackermann et al. (2010b).

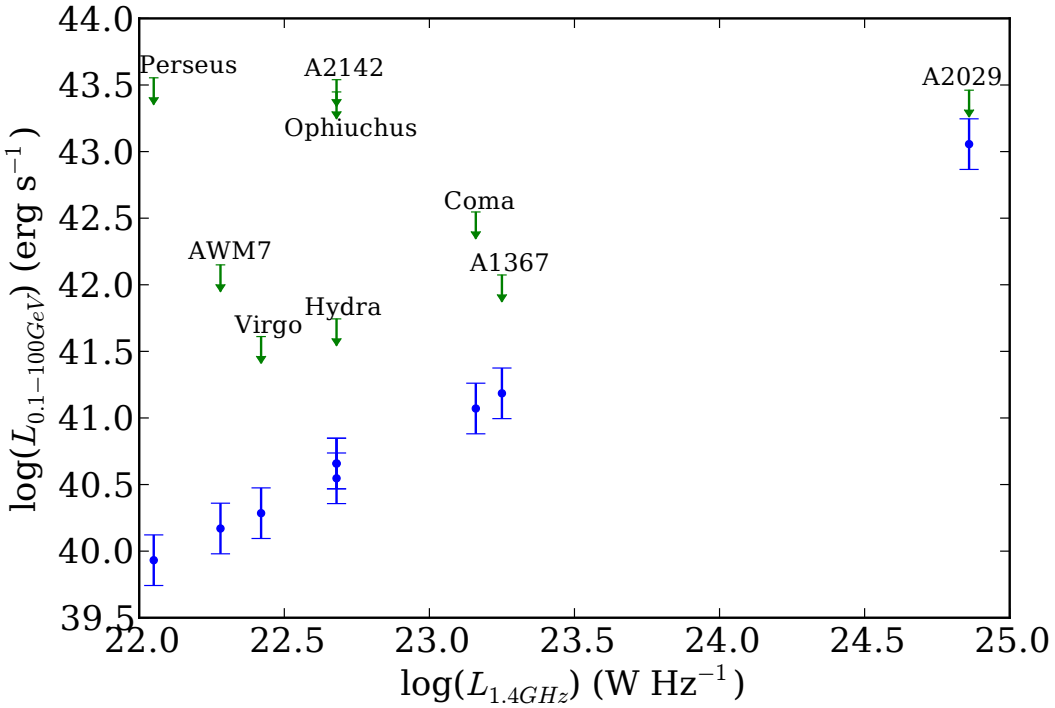

Figure 2.2: Gamma-ray luminosity versus radio luminosity. Blue points correspond to lower limits on gamma-ray luminosity from star formation, calculated using relations in Ackermann et al. (2012b). The uncertainties are reported in Ackermann et al. (2012b) and are a measure of the dispersion in the $L_{0.1-100\mathrm{GeV}}$–$L_{1.4\mathrm{GHz}}$ relationship. Green arrows correspond to upper limits from Ackermann et al. (2010b).

Chapter 3

Constraints on Dark Matter Annihilation in Clusters of Galaxies from Diffuse Radio Emission

Note: This chapter is adapted from the following published work: Storm, E., Jeltema, T. E., Profumo, S., and Rudnick, L., "Constraints on Dark Matter Annihilation in Clusters of Galaxies from Diffuse Radio Emission", 2013, ApJ, 768, 106.

3.1 Introduction

Galaxy clusters are 80% dark matter by mass, making them good candidates for astrophysical searches for a signature from particle dark matter. Among the best motivated particle candidates for dark matter are weakly interacting massive particles, or WIMPS, which can self-annihilate to Standard Model particles. The products of WIMP annihilations generically yield a broad spectrum of electromagnetic emission in cluster environments that is potentially observable across a wide range of frequencies, from radio to gamma rays (Colafrancesco et al. 2006).

Galaxy clusters have not yet been detected in gamma rays (see recently, e.g., Macías-Ramírez et al. 2012; Han et al. 2012b). Upper limits on the gamma ray

emission have been used to place constraints on the dark matter annihilation cross section. Previous studies that placed constraints on dark matter annihilation or decay in clusters have focused on searching for gamma-ray emission using the Large Area Telescope (LAT) onboard the *Fermi Gamma Ray Space Telescope* at the GeV scale (Ackermann et al. 2010a; Dugger et al. 2010; Ando & Nagai 2012; Huang et al. 2012; Nezri et al. 2012; Han et al. 2012b), and using ground-based Cerenkov telescopes, including H.E.S.S. (Abramowski et al. 2012) and MAGIC (Aleksić et al. 2010) at the TeV scale.

Diffuse radio emission from the intracluster medium (ICM) in the form of approximately spherically symmetric halos and mini-halos has been observed from more than 40 clusters to date, indicating the existence of both a relativistic population of electrons/positrons and large-scale magnetic fields at the $\sim \mu$G level (for a review see e.g., Feretti et al. 2012). The origin of these relativistic particles responsible for the diffuse radio emission is, however, at present unclear. One possibility is that some fraction of these cosmic-ray electrons may be the result of dark matter annihilation (Colafrancesco et al. 2006; Pérez-Torres et al. 2009).

Most clusters show no or only low levels of detectable diffuse radio emission. However, Brown et al. (2011b) stacked a sample of 105 clusters with no detected radio halos and found a 6σ detection of radio emission, which suggests that even clusters with no currently observed radio emission host, at some level, both relativistic populations of electrons and positrons and large-scale, μG magnetic fields. The relativistic electrons and positrons produced by dark matter annihilation in clusters would synchrotron radiate away their energy in the presence of cluster-strength magnetic fields. There are many possible sources for the diffuse radio emission observed. However, the most conservative upper limits on the dark matter content in clusters through the use of radio emission comes from calculating how much dark matter annihilation would be required to produce the entire radio flux. In this chapter, we place limits on the dark matter annihilation cross section using primarily upper limits on or low levels of the diffuse radio emission from a selection of nearby clusters and also using some clusters with detected mini-halos. Our study greatly improves contraints on dark matter with radio observations over

previous studies by carefully selecting optimal targets with little or no observed diffuse radio emission, as opposed to clusters with bright radio halos that have been considered so far (see e.g. Colafrancesco et al. 2006).

The chapter is organized as follows. In Section 3.2, we describe our models for the dark matter and magnetic field profiles in clusters. In Section 3.3 we present the sample of clusters and radio data we employ for our analysis, report on the observation of diffuse emission from M49 and NGC4636, and discuss the impact of studies of intracluster magnetic fields on our sample. Section 3.4 presents limits on the dark matter annihilation cross section and discusses the implications and caveats of our results, including comparisons to previous studies and effects of uncertainties in the assumed dark matter profiles and magnetic field structure. We conclude in Section 3.5. Throughout this chapter, we assume a ΛCDM cosmology with $H_0 = 100h$ km s^{-1} Mpc^{-1}, $h = 0.70$, $\Omega_m = 0.27$, and $\Omega_\Lambda = 0.73$.

3.2 Dark Matter and Magnetic Field Modeling

The spectral flux density due to dark matter annihilation is:

$$S_\nu = \frac{\langle \sigma v \rangle}{8\pi m_\chi^2} \left(E \frac{dN_\nu}{dE} \right) J, \tag{3.1}$$

where $\langle \sigma v \rangle$ is the thermally-averaged zero-temperature dark matter annihilation cross section times velocity, m_χ is the dark matter particle mass, and $E dN_\nu/dE$ is the synchrotron energy spectrum per frequency per dark matter annihilation event. The observable flux density S_ν is typically measured in Jansky (Jy) in the radio. J is the line-of-sight integral of the dark matter density squared, integrated over the angular size of the emission region $\Delta\Omega$:

$$J = \int_{\Delta\Omega} \mathrm{d}\Omega \int_{los} \rho_\chi^2(l) \mathrm{d}l \tag{3.2}$$

We take the size of the emission region to match that of the available radio data, either the size of the observed diffuse emission or the size used to place upper limits. We use a number of different models for the dark matter density profile, described in the following sections.

3.2.1 NFW Density Profile

In our analysis we use four models for the dark matter density profile. The most conservative, with no substructure, is the Navarro-Frenk-White (NFW) profile (Navarro et al. 1996, 1997):

$$\rho_{NFW}(r) = \frac{\rho_s}{\frac{r}{r_s}\left(1+\frac{r}{r_s}\right)^2}, \tag{3.3}$$

where the central density ρ_s and the scale radius r_s are determined by observations. Following the derivation in Ackermann et al. (2010a), we use the scaling relationship derived from X-ray observations of clusters from Buote et al. (2007) to determine r_s and ρ_s from the virial mass and radius, M_{vir} and r_{vir}:

$$c_{vir} = 9\left(\frac{M_{vir}}{10^{14}h^{-1}}\right)^{-0.172}, \tag{3.4}$$

where the concentration $c_{vir} = r_{vir}/r_s$. The virial overdensity $\Delta_{vir} \approx 98$ is defined with respect to the critical density of the universe (Bryan & Norman 1998), with $M_{vir} = \frac{4\pi}{3}\Delta_{vir}\rho_c r_{vir}^3$. We determine M_{vir} and r_{vir} from M_{500}, where the overdensity is 500 times the critical density, obtained from X-ray observations (Chen et al. 2007). We correct M_{500} for our current cosmology and reduce it by the gas fraction f_{gas}, also reported in Chen et al. (2007), so that we are left with only the mass of the dark matter in the cluster: $M_{500} \rightarrow M_{500}(1-f_{gas})h$. We use the corrected M_{500} to determine r_{500} and use these parameters to determine M_{vir}, r_{vir}, and r_s using the following equations, derived in Appendix C of Hu & Kravtsov (2003):

$$\frac{M_{500}}{M_{vir}} = \frac{\Delta_{500}}{\Delta_{vir}}\left(\frac{r_{500}}{r_{vir}}\right)^3 \tag{3.5}$$

and

$$\Delta_{500} f(r_s/r_{vir}) = \Delta_{vir} f(r_s/r_{500}), \tag{3.6}$$

where

$$f(x) = x^3[\ln(1+x^{-1}) - (1+x)^{-1}]. \tag{3.7}$$

We use M_{vir}, r_{vir}, and r_s to solve for ρ_s (Hu & Kravtsov 2003):

$$\rho_s = \frac{M_{vir}}{4\pi f(r_s/r_{vir})} \tag{3.8}$$

3.2.2 Effects of Substructure

In cold dark matter (CDM) cosmologies, dark matter halos are structured hierarchically. Clusters are observed to host subhalos down to at least the scale of dwarf galaxies, approximately 10^7 $M_\odot$, and are predicted to contain substructure down to $\sim 10^{-6}$ $M_\odot$ (see Green et al. (2005), but also Profumo et al. (2006)). Since the J factor for dark matter annihilation is proportional to the density squared, the amount of substructure is critical, and can increase J by one or more orders of magnitude compared to a smooth NFW density profile. In clusters, tidal stripping tends to destroy subhalos near the cluster center, so substructure is preferentially found towards the cluster outskirts (Gao et al. 2012a). Generally the density profile of subhalos is more extended than the smooth central halo, as seen in simulations (Nagai & Kravtsov 2005; Gao et al. 2012a).

We consider here multiple substructure models. Two of these models are also used in Ackermann et al. (2010a): a conservative model, with a subhalo cutoff mass of 10^7 $M_\odot$ and a fraction of the total halo mass in substructure, f_s, of 10%, and an optimistic model, with a cutoff mass of 10^{-6} $M_\odot$ and f_s=0.2. We use the formalism in Colafrancesco et al. (2006) to determine the dark matter density profiles ρ_{CON} and ρ_{OPT}. In the notation of this framework, the conservative setup corresponds to a substructure contrast factor of $\Delta^2 = 1.3 \times 10^5$, and the optimistic setup corresponds to $\Delta^2 = 3.0 \times 10^5$.

We also consider a third model based on the results of the Phoenix Project, which is a series of dark matter simulations following the evolution of cluster-sized halos (Gao et al. 2012a,b). These simulations adopt the cosmological parameters of the Millenium Simulation (Springel et al. 2005), which are now known to be inconsistent with current cosmological parameters. However, the main difference is the value of σ_8, which affects the number of clusters in a universe-sized simulation but not the properties of individual cluster halos. This model adopts a cutoff subhalo mass of 10^{-6} $M_\odot$, resulting in a subhalo mass fraction of approximately 27%, and is more extended than either of the previous models.

The Phoenix simulations use M_{200} and r_{200} to express their results in terms of

a boost factor and substructure surface brightness (Gao et al. 2012a):

$$b(M_{200}) = 1.6 \times 10^{-3} \left(\frac{M_{200}}{M_\odot} \right)^{0.39} \tag{3.9}$$

$$S_{sub}(r) = \frac{16 b(M_{200}) L_{main}}{\pi \ln(17)} \frac{1}{r^2 + 16 r_{200}^2}, \tag{3.10}$$

where L_{main} is the luminosity of the smooth halo, which is well-described by an NFW profile. We use Equations (3.5) and (3.6) to solve for M_{200} and r_{200}, defined through the overdensity $\Delta_{200} = 200\rho_c$, from M_{500} and r_{500}. We then translate Equation. (3.10) to a J-factor "surface brightness", following Han et al. (2012a). Thus the resulting J factor for the Phoenix simulations is:

$$J_{PHX} = J_{NFW} + J_{sub} \tag{3.11}$$

where

$$J_{sub} = \int_{\Delta\Omega} \mathrm{d}\Omega \int \frac{16 b(M_{200}) J_{NFW}}{\pi ln(17)} \frac{2\pi r \mathrm{d}r}{r^2 + 16 r_{200}^2} \tag{3.12}$$

3.2.3 Electron/Positron Signal from Dark Matter Annihilation

In order to characterize the synchrotron spectrum, we need the equilibrium electron and positron spectra, which result by solving the full diffusion equation:

$$\begin{aligned} \frac{\partial}{\partial t} \frac{dn_e}{dE} = & \nabla \left[D(E, \mathbf{x}) \nabla \frac{dn_e}{dE} \right] \\ & + \frac{\partial}{\partial E} \left[b_{loss}(E, \mathbf{x}) \frac{dn_e}{dE} \right] + Q(E, \mathbf{x}) \end{aligned} \tag{3.13}$$

where dn_e/dE is the equilibrium electron or positron density spectrum, $Q(E, \mathbf{x})$ is the source term, $D(E, \mathbf{x})$ is the spatial diffusion coefficient, and $b_{loss}(E, \mathbf{x})$ is the energy loss term described below. The source term is proportional to the injected spectrum of electrons/positrons per dark matter annihilation.

The first term on the right-hand side describes the spatial diffusion of the electrons/positrons. If we assume these electrons/positrons diffuse at approximately the Alfvén velocity ($\sim$ 100 km s^{-1}; see e.g., Feretti et al. 2012), the diffusion

time scale across a typical radio halo (hundreds of kpc to a few Mpc) is much longer than the energy loss time scale for synchrotron radiation for particles with $E \gtrsim 1$ GeV. Following a more careful treatment of spatial diffusion in in Appendix A of Colafrancesco et al. (2006), we still find the synchrotron loss time scale is much shorter than the diffusion time across a radio halo; we therefore assume that diffusion is negligible for clusters.

Diffusion may be important for galaxy groups, as the emission regions is quite small ($30 - 35$ kpc, see Section 3.3.1). However, due to numerous uncertainties in estimating the diffusion coefficient for galaxy groups, especially the magnetic field structure, we still choose to ignore diffusion. The effect of diffusion would be to smooth out the equilibrium electron/positron spectrum with respect to the underlying dark matter distribution, ultimately leading to less stringent DM limits. However the galaxy groups do not yield the best limits on the dark matter annihilation cross section; see Section 3.4 for further discussion of the results.

Assuming no spatial diffusion, can neglect the first term on the right-hand side of Equation 3.13. Since we are interested in the time-independent equilibrium electron/positron density spectrum, we set the left-hand side to zero. The expression for the equilibrium density spectrum is:

$$\frac{dn_e}{dE} = \frac{\langle \sigma v \rangle \rho_\chi^2}{2m_\chi^2 b_{loss}(E)} \int_E^{m_\chi} \mathrm{d}E' \frac{dN_{e,inj}}{dE'} \tag{3.14}$$

We use the DMFIT package (Jeltema & Profumo 2008) (in turn derived from the DarkSUSY package (Gondolo et al. 2004)) to calculate the electron/positron injection spectra per dark matter annihilation. The energy loss term, in the low redshift limit, is the sum of synchrotron, IC, bremsstrahlung, and Coulomb losses:

$$
\begin{aligned}
b_{loss}(E) &= b_{syn} + b_{IC} + b_{brem} + b_{coul} \\
&\approx 0.0254 \left(\frac{E}{1\text{GeV}}\right)^2 \left(\frac{B}{1\mu\text{G}}\right)^2 \\
&+ 0.25 \left(\frac{E}{1\text{GeV}}\right)^2 \\
&+ 1.51n(0.36 + \log(\gamma/n)) \\
&+ 6.13n(1 + \log(\gamma/n)/75)
\end{aligned}
\tag{3.15}
$$

The energy loss term has units of 1×10^{-16} GeV s^{-1}, where n is the average thermal electron density, $\approx 1 \times 10^{-3}$ cm^{-3} for all clusters. For GeV electrons and positrons, synchrotron and IC losses dominate; when $B > B_{CMB} \approx 3$ μG, synchrotron losses dominate over IC losses.

3.2.4 Synchrotron Emission

Relativistic electrons in clusters of galaxies radiate their energy via synchrotron emission in the presence of a magnetic field $B(r)$, and live in a background plasma with electron density $n(r)$ and plasma frequency $\nu_p = 8890[n(r)/1\text{ cm}^{-3}]^{1/2}$ Hz. The power per frequency of emitted synchrotron radiation for a single electron (or positron) with energy $E = \gamma m_e c^2$, averaged over all incoming directions is (Longair 2011):

$$
P_\nu(\nu, E) = \int_0^\pi \mathrm{d}\theta \frac{\sin\theta}{2} 2\pi\sqrt{3} r_0 m_e c \nu_0 \sin\theta F\left(\frac{x}{\sin\theta}\right) \tag{3.16}
$$

where $r_0 = e^2/(mc^2)$ is the classical electron radius, θ is the pitch angle, $\nu_0 = eB/(2\pi mc)$ is the nonrelativistic gyrofrequency. The quantities x and F are defined as follows:

$$
x \equiv \frac{2\nu}{3\nu_0\gamma^2}\left[1 + \left(\frac{\gamma\nu_p}{\nu}\right)^2\right]^{3/2} \tag{3.17}
$$

$$
\begin{aligned}
F(s) &\equiv s\int_s^\infty K_{5/3}(\xi)\mathrm{d}\xi \\
&\approx 1.25 s^{1/3}\exp(-s)[648 + s^2]^{1/12}
\end{aligned}
\tag{3.18}
$$

where $K_{5/3}(\xi)$ is the modified Bessel function of order 5/3.

The synchrotron energy spectrum per frequency, EdN_ν/dE, given populations of electrons and positrons each with an equilibrium density spectrum dn_e/dE_e is:

$$E\frac{dN_\nu}{dE} = \frac{2m_\chi^2}{\langle\sigma v\rangle\rho_\chi^2}\int_{m_e}^{m_\chi}\left(\frac{dn_{e^-}}{dE}+\frac{dn_{e^+}}{dE}\right)P_\nu \mathrm{d}E \tag{3.19}$$

This energy spectrum is inserted into Equation (3.1) to find the limits on the annihilation cross section.

3.2.5 Magnetic Field Model

Synchrotron emission depends strongly on the magnetic field in the region of interest. From MHD simulations and from clusters with multiple Faraday RMs, the magnetic field appears to follow the gas density (Murgia et al. 2004; Bonafede et al. 2010; Vacca et al. 2012). The gas density is typically fit with a β model (Cavaliere & Fusco-Femiano 1976); we adjust the radial dependence with a free parameter η:

$$B(r) = B_0\left[\left(1+\left(\frac{r}{r_c}\right)^2\right)^{-(3/2)\beta}\right]^\eta \tag{3.20}$$

where B_0 is the central magnetic field value and r_c is the core radius. The parameters β and r_c are fit using X-ray data, and B_0 and η are typically modeled based on a combination of simulations and RMs (e.g., for Coma, Bonafede et al. 2010).

We weight the magnetic field distribution by the dark matter density profile to yield a single parameter, an effective magnetic field B_{eff} that is used in our synchrotron spectrum calculations:

$$B_{eff} = \left[\frac{\int_0^{r_h} B(r)^2\rho_\chi^2 r^2 \mathrm{d}r}{\int_0^{r_h}\rho_\chi^2 r^2 \mathrm{d}r}\right]^{1/2} \tag{3.21}$$

where r_h is the radius of the considered emission region, either that of the observed diffuse emission region or the region used to place an upper limit. This weighting of the magnetic field yields a better estimate of the field in the regions where most of the synchrotron emission is originating from, i.e., regions with high dark matter densities.

3.3 Cluster Sample: Radio and Magnetic Field Data

3.3.1 Selection of Clusters from Radio Data

We choose our sample based on radio, X-ray, and magnetic field data available from the literature. The clusters that produce the best limits on dark matter annihilation are nearby and do not host observable radio halos, or host only low levels of central diffuse emission or mini-halos. Unfortunately, there are very few published upper limits on the diffuse radio emission in clusters. Rudnick & Lemmerman (2009) published the most comprehensive list of upper limits (96% confidence limit) on Mpc-sized radio emission for bright X-ray clusters with redshifts between 0.03 and 0.3 at 327 MHz with the Westerbork Northern Sky Survey. Upper limits on Mpc-sized emission from clusters with $0.2 < z < 0.4$ were published in Venturi et al. (2008) using the Giant Metrewave Radio Telescope at 610 MHz. Since the astrophysical J factor decreases with increasing distance, nearby clusters are the best candidates for dark matter detection; we therefore restrict our sample to $z < 0.1$. Only a handful of clusters in Rudnick & Lemmerman (2009) have redshifts of less than 0.1. Additionally, to facilitate comparisons, our sample of clusters largely overlaps with those considered for gamma-ray analysis (e.g., Ackermann et al. 2010a; Huang et al. 2012).

We take β model parameters, cluster masses, and gas fractions from the HIFLUGCS catalog of nearby, massive, bright X-ray galaxy clusters (Chen et al. 2007). Four clusters with published radio halo upper limits from Rudnick & Lemmerman (2009) are also part of the HIFLUGCS catalog.

We include three additional clusters in HIFLUGCS that have detected mini-halos: Perseus, Ophiuchus, and A2029 (Murgia et al. 2009, 2010). Despite the detected radio flux from these clusters, they are strong candidates because they host cool cores, and thus have higher inferred central magnetic field strengths, and are also nearby and heavily dark matter dominated. Perseus and Ophiuchus especially are considered to be among the best candidates for dark matter searches

(Jeltema et al. 2009).

Coma is also included in our sample, as it has both a very well-studied radio halo (Kim et al. 1990) and magnetic field (Bonafede et al. 2010), and is generally used as a representative massive, merging cluster. It is also the only cluster that has been used previously to place constraints on the dark matter content in clusters using radio data (Colafrancesco et al. 2006) and is frequently considered in analyses of dark matter annihilation in clusters, especially in gamma rays (e.g., most recently in Han et al. 2012a). We show that it produces comparably poor limits on the dark matter annihilation cross section due to the large observed radio emission, for a smooth NFW dark matter profile with a final annihilation state of $b\bar{b}$ in Fig. 3.3; we find that Coma yields poor limits for other dark matter profiles and annihilation channels as well.

Finally, we searched for diffuse radio emission using the NRAO VLA Sky Survey (NVSS; Condon et al. 1998) at 1.4 GHz for some of the best candidate clusters for dark matter detection which do not have published radio upper limits or detections, including Virgo, Fornax, AWM7, and two Virgo groups, M49 and NGC4636. While NVSS is not an optimal survey to search for extended emission, since the sensitivity of NVSS steeply decreases with the increase in size of the emission region, it happens to be the best option for the selected objects, and we have corrected for the loss of NVSS sensitivity as a function of size where needed. We ultimately exclude Virgo and Fornax as they both contain very bright radio sources that likely wash out any true diffuse emission.

For AWM7, we find no detected diffuse radio emission in the NVSS images. We consider a circular emission region with a diameter of ~ 2 core radii, $\sim 11'$, and using a multiresolution filtering technique as used by Rudnick & Lemmerman (2009), we remove bright compact sources and place a 3σ upper limit on the diffuse flux from that region, corrected for the sensitivity losses of NVSS for very extended emission.

We do find extended radio emission in the NVSS from M49 and NGC4636 extending beyond the bright emission from the central galaxies, after removing the emission from compact and slightly resolved sources using a multiresolution

filtering technique as used by e.g., Rudnick & Lemmerman (2009). The resulting extended emission from M49 is approximately $\sim 30-35$ kpc $(6-7')$ in diameter with a flux density of 40 mJy, much larger and fainter than the ~ 220 mJy emission from the central, Seyfert 2 elliptical galaxy (Dunn et al. 2010; Brown et al. 2011a). NGC4636 shows diffuse emission over a ~ 36 kpc $(7')$ range with a flux density of 30 mJy. The central source of NGC4636 shows clear jet-like structure and is approximately 5 kpc in size at 610 MHz (Baldi et al. 2009; Giacintucci et al. 2011), and this structure is not visible at 1.4 GHz at the lower resolution of the NVSS, whereas the diffuse emission at 1.4 GHz is larger and more spherical in shape. We note that the core of NGC4636, ~ 15 kpc in size, has a complex morphology in the X-ray and radio which may be due to AGN outbursts (e.g., Jones et al. 2002; Baldi et al. 2009). It is possible that the larger diffuse emission observed in NVSS may be partly due to older outbursts by a central AGN; however, we choose to derive upper limits by calculating the amount of dark matter annihilation needed to account for all of this observed diffuse emission, which yields the most conservative upper limits on the dark matter annihilation cross section. Diffuse central emission at 1.4 GHz has not been previously identified in either group. Images of the diffuse emission for M49 and NGC4636 are shown in Figs. 3.1 and 3.2, respectively.

3.3.2 Magnetic Fields in Clusters

The observation of diffuse radio emission in galaxy clusters requires the presence of large-scale magnetic fields associated with the ICM. Intracluster magnetic fields can be inferred from the Faraday rotation of polarized radiation of individual sources with typical central values of $\sim 1-10$ μG (e.g., Eilek & Owen 2002; Bonafede et al. 2010; Vacca et al. 2012). Clusters with cool cores can have higher inferred central magnetic field strengths, $\sim 10-40$ μG (Taylor et al. 2002, 2006; Kuchar & Enß lin 2011). Magnetic fields in clusters can also be estimated using radio halo observations assuming equipartition of cosmic ray and magnetic energy densities; these estimates are typically between $0.1-1$ μG and are taken as lower

limits (e.g. Govoni & Feretti 2004; see also Carilli & Taylor 2002 for a review of magnetic fields in clusters).

Turbulence due to past mergers can amplify magnetic fields in clusters to μG levels (e.g., Dolag et al. 2002; Subramanian et al. 2006; Ryu et al. 2008), and can also accelerate particles, which may be responsible for the giant radio halos observed in some clusters (e.g., Brunetti & Lazarian 2011b and references therein). If mergers drive radio halos, then the difference between clusters with and without halos may be dynamical: clusters with halos have suffered a merger in their recent past, while clusters without halos are more dynamically relaxed, with no recent mergers in their history (Brunetti et al. 2009; Cassano et al. 2010). Assuming clusters evolve in this way, it is natural to infer that at some point the cluster magnetic field will dissipate and suppress the synchrotron radiation producing halos (Brunetti et al. 2009; Cassano et al. 2010). However, theoretical studies and simulations of clusters show that large-scale magnetic fields are long-lived, $\sim 4-5$ Gyr (Subramanian et al. 2006), which is longer than the cosmic-ray electron/positron lifetime, and thus longer than the lifetime of the radio halo, about 1 Gyr (Brunetti et al. 2009). Additional theoretical work on the ICM by Kunz et al. (2011), in which heating by local plasma instabilities can stabilize cooling in the ICM, predicts $\sim 1-10$ μG magnetic field strengths that scale weakly with gas density and generally agree with values estimated from RMs for specific clusters.

Only a handful of clusters have well-studied magnetic fields; less than half of our sample have published studies on their magnetic fields. For the clusters that are not strong cool cores as defined by Hudson et al. (2010) but do not have any published information about their magnetic fields, we use the best fit values of B_0 and η for Coma from Bonafede et al. (2010), which we call the non-cool-core model, as Coma is a well-studied non-cool-core cluster. The magnetic field in clusters may turn out to be connected to the presence of a radio halo in such a way that clusters without observed halos have lower magnetic fields than those with halos (e.g., Brunetti et al. 2009). However, we choose to use the magnetic field parameters derived for Coma even for clusters with upper limits on the radio

emission. This is because RM studies yield no differences in the RMs, and thus inferred magnetic fields, of clusters with and without radio halos (Clarke et al. 2001; Govoni et al. 2010).

Cool core clusters generally have higher inferred central magnetic field strengths than clusters without cool cores (Kuchar & Enß lin 2011). In our sample both A2029 and Perseus have published central field strengths from RMs (Eilek & Owen 2002 and Taylor et al. 2006, respectively). A2199 is the only cool core cluster in our sample with best fit values for both B_0 and η from Faraday RMs (Vacca et al. 2012). Ophiuchus, also a cool core cluster, has a published RM from a radio galaxy outside the cool core region and therefore no estimated central magnetic field strength (Govoni et al. 2010). It has one of the hottest known cool cores (Fujita et al. 2008), which could mean its central magnetic field is somewhere between that of a strong cool core cluster and a cluster with no cool core. We therefore choose the more conservative, non-cool-core model to estimate the magnetic field of Ophiuchus when comparing constraints from other clusters, but we also show how our constraints change if we use the central magnetic field value of Perseus, the prototypical cool-core cluster. We discuss the effects of the uncertainty on the magnetic field on dark matter constraints, specifically with respect to Ophiuchus and A2199, further in Section 3.4.3.

Little is known about the magnetic field strengths for groups of galaxies, especially in/near the central elliptical galaxies that typically dominate these groups. We choose to use the non-cool-core model for the magnetic field in calculating the limits for the two Virgo groups in our sample, M49 and NGC4636. These groups are heavily dominated by their central elliptical galaxies, which must host magnetic fields of their own. large-scale galactic magnetic fields of normal galaxies are typically in the μG range (e.g., for the Milky Way, Noutsos 2012). We choose therefore to use the non-cool-core model for the magnetic fields of these groups, the central strength of which is probably comparable to or lower than the strength of the field within the central galaxy. Cluster properties, radio data, and magnetic field parameters are listed in Table 3.1.

3.4 Results and Discussion

We derive constraints on the dark matter annihilation cross section by assuming conservatively that the radio upper limits or low levels of observed emission in a sample of nearby galaxy clusters are due to synchrotron emission from electrons and positrons produced by annihilating dark matter. In Fig. 3.3, we present the cross section upper limits for all the clusters in our sample, each with an NFW dark matter profile, for the $b\bar{b}$ annihilation channel. For this dark matter profile, the Virgo groups NGC4636 and M49 yield the tighest constraints, while the best constraints are produced by A2199 for massive clusters with published radio data at low dark matter particle masses and by Ophiuchus at higher masses. Perseus, which hosts a particularly bright mini-halo, produces the weakest constraints. As expected, the constraints from the Coma Cluster, with its bright, giant radio halo, are also relatively poor.

We also consider four different annihilation channels: $b\bar{b}$, $\tau^+\tau^-$, $\mu^+\mu^-$, and W^+W^-. In Figures 3.4 and 3.5 we show the limits for each of the different channels for A2199 and Ophiuchus, using an NFW dark matter profile. The $\tau^+\tau^-$ and $\mu^+\mu^-$ channels, which tend to produce more electrons and positrons per annihilation than $b\bar{b}$, yield the best limits at lower particle masses, while the $b\bar{b}$ yields better limits at higher masses, which is generally true of all the clusters.

3.4.1 Comparison to Limits from Gamma-Ray Emission

Many previous studies of clusters have focused on the potential gamma-ray emission from dark matter annihilation, typically using data from *Fermi* (Ackermann et al. 2010a; Ando & Nagai 2012; Huang et al. 2012; Nezri et al. 2012; Han et al. 2012b). Using gamma rays to investigate the dark matter content of clusters has the advantage that the emission only depends on the underlying particle population(s) and chosen dark matter profile, and does not depend on other cluster properties, e.g., the magnetic field. However, only very nearby clusters produce useful limits, and clusters that are near the Galactic plane or contain a point source that is bright in gamma rays must be excluded from these studies, as

the Galactic plane is gamma-ray bright and the resolution of *Fermi* and ground-based gamma-ray telescopes is poor compared to radio telescopes. A2199 and Ophiuchus, which yield the best limits in many cases in the radio, are typically not considered for gamma-ray analysis, as A2199 is too far away, and Ophiuchus is very near the Galactic center, a very bright gamma-ray region. Comparing the limits for A2199 for dark matter annihilating to $b\bar{b}$ with a smooth NFW profile to the limits derived for Fornax, also for $b\bar{b}$ and an NFW profile, in Huang et al. (2012), which are the best limits derived from gamma rays from a single cluster with an NFW profile to date, our limits from A2199 are approximately a factor of ~ 3 or more across a wide range of masses.

Han et al. (2012a), using the results of the Phoenix simulations to model substructure and considering the possibility that the gamma-ray emission from clusters is extended, placed constraints on dark matter annihilation in Coma, Virgo and Fornax that are comparable to or better than the limits derived in Huang et al. (2012) including substructure. Our limits from A2199 when considering the same substructure model from the Phoenix simulations, are comparable to those reported in Han et al. (2012a).

3.4.2 Substructure in Clusters and Groups

The boost factors obtained by using the the Phoenix simulations are $\gtrsim 10$ times larger than the boost factors derived from our other adopted substructure models, which in turn yield limits that are 1–2 orders of magnitude tighter. This is reflected in Fig. 3.6, which shows the limits for the $b\bar{b}$ annihilation channel for our four adopted dark matter profiles for A2199. The limits from our conservative and optimistic models are only slightly better than those produced by an NFW profile, about $10-30\%$. The limits that result from using the Phoenix profile are much lower, almost 2 orders of magnitude for A2199, and dip below the nominal thermal annihilation cross section 3×10^{-26} cm^3 s^{-1} for masses $\lesssim 400$ GeV. A similar pattern is true for most other clusters, except M49 and NGC4636. This is because the emission region is so small for these groups that the J factors only

change by at most a factor of four as the amount of substructure is increased, while for other clusters the difference between J_{NFW} and J_{PHX} is typically $2-3$ orders of magntitude.

3.4.3 Uncertainties in Cluster Masses and Magnetic Fields

Aside from the assumed dark matter profile and amount of substructure, the two main sources of uncertainty in the limits on the dark matter annihilation cross section are the cluster mass, reported by Chen et al. (2007), and the uncertainty in the magnetic field parameters B_0 and η. Chen et al. (2007) also report uncertainties in the gas fraction, the core radius, and β; we find that the uncertainties associated to these quantities are, however, negligible compared to the cluster mass and magnetic field uncertainties.

In Fig. 3.7, we show the relative magnitudes of the various sources of uncertainty for one of the best cluster candidates, A2199. The uncertainty in the mass leads to an uncertainty in the J factors which is generally a factor of $\lesssim 2$ or smaller for all the clusters in our sample. For the uncertainty in the magnetic field of A2199, we choose values for B_0 and η that best represent the spread in the B_0–η contour plot in Figure 9 of Vacca et al. (2012). The uncertainty in the magnetic field is comparable to the uncertainty in the cluster mass at lower dark matter masses, leading to uncertainties in the annihilation cross section of about a factor of 2. At higher masses, the magnetic field uncertainty translates to only about a 10% uncertainty in the limits while the uncertainty in cluster mass remains constant. This is because the total radio energy per frequency, and thus the annihilation cross section, depends on the magnetic field to a power proportional to the index of the underlying electron/positron distribution. The electron/positron distribution produced by lower mass dark matter particles is generally steeper than the distribution produced by higher mass dark matter particles, so the magnetic field is more important at lower dark matter masses than at higher masses.

A2199 is a cool-core cluster (e.g., Hudson et al. 2010) and is therefore more

likely to host a small mini-halo hundreds of kpc in size rather than a giant, Mpc-sized radio halo, as we assumed here based on the upper limits available in the literature (Rudnick & Lemmerman 2009). It is also possible that the magnetic field determined by Vacca et al. (2012) is only relevant inside the cool core region. However, a smaller emission region would likely not change our results much, since the dark matter distribution and thus emission from dark matter is highly centrally peaked (except perhaps in the case of the Phoenix simulations, where the dark matter distribution is much flatter).

While Ophiuchus yields some of the best limits for the $\tau^+\tau^-$ and $\mu^+\mu^-$ annihilation channels, its magnetic field is not well understood. Ophiuchus has a claimed detection of nonthermal hard X-ray emission from a deep INTEGRAL observation (Eckert et al. 2008; see also Profumo 2008). The magnetic field strength of Ophiuchus has been estimated to be around 0.1 μG using this observation combined with radio data, assuming the hard X-ray emission is due to the IC scattering of the same population of relativistic electrons that are the source of the radio emission due to synchrotron losses (Eckert et al. 2008; Pérez-Torres et al. 2009; Nevalainen et al. 2009). This is inconsistent with the larger magnetic fields inferred from Faraday RMs in similar clusters.

Both approaches to measuring cluster magnetic fields rely on several assumptions. The field strength calculated using hard X-ray emission is typically a volume average over the size of the emission region, and it assumes that the field is uniform, while simulations point to a field that decays radially with gas density (e.g., Donnert et al. 2009). Additionally, assumptions must be made about the energy spectrum and origin of the cosmic-ray lepton population in order to match the observed X-ray and radio emission that potentially conflict with other observations, e.g. in gamma rays (Colafrancesco & Marchegiani 2009).

RMs rely on the gas density along the line of sight. Turbulence could distort the gas density and therefore the magnetic field along the line of sight. Additionally, it is possible that most of the contribution to an observed RM is due to the local environment around the radio source itself, implying the inferred magnetic fields may not be representative of what is happening in the ICM (Rudnick & Blundell

2003, however see also Ensslin et al. 2003).

We choose to use field estimates based on RMs of other clusters for Ophiuchus, setting the non-cool-core model as the lower limit, and the field of Perseus, a cluster with a strong cool core, as the upper limit. We show the effect of the uncertainty in the magnetic field of Ophiuchus in Fig. 3.8 by varying B_0 with η fixed at 0.5. The limits vary by approximately a factor of 7 for a mass of 10 GeV, and a factor of 1.3 at 1000 GeV.

3.5 Conclusions

In this chapter, we present new limits on the dark matter annihilation from radio nondetections and marginal detections of galaxy clusters. Overall, the limits derived from upper limits on radio halos in massive clusters, low levels of observed central diffuse emission in galaxy groups, and detections of mini-halos in cool core clusters are better than previously derived limits using non-detections in gamma rays for the same substructure model and annihilation channel by a factor of ~ 3 or more, despite our conservative assumptions. We consider four dark matter pair-annihilation channels in our analysis; channels that produce harder leptons ($\tau^+\tau^-$ and $\mu^+\mu^-$) yield better limits at lower masses, as expected, while at higher masses, $b\bar{b}$ yields the best limits. However, our limits depend strongly on both the assumed amount of substructure, which is also true for limits derived from gamma-ray nondetections, and the chosen magnetic field model for any individual cluster.

The clusters that yield the most strigent limits, A2199 and Ophiuchus, are not necessarily the best targets for dark matter analysis with gamma rays. This implies that dark matter studies with radio observations can rely on a different set of objects than studies with gamma-ray observations, indicating that radio studies can be complementary to gamma-ray studies.

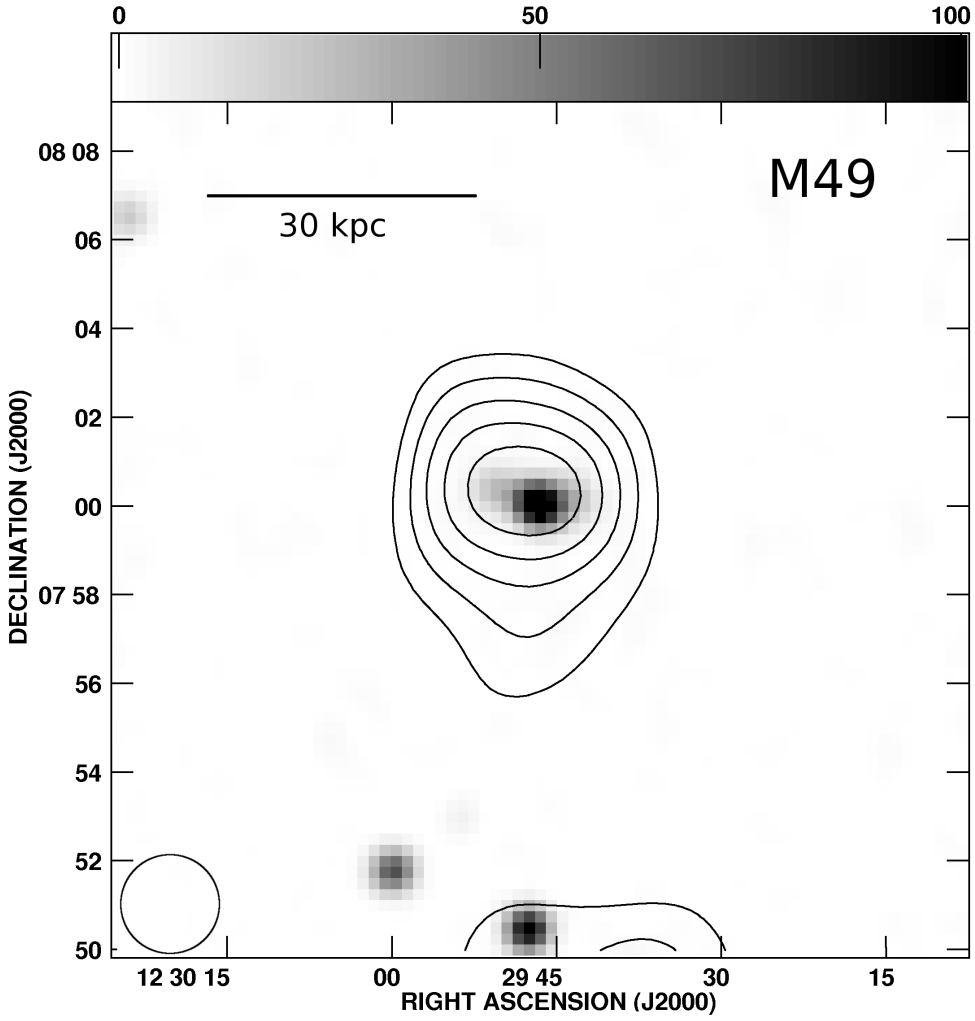

Figure 3.1: Greyscale image of M49 from NVSS, 45" resolution, on a scale of 0-100 mJy/45" beam. Contours show the residual diffuse emission at a resolution of 135", as shown in the lower left, after subtraction of the compact emission. Contour levels are at 2 mJy/135" beam $\times$ (1,2,3,...).

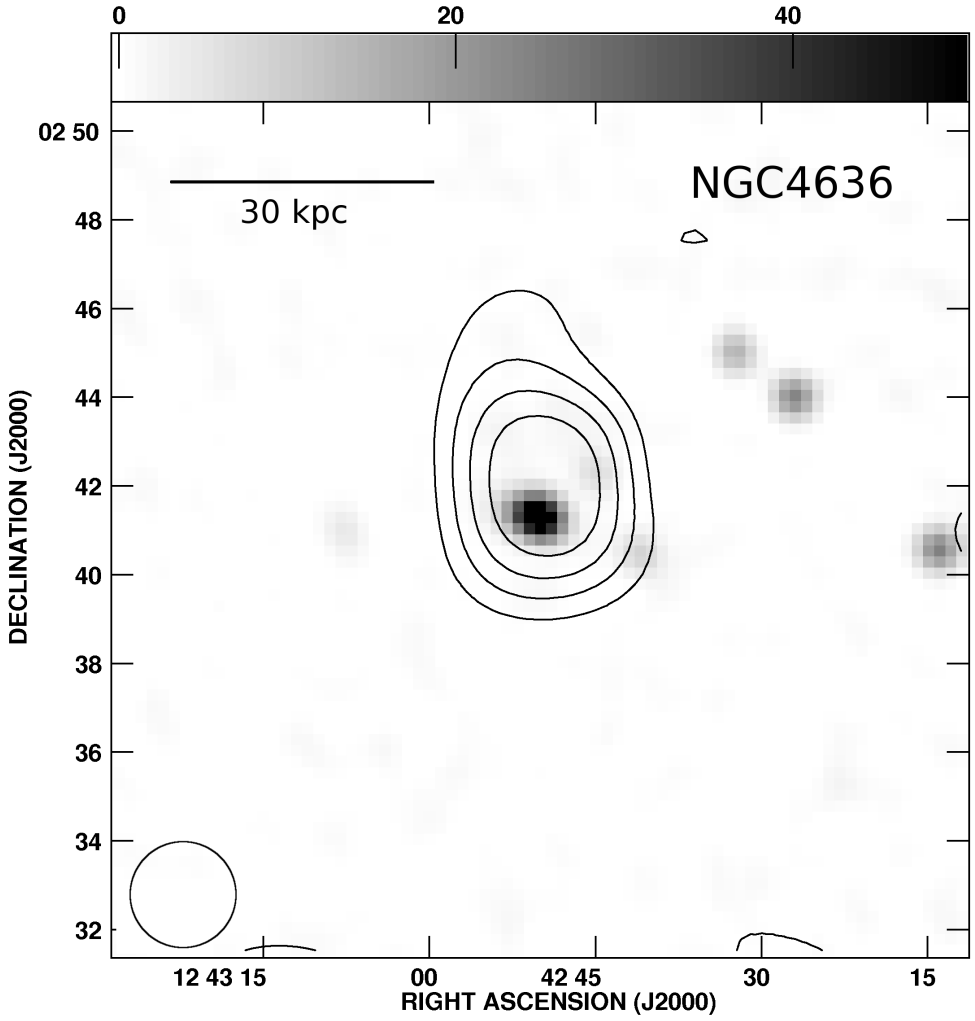

Figure 3.2: Greyscale image of NGC4636 from NVSS, 45" resolution, on a scale of 0-50 mJy/45" beam. Contours show the residual diffuse emission at a resolution of 135", as shown in the lower left, after subtraction of the compact emission. Contour levels are at 2 mJy/135" beam $\times$ (1,2,3,...).

Table 3.1: Galaxy Cluster Properties

Name	z	M_{vir} (10^{14} $M_\odot$)	β	r_c (kpc)	ν (MHz)	S_ν (Jy)	R_h (Mpc)	Radio Ref.	B_0 (μG)	B_0 Ref.
A0576	0.0381	4.80	0.825	277	327	<0.20	0.5	1	...	...
A2199	0.0302	4.18	0.655	98	327	<0.025	0.5	1	11.7	4
A2244	0.0970	5.14	0.607	88	327	<0.08	0.5	1	...	...
Zw1742[a]	0.0757	11.1	0.717	163	327	<0.10	0.5	1	...	...
Perseus	0.0183	5.04	0.540	44	1400	1.979	0.069	2	25	5
Ophiuchus	0.0280	48.4	0.747	196	1400	0.1064	0.315	2	...	...
A2029	0.0767	9.62	0.582	58	1400	0.0188	0.125	2	16.0	6
Coma	0.0232	9.88	0.654	241	1400	0.64	0.415	3	4.7	7
AWM7	0.0172	4.92	0.671	122	1400	<0.107	0.122	*	...	...
M49	[b]	0.67	0.592	7	1400	0.040	0.016	*	...	...
NGC4636	[c]	0.18	0.491	4	1400	0.030	0.018	*	...	...

Notes. Cluster masses taken from Chen et al. (2007), corrected for gas fraction and current cosmology (see text). Listed values for z, β and r_c also taken from Chen et al. (2007) (r_c corrected for current cosmology). For all clusters except A2199, we assume $\eta = 0.5$. We use $\eta = 0.9$ for A2199, consistent with Vacca et al. (2012). For clusters with no listed B_0, we assume $B_0 = 4.7\mu$G and $\eta = 0.5$, i.e., our non-cool-core model.

[a] Full name for Zw1742 is ZwCl1742.1+3306.

[b] Distance calculated from a distance modulus of 31.15, from Villegas et al. (2010), rather than a redshift.

[c] Distance calculated from a distance modulus of 31.24, from Dirsch et al. (2005), rather than a redshift.

References. *This chapter. (1) Rudnick & Lemmerman (2009); (2) Murgia et al. (2009); (3) Kim et al. (1990); (4) Vacca et al. (2012); (5) Taylor et al. (2006); (6) Eilek & Owen (2002); (7) Bonafede et al. (2010).

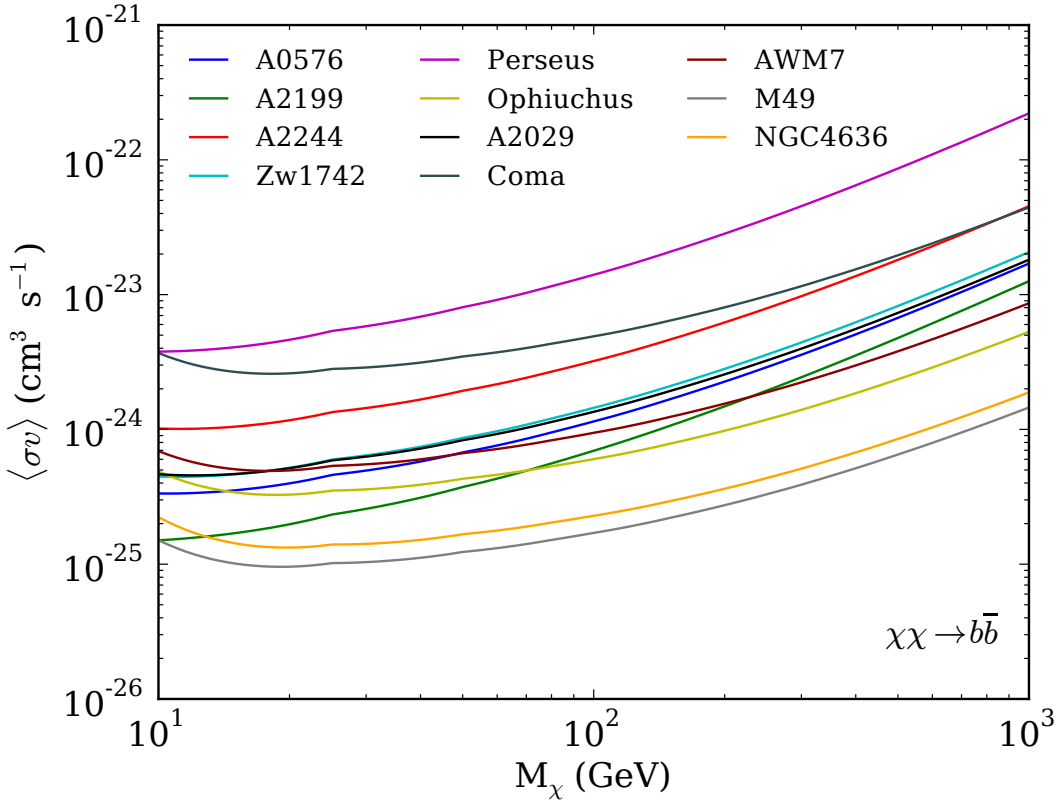

Figure 3.3: Dark matter annihilation cross section upper limits for all clusters in the sample; we assume a smooth NFW dark matter density profile.

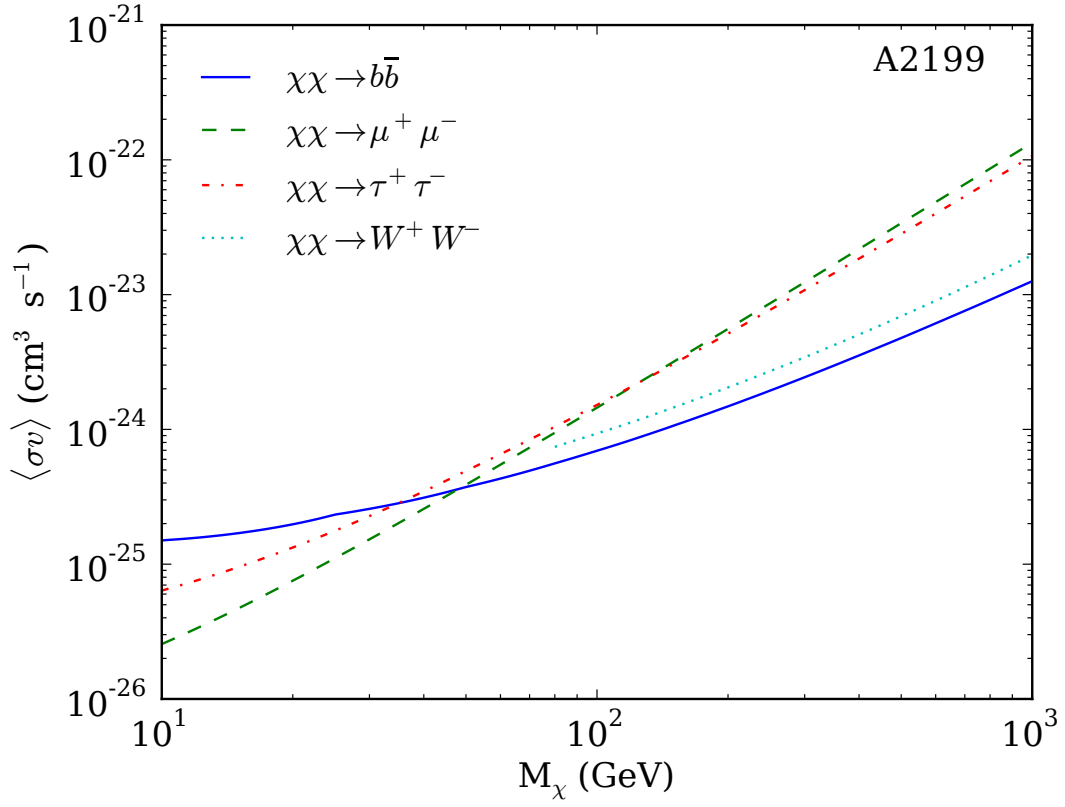

Figure 3.4: Dark matter annihilation cross section upper limits for A2199, for four annihilation channels, with a smooth NFW dark matter profile only.

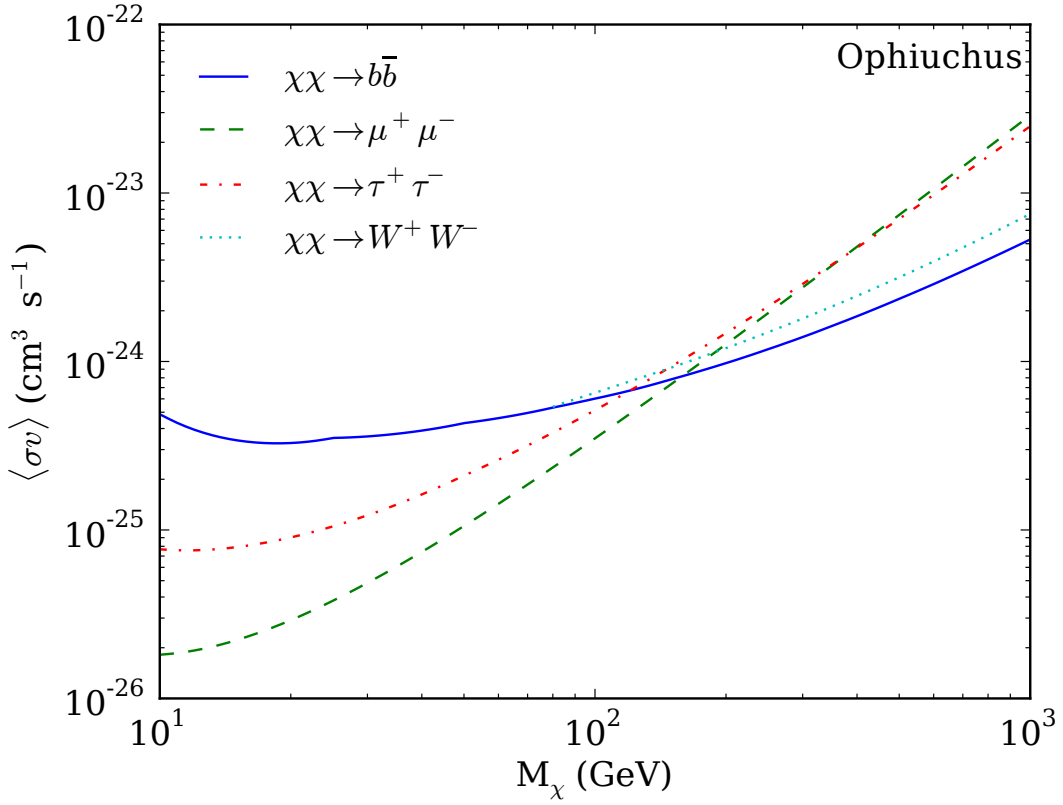

Figure 3.5: Dark matter annihilation cross section upper limits for Ophiuchus, for four annihilation channels, with a smooth NFW dark matter profile only. We use a central magnetic field value of 4.7μG and $\eta = 0.5$ (our non-cool-core model) in deriving these constraints.

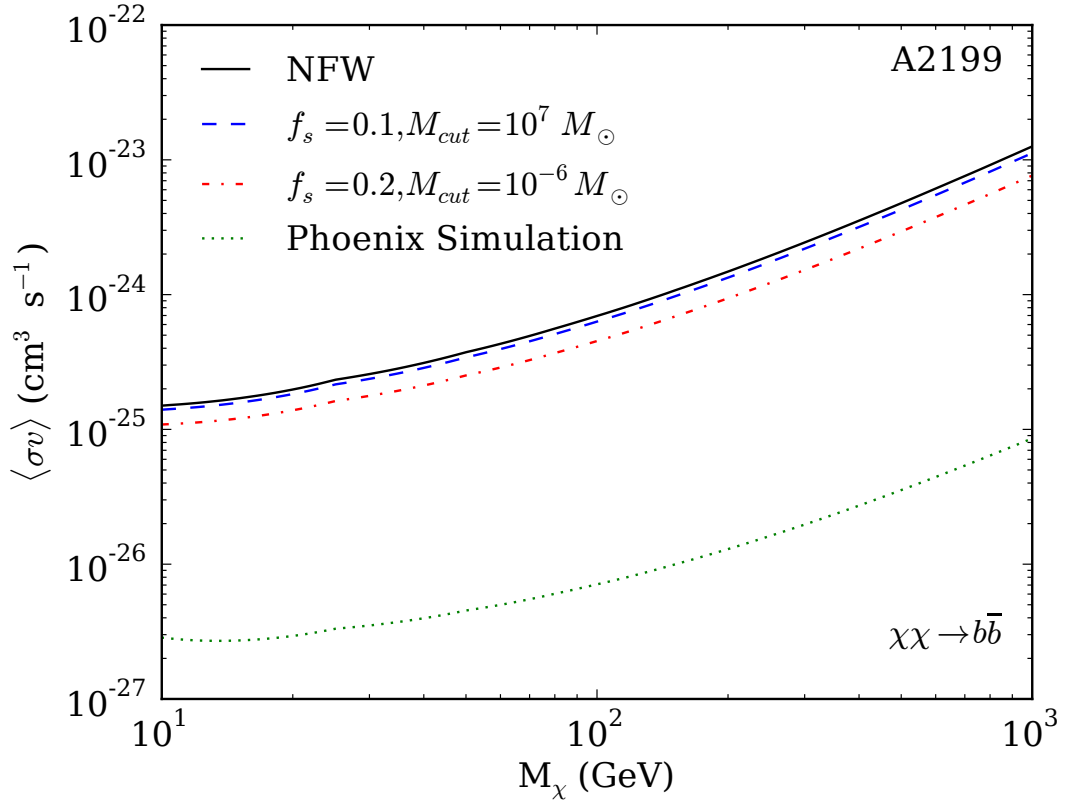

Figure 3.6: Dark matter annihilation cross section upper limits for A2199, for one annihilation channel ($b\bar{b}$) and our four different substructure models.

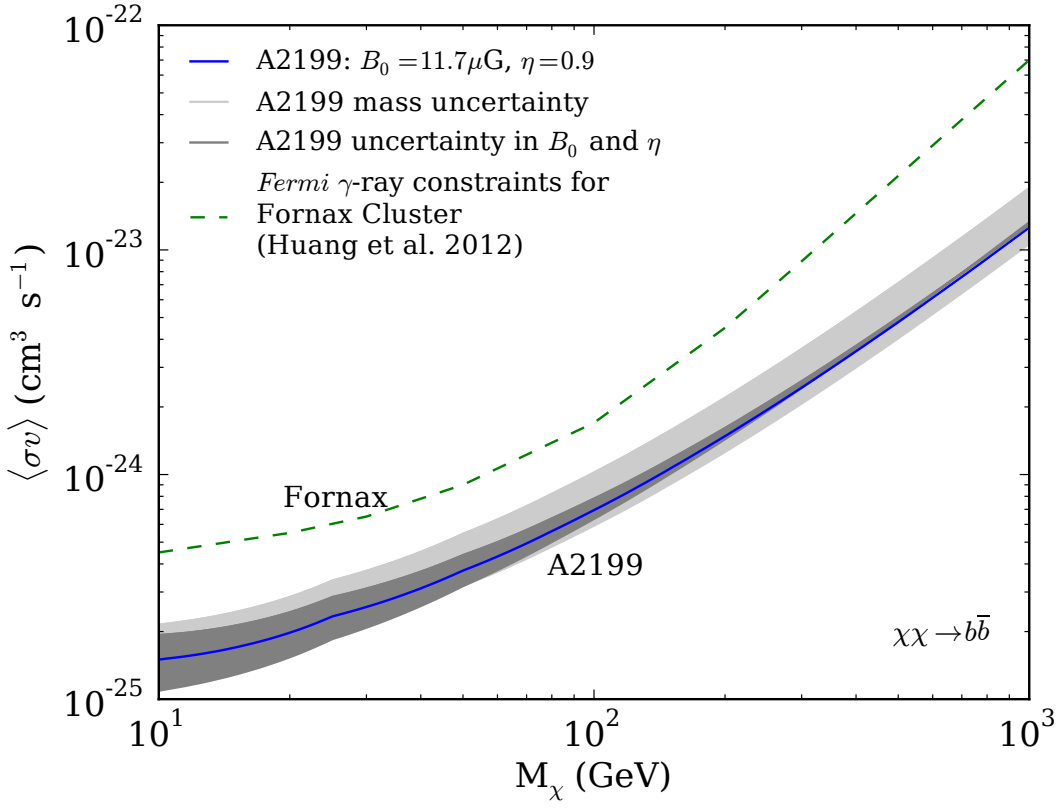

Figure 3.7: Effects of uncertainty in cluster mass and magnetic field parameters, for A2199, for the final state $b\bar{b}$, with an NFW dark matter profile. The constraints from the Fornax Cluster using gamma ray upper limits from *Fermi* are copied from Fig. 4 of Huang et al. (2012) and also correspond to an NFW profile for final state $b\bar{b}$ (same as in Figure 3.6.

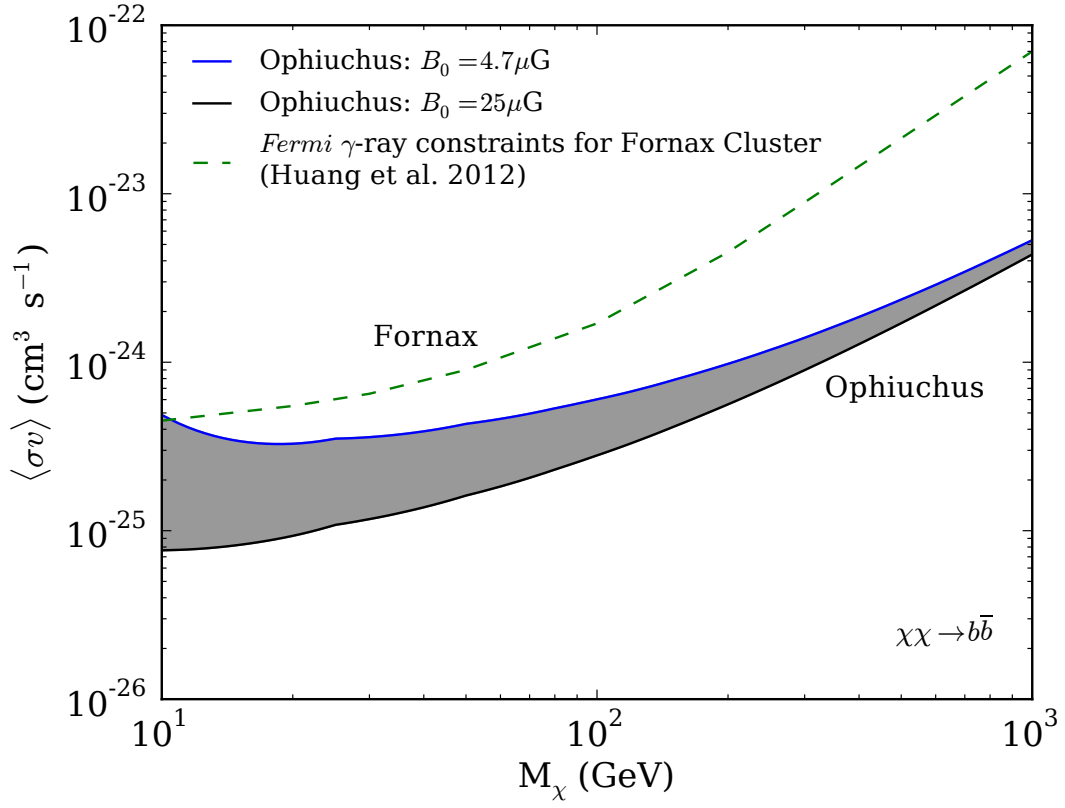

Figure 3.8: Effects of uncertainty in the central magnetic field strength for Ophiuchus, for one annihilation channel ($b\bar{b}$), with an NFW dark matter profile. The constraints from the Fornax Cluster using gamma ray upper limits from *Fermi* are copied from Fig. 4 of Huang et al. (2012) and also correspond to an NFW profile for final state $b\bar{b}$ (same as in Fig. 3.7).

Chapter 4

A Radio and X-ray Study of the Merging Cluster A2319

Note: This chapter is adapted the following published work: Storm, E., Jeltema, T. E., and Rudnick, L., "A Radio and X-ray Study of the Merging Cluster A2319", 2015, MNRAS, 448, 2495.

4.1 Introduction

Galaxy cluster mergers are among the most energetic events in the universe, dissipating as much as 10^{63} ergs primarily into the intracluster gas. Signatures of cluster mergers can be observed in the X-ray emitting ICM. Shocks are one indicator of a dynamically disturbed ICM. Cold fronts, characterized by a surface brightness discontinuity in the X-ray, occur when a cold subcluster core moves through hotter ambient gas or result from sloshing of the central cool gas in the aftermath of a merger (Markevitch & Vikhlinin 2007). The temperature structures of merging clusters tend to be complex, with colder gas tracing the paths of the subcluster cores and heated gas perpendicular to the merger axes (Govoni et al. 2004).

There exists a strong correlation between the existence of radio halos and the dynamical state of clusters derived from X-ray observations (e.g. Cassano et al.

2013 and references therein). Radio halos are clearly associated with merging clusters, while more relaxed clusters do not host radio halos (e.g., Cassano et al. 2010), with few exceptions (Bonafede et al. 2014). Radio halos are therefore intimately tied to the dynamical history of clusters, and the origins of radio halos can be effectively probed by studying cluster dynamics, especially with X-ray observations.

The origin of the cosmic rays responsible for radio halos is still under debate (see Brunetti & Jones 2014 for a review of cosmic ray acceleration mechanisms in clusters). In the hadronic model, cosmic-ray protons, accelerated by merger-driven shocks and turbulence, fill the volume of the cluster (Volk et al. 1996; Berezinsky et al. 1997). These cosmic-ray protons collide with thermal particles in the ICM, producing pions that decay to electrons and positrons, which then lose energy *in situ*, via synchrotron radiation if the magnetic fields are sufficiently strong (Dennison 1980; Blasi & Colafrancesco 1999). The hadronic model provides a natural explanation for the diffuse nature of radio halos and for the strong observed correlation between X-ray and radio emission in clusters, since both trace the gas density in this scenario. However, among the products of cosmic-ray proton collisions are gamma rays, and clusters have not yet been detected in the gamma-ray band (most recently, Ackermann et al. 2014).

In the reacceleration model, a long-lived mildly relativistic population of seed electrons are reaccelerated to energies sufficient to produce observable synchrotron emission by merger-driven turbulence throughout the cluster (Brunetti et al. 2001, 2004; Brunetti & Lazarian 2011a; Petrosian 2001; Donnert et al. 2013). In this context, the predicted gamma-ray emission from Inverse Compton (IC) scattering is low compared to observed upper limits (e.g., Brunetti & Lazarian 2011a; Brunetti et al. 2012). However, the properties of turbulence in the ICM are poorly understood, which limits the predictive capabilities of this model.

In this chapter we study A2319, a massive, merging, nearby galaxy cluster ($z = 0.0557$; Struble & Rood 1999). Optical observations reveal two subclusters, the more massive A2319A and a smaller subcluster to the northwest, A2319B, separated by $\sim$ 10 arcmin in the plane of the sky and by $\sim$ 3000 km s^{-1} in

velocity space (Faber & Dressler 1977; Oegerle et al. 1995). A mass ratio of 3:1 is derived for the A and B subclusters in Oegerle et al. (1995).

A2319 hosts a previously detected $\sim$ 10 arcmin (650 kpc) radio halo that closely traces the X-ray emission from the ICM (Harris & Miley 1978; Feretti et al. 1997). However, recent observations with the Green Bank Telescope (GBT) reveal the true extent of the halo to be $\sim$ 35 arcmin ($\sim$ 2 Mpc) across (Farnsworth et al. 2013).

A2319 has been studied extensively in the X-ray by several instruments, including *ASCA* (Markevitch 1996), *ROSAT* (Feretti et al. 1997), *BeppoSAX* (Molendi et al. 1999), *Chandra* (Govoni et al. 2004; O'Hara et al. 2004), *Suzaku* (Sugawara et al. 2009), and *XMM-Newton* (Ghizzardi et al. 2010; this work). The X-ray emission also reveals several signatures of merger activity, including a complex temperature structure and a cold front to the SE of the central X-ray core of A2319A (Govoni et al. 2004; O'Hara et al. 2004; Ghizzardi et al. 2010). While an optical analysis by Oegerle et al. (1995) claims that there is a non-negligible chance the subclusters are not actually gravitationally bound, a photometric study of the galaxies in A2319 combined with the detection of a cold front in the X-ray is clear evidence that the cluster is post-merger viewed in projection ($\sim 30^\circ - 70^\circ$ to the plane of the sky; O'Hara et al. 2004; Yan et al. 2014).

In this chapter we present a joint analysis of radio and X-ray observations of A2319. From $\sim$ 20 cm radio observations with the upgraded Jansky Very Large Array (VLA), we report more extensive halo emission than previously seen by interferometer measurements, and identify a distinct 800 kpc core to the halo emission and an extension to the southwest (SW) that blends smoothly into the larger scale halo detected by the GBT. We present a new analysis of archival X-ray observations from *XMM-Newton* to examine potential connections between the radio and X-ray emission in this cluster. We find that the radio halo core traces the central X-ray emission remarkably well. In light of this discovery of a multicomponent halo, we revisit the dynamical history of this cluster and explore possible origin models for this radio halo.

This chapter is organized as follows. In Section 4.2, we review radio obser-

vations of A2319 from the literature and present our results from a new analysis of VLA data. In Section 4.3, we summarize previous X-ray analyses of A2319 and present a new analysis of archival *XMM-Newton* observations. In Section 4.4, we discuss the implications of the radio and X-ray observations in the context of cluster dynamics, cosmic ray origins, and magnetic field structure. We conclude in Section 4.5. We adopt a ΛCDM cosmology, where $H_0 = 70$ km s^{-1} Mpc^{-1}, $\Omega_m = 0.3$, $\Omega_\Lambda = 0.7$. At the redshift of A2319 ($z = 0.0557$), 1 arcsec corresponds to 1.08 kpc.

4.2 Radio Analysis

4.2.1 Previous Observations

The radio halo in A2319 has been observed previously with the WSRT and the VLA (Harris & Miley 1978; Feretti et al. 1997). After subtraction of discrete sources, Harris & Miley (1978) reported a $\sim 10'$ or 650 kpc halo with an integrated flux density of 1 Jy at 610 MHz using WSRT. Observations at 90 cm (330 MHz) by Feretti et al. (1997) with WSRT and VLA were badly compromised by sidelobes from Cygnus A. The best map was obtained from the WSRT observations at 20 cm (1400 MHz), which yielded a $\sim 15'$ or 1000 kpc radio halo that traced the X-ray emission as observed with *ROSAT*. The total flux of the halo reported was 153 mJy after point source subtraction, with an rms noise of 0.035 mJy beam^{-1} for a $29.0'' \times 20.4''$ beam. Feretti et al. (1997) noted that they did not capture the full size or flux from the halo due to missing short baselines. Feretti et al. (1997) also reported on a detection of the halo at 408 MHz with the Northern Cross Radio Telescope (NCRT), which yielded a total halo flux of 1.45 Jy after point source subtraction.

Observations of the halo in A2319 with the (GBT) were presented in Farnsworth et al. (2013). The detected halo flux and size were more than double the previous detection with WSRT. Farnsworth et al. (2013) reported a halo flux of 328±28 mJy and a largest angular size of $35'$ (largest linear size of 2 Mpc) at 1400 MHz, for a

$9.7' \times 9.5'$ beam. Since it is a single dish, the GBT can capture all of flux from extended, diffuse sources such as radio halos. This detection represents the total flux and extent of the halo in A2319. However, the GBT cannot map smaller scale structure in the radio halo because its resolution is poor compared to interferometers.

4.2.2 VLA Analysis

We observed A2319 with the VLA in 2010 in the C and D configurations over two 128 MHz spectral windows centered on 1348 and 1860 MHz. Two pointings were made for each configuration, centered on the subclusters A2319A and A2319B. Pointing centers were $\alpha = 19^h21^m15^s.00$, $\delta = 43°52'00''.00$ and $\alpha = 19^h20^m45^s.00$, $\delta = 44°03'00''.00$. The total time on source was ~ 4.5 hours for the C configuration and ~ 7 hours for the D configuration. The data were taken while the new correlator was still being debugged, which resulted in some problems with the analysis, as described below. Data analysis and imaging were performed with the National Radio Astronomy Observatory (NRAO) analysis package CASA[1], version 4.0.1.

Data from the C configuration were not used as we originally intended. We planned to subtract the fluxes from the point sources in the C configuration images from the D configuration images. However, after calibration and imaging, it was discovered that the fluxes in the C configuration data set were corrupted, and could not be salvaged. We were able to use the C configuration images as guides for locating point sources, in addition to the NVSS (Northern VLA Sky Survey; Condon et al. 1998).

D configuration data were calibrated with CASA. 3C286 was used as the flux calibrator and J1845+4007 was used as a bandpass and phase calibrator, which was observed every 20 minutes. This observation was made in spectral line mode (as are all new VLA observations) with a channel width of 2 MHz. This allows for more precise excision of radio frequency interference (RFI). The data were

[1] casa.nrao.edu

Hanning smoothed and RFI was excised first automatically using the `flagdata` and `flagcmd` tasks in CASA, and then the remaining RFI was carefully removed by hand. Approximately 50% of the data in each spectral window were contaminated by RFI, which is typical for L band observations. After calibration, the data sets were time-averaged to 10s from 1s to speed up image processing.

Imaging was performed using the CLEAN task in CASA. We first created maps using only *uv* data at baselines longer than 200λ, to preserve the flux of compact sources while significantly reducing the halo emission. In Table 4.1, we list the compact sources located within the 1348 MHz detected halo region. We scaled their fluxes to 1400 MHz to facilitate comparison with the NVSS, by first averaging the primary-beam-corrected fluxes from the two pointings and then interpolating between 1348 and 1860 MHz. For the sources also found in NVSS, our fluxes agree within calibration uncertainties of a few percent. We then subtracted the baseline-restricted clean components from the full *uv* data set, so that we were left with flux only from the halo plus residual noise. We then *uv* tapered to a $\sim 120''$ beam to enhance the sensitivity to extended emission. We used multiscale CLEAN to image each map. We attempted several iterations of self calibration (phase only) and widefield CLEANing; however, these techniques did not noticeably improve image quality, so our final images do not include these processing steps. We mosaicked the CLEANed images from the 2 pointings and applied the primary beam correction.

The 1860 MHz spectral window suffered from significant residual RFI which particularly created problems for the reconstruction of the diffuse emission. Therefore, in the remainder of the chapter, we will report only the results from the 1348 MHz map. The resulting image of the diffuse emission at 1348 MHz is shown in Figure 4.1.

4.2.3 The Radio Halo in A2319

The radio halo is significantly larger with a more complex morphology than previously detected in interferometer maps. The flux density within the 3σ con-

tours at 1348 MHz is 240 ± 10 mJy, with an rms noise of 0.4 mJy beam^{-1}. This is significantly less than detected on the GBT by Farnsworth et al. (2013) because of insufficient short *uv* spacing data with the VLA. The reported uncertainty in the integrated flux density does not take into account any uncertainties in calibration or imaging. The halo's longest dimension as detected by the VLA at 1348 MHz is $22'$ or 1400 kpc, compared to about $35'$ or 2000 kpc for the GBT.

Halo Structure

Figure 4.2 shows the various components of the halo. The full GBT emission spans 2 Mpc and is shown as a single contour here. The residual GBT emission, after subtracting out the VLA image convolved with the GBT beam, is visible on three sides of the core. On the fourth side, to the SW, the VLA recovers all the flux seen at the GBT.

This large SW extension was previously undetected by interferometers. With a flux density of 62 mJy over an area of $\sim 3.6 \times 10^5$ arcsec^2 (about a third of the total area of the halo), it contributes only 25% of the halo flux visible to the VLA. The SW extension appears to have no X-ray counterpart, as discussed in Section 4.3.

In this work, we were able to increase the surface brightness sensitivity by convolving down to $120''$ resolution after compact source removal. Previous interferometer images were able to detect the brighter regions of diffuse emission, but were not able to pick out the various sub-structures because of confusion from compact radio emission (Feretti et al. 1997). A hint of the core of the halo may be visible in the Feretti et al. (1997) 90 cm map, but is likely confused with nearby compact emission (source K, Table 4.1).

Spectral Analysis

Due to the limited quality of the 1860 MHz map we were unable to calculate a reliable spectral index for the halo core. Feretti et al. (1997) calculate spectral indices using fluxes from the NCRT at 408 MHz and WSRT at 610 and 1400 MHz.

They report a steepening spectrum with frequency: $\alpha_{610}^{408} = 0.92$ and $\alpha_{1400}^{610} = 2.2$. Using our new flux from the VLA of 240 mJy at 1348 MHz, the spectral index is reduced to $\alpha_{1348}^{610} = 1.8$. However, the discovery of a significantly larger emitting region with GBT from Farnsworth et al. (2013) indicates that these interferometric observations are missing a substantial amount of flux (328 mJy from the GBT versus 153 mJy from the WSRT (Feretti et al. 1997) at 1400 MHz), so this steepening must be viewed as tentative.

4.3 X-ray Analysis

A2319 has been observed by several X-ray telescopes, including *ASCA* (Markevitch 1996), *ROSAT* (Feretti et al. 1997), *BeppoSAX* (Molendi et al. 1999), *Chandra* (Govoni et al. 2004; O'Hara et al. 2004), *Suzaku* (Sugawara et al. 2009), and *XMM-Newton* (this work). All instruments reveal an asymmetric X-ray distribution, with the brightest emission located near the center of the A2319A main cluster, and a tail extending to the NW towards the A2319B subcluster. It is a relatively hot cluster, with a mean X-ray temperature between 9-12 keV, depending on the instrument. Observations from *ASCA*, *ROSAT*, and *BeppoSAX* revealed temperature decreases to the NW of the emission peak, suggesting that this cooler temperature is associated with the ICM of A2319B. There is no evidence for nonthermal X-ray emission from observations with *BeppoSAX* (Molendi et al. 1999), *Suzaku* (Sugawara et al. 2009), or *Swift* (Ajello et al. 2009).

Temperature maps of A2319 from *Chandra* observations show evidence of cooler regions in the cores of the merging subclusters, and hotter regions perpendicular to the merger axis, consistent with other observations of merging clusters (Govoni et al. 2004; O'Hara et al. 2004). Govoni et al. (2004) find for a sample of clusters with radio halos that in general the radio halo tends to trace the hotter X-ray regions. However, these temperature maps are only sensitive to the central, brightest region of the cluster, so it is difficult to characterize the relationship between the large-scale halo and the X-ray temperature.

A detailed study of the merger history of A2319 using *Chandra* observations is

found in O'Hara et al. (2004). There is a clear discontinuity seen in the *Chandra* X-ray image $\sim 3'$ to the SE of the brightness peak, which is identified as a cold front. The peak X-ray emission is offset from the central cD galaxy. O'Hara et al. (2004) also find evidence for dimmer emission in the region of A2319B. The authors propose a scenario in which A2319 is post merger, and the two subcluster cores are moving apart. In this scenario, A2319B moved past the main core with a nonzero impact parameter and was stripped of most of its gas, while the core of A2319A was displaced from its pre-merger position. The interaction between the cold core of A2319A and the surrounding warmer ICM is responsible for the formation of the cold front. They argue that these X-ray features, along with information on velocity dispersion from optical analyses, point to a NW-SE merger axis that is $\sim 65°$ out of the plane of the sky. If this merger is taking place at this large angle to the plane of the sky, then quantitative analyses of this cluster become difficult due to projection effects.

4.3.1 *XMM-Newton* Analysis

Data Reduction

We analyzed the three archival *XMM* observations of A2319 (ObsIDs: 0302150101, 0302150201, 0600040101), using data from the MOS1, MOS2 and PN cameras on the EPIC instrument. We utilized the XMM Extended Source Analysis Software (XMM-ESAS; Kuntz & Snowden 2008; Snowden et al. 2008), in conjunction with the XMM Scientific Analysis System (SAS) version 13.5.0, for data preparation and background modeling. We filtered the data for soft proton flares, masked point sources, and generated quiescent particle background images following the standard ESAS analysis. After filtering, the total exposures for each camera, summed over the three observations, were $\sim$ 80 ks each for MOS1 and MOS2, and $\sim$ 72 ks for PN. We created an exposure-corrected, background-subtracted, mosaicked image, binned to $3''$ per pixel, in the soft (0.5-2 keV) X-ray band.

Image and Residuals

We present an image of the X-ray emission from A2319 in Figure 4.3. We clearly observe a surface brightness discontinuity to the SE that is consistent with the previously detected cold front (Govoni et al. 2004; O'Hara et al. 2004; Ghizzardi et al. 2010). A visual inspection of Figure 4.3 suggests two components to the X-ray emission: a bright core corresponding to the subcluster A2319A, bounded on the SE side by the cold front and extending to the NW in the direction of the subcluster A2319B, and a more symmetric, fainter emission region outside the cold front. There is no obvious sign of excess X-ray emission in the region where the SW extension to the radio halo is found. Our results are consistent with the previous *Chandra* observation.

Motivated by two-component structure evident in the X-ray emission, we simultaneously fit two smooth, elliptical beta models to the X-ray emission to examine the the residuals (Cavaliere & Fusco-Femiano 1976; Sarazin 1986). The first beta model is fit to the core region (bounded on the SE by the cold front) and the second is fit to the more symmetric extended emission region:

$$S_{core}(r_\perp) = S_1 \left(1 + \left(\frac{r_\perp}{r_{c1}}\right)^2\right)^{-3\beta_1+0.5} \tag{4.1}$$

$$S_{ext}(r_\perp) = S_2 \left(1 + \left(\frac{r_\perp}{r_{c2}}\right)^2\right)^{-3\beta_2+0.5} + S_b \tag{4.2}$$

where S_1 and S_2 are the peak amplitudes in X-ray brightness (in counts s^{-1} deg^{-2}) of each component of the double beta model, r_{c1} and r_{c2} are the two core radii, $r_\perp$ is the projected distance from the peak, and S_b is a constant background term. The two beta model fits have slightly different centers.

We binned the X-ray image to 12″ per pixel and fit the data using the package *Sherpa*. The reduced chi-squared for our best fit is 2.3 for 17178 degrees of freedom.The best fit values for the core radii r_{c1} and r_{c2} are 128 kpc and 394 ± 9 kpc, respectively. The value for r_{c1} is at its maximum bound, corresponding to the distance from the X-ray peak to the cold front. Relaxing this bound leads to a best fit value for the radius of the inner beta model equal to that of the outer beta

model. While the global fit is slightly preferred in this instance, the larger residuals left in the core indicate that this is not a good fit to the central region of the cluster. Best-fit values for β_1 and β_2 are 0.644 ± 0.005 and 0.77 ± 0.02, respectively. While not expressed explicitly in Equations 1 and 2, both fits have moderately small eccentricities. The best fit background value is 9.4 ± 0.2 counts s^{-1} deg^{-2}. We quote 1σ statistical uncertainties on best-fit values, but stress that the surface brightness of this cluster is not expected to be well-modeled by any smooth β-model, given the asymmetry in the X-ray emission due to the cluster merger.

In Figure 4.4, we see clear evidence of a surface brightness discontinuity to the SE, corresponding to the previously detected cold front. The spiral pattern of positive residuals seen in Figure 4.4 is commonly found in simulations of cluster mergers with nonzero impact parameters, which leaves the more massive core intact and triggers sloshing that produces the cold front (Ricker & Sarazin 2001; Ascasibar & Markevitch 2006; Roediger et al. 2012; Laganá et al. 2010). This interpretation is consistent with the merger picture put forth by O'Hara et al. (2004). We do not find any evidence in the residuals for excess emission in the SW region after subtraction of the best-fit smooth beta models. The same analysis of the $2 - 10$ keV band image yields similar results to the $0.5 - 2$ keV band.

4.4 Discussion

4.4.1 Radio Halo Substructure and the X-ray Cold Front

In the bright, central region of the cluster, the radio emission traces the X-ray emission remarkably well. The radio brightness at 1348 MHz falls off rapidly across the cold front, especially visible towards the eastern edge.

In order to examine the profiles of the X-ray and radio emission across the cold front region, we calculated the average brightness in a 90 degree wedge oriented east-west, and plotted it in Figure 4.5. Note the distinct change in slope of the X-ray profile across the cold front, steep in the interior (left) and shallower beyond the cold front (right). The same is true for the radio emission, although the

transition is significantly broadened because of the 120″ beam.

4.4.2 A Multicomponent Radio Halo

The brightness profiles of the core X-ray and VLA radio emission (see Figure 4.5), together with the substantially larger radio emission detected by the GBT (Figure 4.2), provide evidence for a cluster with distinct emission regions that are perhaps produced by different underlying emission processes. The X-ray emission together with temperature maps from Govoni et al. (2004) and O'Hara et al. (2004), show a distinct, cold X-ray core that has been disturbed by a significant merging event and has compressed some of the ICM near it, producing a cold front. The merger likely occurred with a nonzero impact parameter and at a significant angle to the plane of the sky. There is additionally a fainter, larger component to the X-ray emission that maps the hotter, more diffuse gas of the ICM; this is possibly gas that was undisturbed by the merger event or has since relaxed.

The radio emission also contains multiple components. There is a large-scale, 2000 kpc component detected with the GBT. Some of this large-scale emission is also seen with the VLA in the SW extension. A smaller, $\sim$ 800 kpc brighter region of radio emission is embedded in the larger halo. This radio core closely traces the X-ray emission, and the brightness of this region falls off sharply in the same location as the X-ray cold front.

It is perhaps natural to speculate on the (potentially different) origins for these two components of the radio halo. Cluster mergers drive shocks and turbulence throughout the ICM, providing acceleration sites for the cosmic rays responsible for radio halos (e.g., Brunetti & Jones 2014). The large-scale halo component may be the result of this usual story: merger-generated cosmic ray acceleration that permeates the entire cluster volume. In the hadronic model, long-lived cosmic-ray protons continuously resupply the radiating cosmic-ray electrons. The lack of excess X-ray emission in the SW region of the halo implies the lack of thermal electrons, and therefore the lack of sufficient cosmic-ray proton collision targets.

The fact that we observe radio emission in this region already suggests that a hadronic origin in this region is disfavored (see Section 4.4.4). Cosmic-ray proton collisions produce gamma rays in the hadronic model, so limits on the gamma-ray emission from A2319 with *Fermi* could provide even stronger constraints on this model. However, current gamma-ray limits from this cluster and others already put tension on a hadronic origin for the cosmic rays for μG magnetic fields (e.g., Jeltema & Profumo 2011; Brunetti et al. 2012; Ackermann et al. 2014). The alternative for the larger scale component of the halo is that cluster-wide turbulent reacceleration of pre-existing cosmic-ray electrons is responsible.

The origins of the smaller radio core, by contrast, may be tied closely to the dynamics of the remaining subcluster core and the X-ray cold front. Simulations of minor mergers (with subcluster mass ratios of approximately 10:1) show that the turbulence generated by core sloshing is confined to the regions inside cold fronts and this turbulence may be responsible for observed radio mini-halos (ZuHone et al. 2013). Observations of the cool-core cluster RX J1720.1 + 2638 reveal that its mini-halo is bounded by X-ray cold fronts and may be the result of electrons accelerated by core-sloshing-induced turbulence (Giacintucci et al. 2014a). These mini-halos are typically <300 kpc across and are found in a handful of cool-core clusters (e.g., Feretti et al. 2012; Gitti et al. 2012). They are often accompanied by a bright central radio galaxy (e.g., Blanton et al. 2001; Doria et al. 2012).

A2319, by contrast, does not have a cool core; its central entropy of $\mathbf{K}_0$= 270 keV-cm^2 (Cavagnolo et al. 2009) and subcluster mass ratio of 3 : 1 (Oegerle et al. 1995) puts it firmly in the recent merger class. Nor does it have a bright central radio galaxy. However, the striking similarity between the morphologies of the X-ray and radio emission in A2319's core suggest that the origins of the radio core may be more similar to the origins of mini-halos.

4.4.3 Core Magnetic Field

Magnetic fields in clusters are essential for discriminating between origin models for radio emission, especially with limited concrete spectral information, but

are poorly understood (e.g., Feretti et al. 2012). We can calculate the volume-averaged magnetic field, B_{eq}, from equipartition, by assuming the cosmic ray energy density (protons and electrons) is equal to the magnetic field energy density. We use the revised equipartition formula for B_{eq} derived in Beck & Krause (2005), with the cosmic-ray proton to electron number ratio, $k = 100$, appropriate for acceleration by either direct, turbulent or secondary, hadronic, processes. This equation does not rely on a choice of integration bounds in frequency space, which, in the classical equipartition calculation, induces an implicit dependence on the magnetic field.

To calculate the equipartition field, we consider the bright central core of the cluster, limiting the region to that enclosed by the 12σ contour on the 1348 MHz radio emission, which also corresponds to the X-ray core (that is, the region inside the cold front). For the line of sight depth of the region, we use $l \sim 500$ kpc, which is approximately the width of the region enclosed by the 12σ contour. With a brightness of 0.5μJy arcsec^{-2} and a spectral index $\alpha = 1.8$, we derive $B_{eq} = 2.8$ μG. For $\alpha = 0.92$, this decreases to 1.7 μG. These values are consistent with those estimated from Faraday Rotation measures for disturbed clusters (e.g., Govoni & Feretti 2004).

4.4.4 Comparing the X-ray and Radio: A Test for Hadronic Origins

A spatial comparison of the X-ray and radio emission can help to discriminate between different acceleration models for cosmic rays and probe the structure of magnetic fields in clusters.

The X-ray emissivity due to thermal bremsstrahlung radiation, the dominant continuum emission mechanism, depends on the thermal ICM density, n_{th} and the X-ray temperature, T_X:

$$\epsilon_X \propto n_{th}^2 T_X^{1/2} \tag{4.3}$$

The temperature in A2319 only changes by a factor of $\lesssim 2$ across the cluster (Govoni et al. 2004; O'Hara et al. 2004); we can therefore safely ignore the weak

dependence on temperature.

The radio emissivity depends on how the cosmic-ray electrons responsible for the synchrotron emission are generated. In the case of hadronic origins, assuming a power law distribution for the cosmic-ray protons, the synchrotron emissivity depends on the cosmic-ray proton density, the thermal ICM density and the magnetic field (e.g., Brunetti et al. 2012):

$$\epsilon_\nu \propto \nu^{-\alpha} n_{th} n_{CRp} \frac{B^{1+\alpha}}{B^2 + B_{CMB}^2} \tag{4.4}$$

where α is the radio spectral index ($S_\nu \propto \nu^{-\alpha}$). Note this expression includes electron injection losses due to synchrotron and Inverse Compton scattering. B_{CMB} is the magnetic field equivalent of the Cosmic Microwave Background energy density, and is equal to 3.25μG at $z = 0$. If we assume the cosmic-ray proton density n_{CRp} roughly scales with the thermal density n_{th}, then the radio emissivity scales with the X-ray emissivity convolved with the magnetic field dependence.

To make a quantitative comparison between the radio and X-ray images, we convolved and regridded the X-ray image to match the resolution ($9'.7 \times 9'.5$ beam) and pixel size ($120''$) of the GBT. The result of dividing the radio image by the X-ray image, each normalized to a peak of 1, is shown in Figure 4.6. In the context of a hadronic origin model for the cosmic rays, this yields a spatial map of the magnetic field with an overall scaling dependent on the spectral index:

$$\frac{\epsilon_\nu}{\epsilon_X} \sim \frac{B^{1+\alpha}}{B^2 + B_{CMB}^2} \tag{4.5}$$

The ratio between the radio and the X-ray is approximately constant in the central X-ray emitting region. Towards the SW, this ratio grows by a factor of ~ 3. There is also an excess towards the NE over a smaller area. The same analysis performed with the $2 - 10$ keV X-ray image yields a similar map, with a pronounced excess towards the SW and smaller excess towards the NE. However, the brightness ratio is reduced far from the center (~ 2.4 in the SW region) compared to the $0.5-2$ keV image, due to the smaller signal-to-noise of the $2 - 10$ keV image. Assuming hadronic origins for the cosmic rays, this would imply that the magnetic field profile is relatively flat over the central region of the cluster, but increases towards

the SW and NE, perpendicular to the merger axis. In the case of direct (re-) acceleration by ICM turbulence, the enhanced radio emission would be explained by either increased turbulence or an excess of seed cosmic-ray electrons in these regions.

There is evidence from simulations and Faraday Rotation measurements of galaxies in clusters that the magnetic field profile should decrease with increasing radius, and roughly follow the thermal electron density (Dolag et al. 2001; Govoni & Feretti 2004; Bonafede et al. 2010; Donnert et al. 2013). The magnetic field profile inferred from Figure 4.6 is clearly asymmetric, and contradicts this evidence. Alternatively, if the magnetic field is not larger in this SW extension, then the cosmic-ray proton density must increase. This is also unlikely, as the cosmic-ray proton density is typically assumed to also follow the thermal gas density (e.g., Pinzke & Pfrommer 2010). We therefore argue that a hadronic origin model for the cosmic rays in A2319 is disfavored. At the same time, the turbulent re-acceleration model could be consistent with the data, but there is no way currently to tell whether the requisite enhanced turbulence or seed relativistic electrons are present. Detailed spectral index maps of the radio halo would help to clarify this scenario.

4.5 Conclusions

In this chapter, we present results from observations of the merging cluster A2319 with the VLA at 1348 MHz and *XMM* in the $0.5 - 2$ keV band. We tentatively report on the discovery of the multicomponent nature of the radio halo in A2319: (1) a large-scale, 2 Mpc, component discovered by Farnsworth et al. (2013) with the GBT and partially detected with our VLA observations at 1348 MHz, and (2) a smaller, 800 kpc radio core that is bounded on one side by a cold front observed in the X-ray. A detailed spectral index map for A2319 would help to further distinguish the smaller radio core from the larger emission region. In the X-ray, we confirm the previous detections of the X-ray cold front to the SE and provide strong evidence for core sloshing in the form of a spiral-like

structure in the residual X-ray emission after subtraction of a smooth, symmetric component. We also show via a simple spatial comparison of the X-ray and radio emission that a hadronic interpretation for the radio emission, at least outside the X-ray core, is disfavored, due to the lack of excess X-ray emitting gas (and therefore targets for cosmic-ray proton collisions) in that region.

We speculate that these two radio components may have different origins. The large-scale component may be the result of merger-driven turbulence that fills the cluster volume, thus providing acceleration sites for cosmic rays (protons or electrons). The presence of the smaller radio core appears to be related to the motion of the subcluster A2319A core, and could be the result of turbulence related to this core motion that is confined to the cluster core. We propose a scenario in which A2319 recently experienced a significant merger with a nonzero impact parameter that left the more massive cluster core somewhat intact but caused it to slosh around in its gravitational potential well, resulting in a cold front observable in the X-ray and a two-component radio halo. This scenario is consistent with other X-ray studies of this cluster (O'Hara et al. 2004; Govoni et al. 2004).

A multicomponent radio halo is not entirely unprecedented. The cluster A2142, which hosts multiple cold fronts and previously detected radio emission in the cluster center classified as a mini-halo, is now known to also host a giant, ~ 2 Mpc radio halo (Farnsworth et al. 2013) and a fourth cold front ~ 1 Mpc from the cluster center (Rossetti et al. 2013). These new discoveries challenge the prevailing paradigm that cleanly separates merging systems with disturbed X-ray emission and giant radio halos from relaxed systems, with cool cores, regular X-ray emission, and mini-halos. The recent discovery of a giant, ~ 1.1 Mpc radio halo in the cool-core cluster CL1821+643 (Bonafede et al. 2014) further suggests that our current understanding of how mergers and the resulting cluster dynamics impact the production of radio emission needs revision. We add A2319 to this new ambiguous class of clusters that are perhaps in various intermediate stages between relaxed and disturbed systems, leading to novel radio and X-ray morphologies.

This study of A2319 highlights the need to combine different wavelengths of the same object in order to fully understand the interactions between the thermal and nonthermal components of clusters. In light of this work, we plan a future study that expands on our current analysis of A2319 to include more information on the thermal component with SZ data and the nonthermal component with gamma-ray upper limits.

Table 4.1: Radio Source Properties

	NVSS ID	RA (J2000)	Dec (J2000)	VLA (1400 MHz, mJy)	F97	HM78
1	192004+440034	290.01775	+44.00958	4.0	...	252
2	192012+435955	290.05067	+43.99875	1.6	...	257
3	192015+440305	290.06508	+44.05153	87	B	259
4	192017+434851	290.07446	+43.81422	3.9	C	262
5	192053+435232	290.22371	+43.87572	33	...	270
6	192109+435307	290.28854	+43.88544	25	K	273
7	192112+435640	290.30217	+43.94469	27	...	277
8	192118+435817	290.32808	+43.97156	3.5	...	278
9	192132+435946	290.38425	+43.99633	4.0	N	282
10	192133+435805	290.38858	+43.96819	110	...	283
11	192142+435749	290.42833	+43.96375	13	R	291
12	...	290.408	+43.9124	2.5	...	287
13	...	290.273	+44.0798	2.5	H	272
14	...	290.134	+43.9142	2.2	...	266
15	...	290.134	+43.8942	2.0	...	265
16	...	290.115	+43.8747	1.4	...	264

Notes. Column 1: ID number. Column 2: NVSS ID (Condon et al. 1998). Column 3 and 4: Coordinates of radio source; NVSS coordinates given if source is identified in NVSS. Column 5: Source flux measured by VLA D configuration (only baselines longer than 200λ present), scaled to 1400 MHz. Beam is 48″. Column 6: ID corresponding to the label listed in Table 4 of Feretti et al. (1997), which only lists radio sources associated with optically-identified cluster member galaxies. Column 7: ID corresponding to the serial number listed in Table 6 of Harris & Miley (1978).

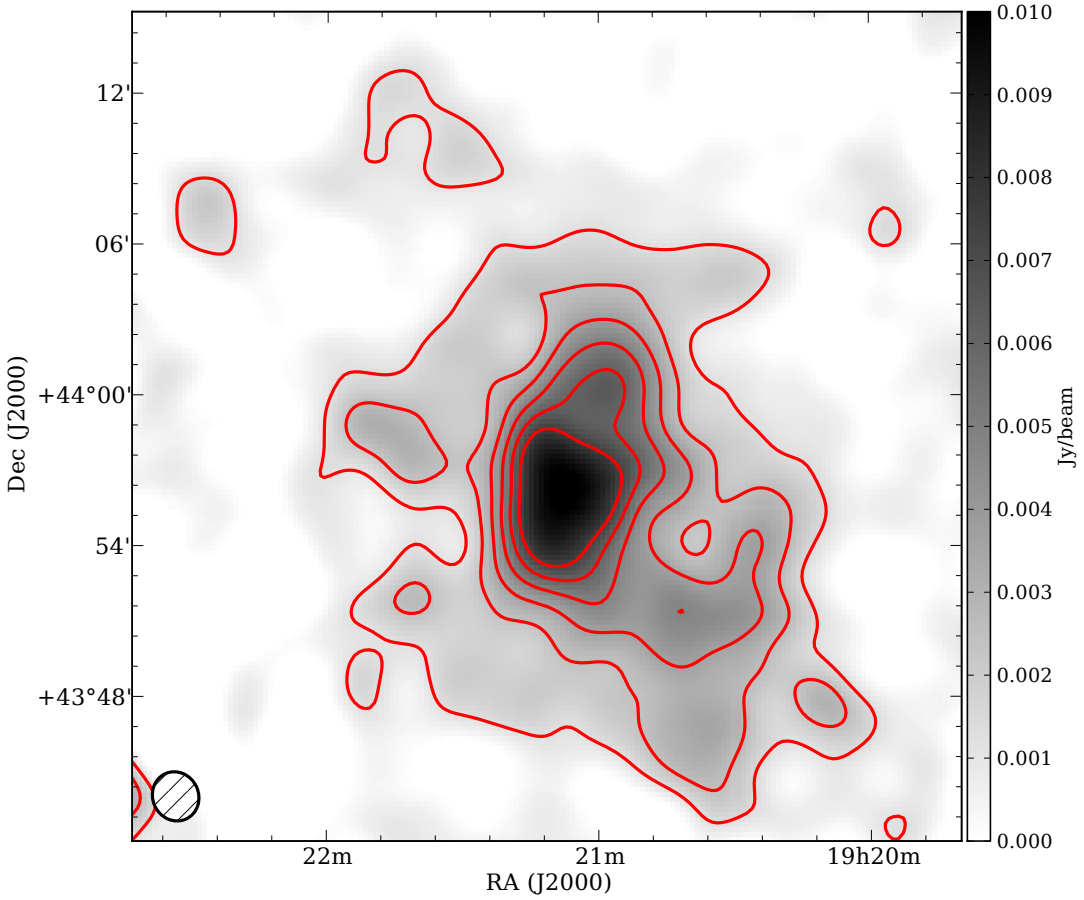

Figure 4.1: A2319 Halo at 1348 MHz from VLA. Contours in red are (3,6,9...)×0.4 mJy beam^{-1}. Beam is $119'' \times 110''$, shown in black in bottom left.

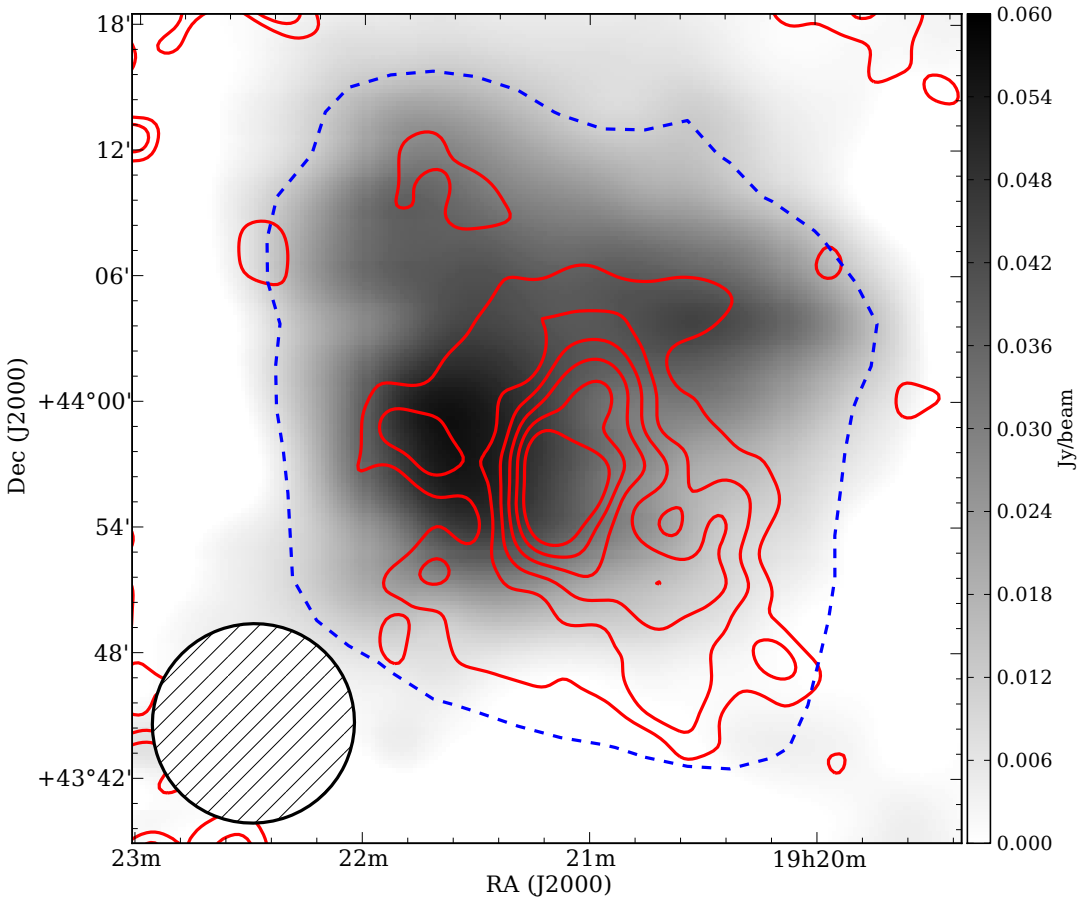

Figure 4.2: Comparison of VLA (beam: 120″) and GBT (beam: 570″) images. The VLA contours are in solid red, at (3,6,9...)×0.4 mJy beam^{-1}. The lowest contour from the full GBT image (18 mJy beam^{-1}) is shown in dashed blue. The grey scale image shows the residual GBT image after subtracting a convolved version of the VLA image. The GBT beam is shown in the bottom left.

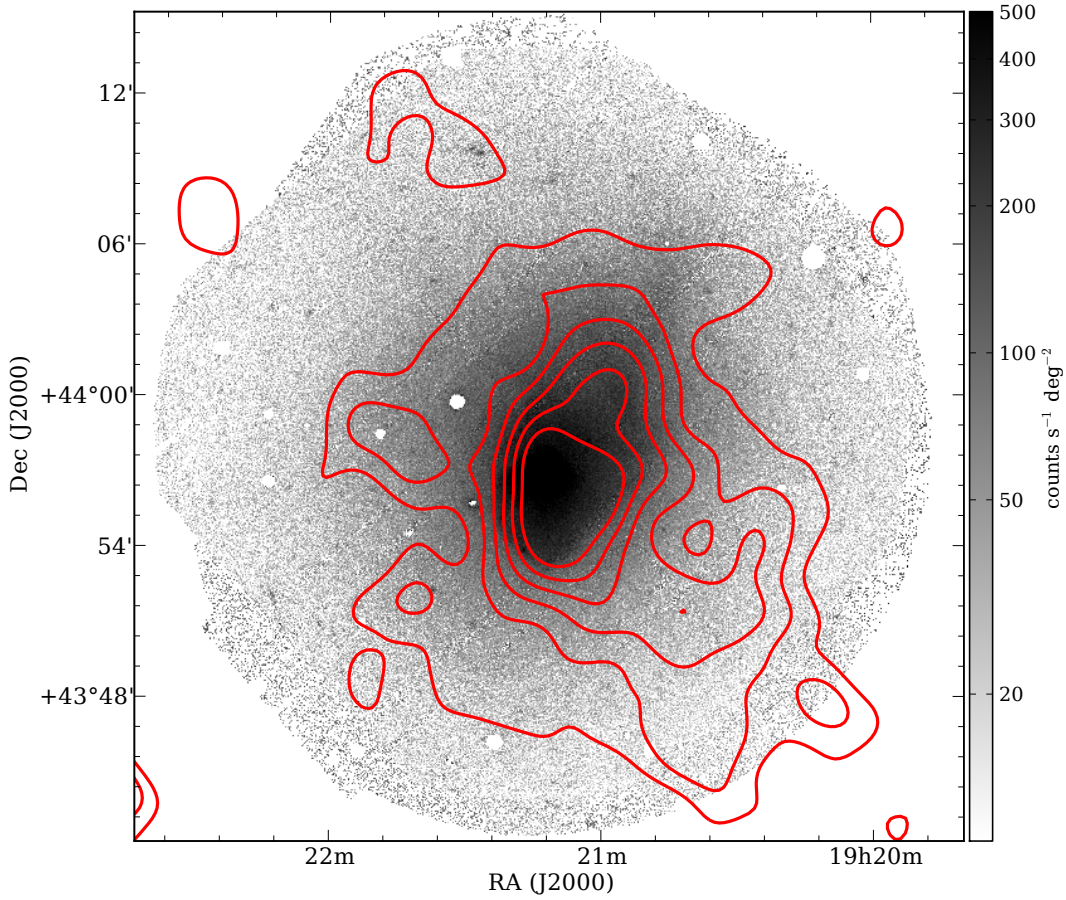

Figure 4.3: *XMM* observation of A2319, 0.5-2 keV, on a log scale. Pixels are 3″. 1348 MHz VLA radio contours are overlaid in red. Levels are (3,6,9...)×0.4 mJy beam^{-1}.

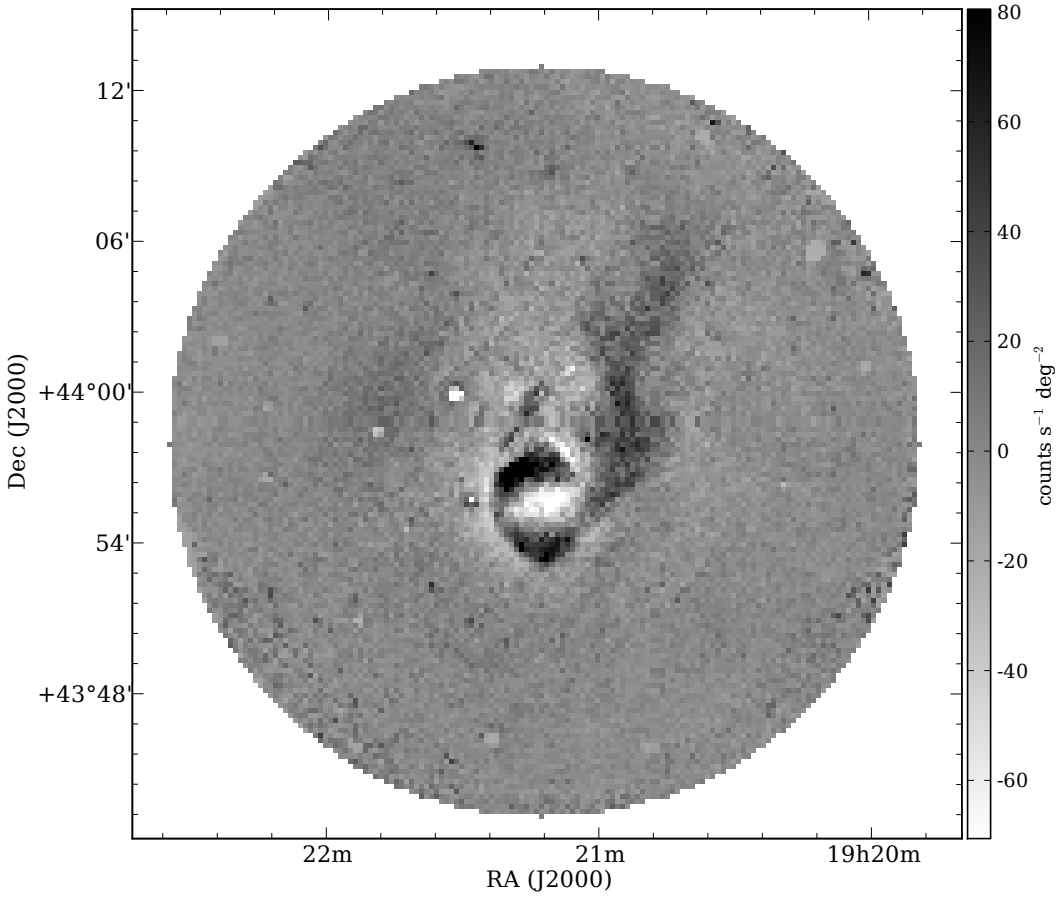

Figure 4.4: *XMM* residuals, 0.5-2 keV, after subtraction of two elliptical beta models. Pixels are 12″.

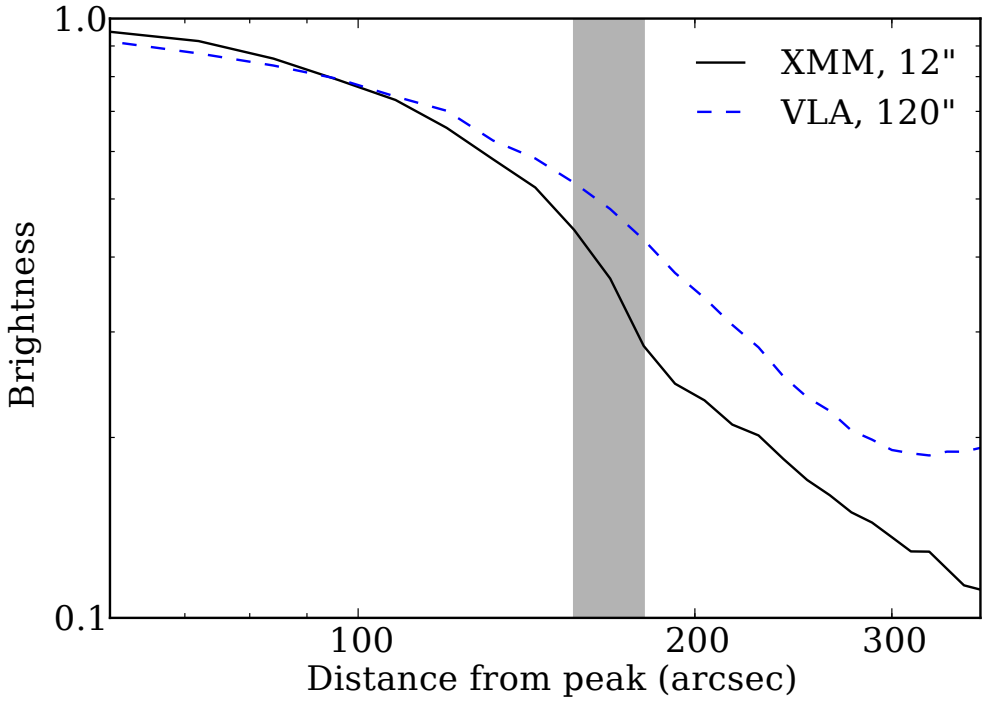

Figure 4.5: Brightness profiles for X-ray (black solid) and radio (blue dashed), in a 90° wedge centered at $\alpha = 19h21m0.56s$, $\delta = 43°56'48''$ and extending east. The X-ray image is averaged over $12''$ annuli. The radio is convolved to a $120''$ beam. The region containing the cold front is highlighted in gray. Brightness is in arbitrary units normalized to the peak.

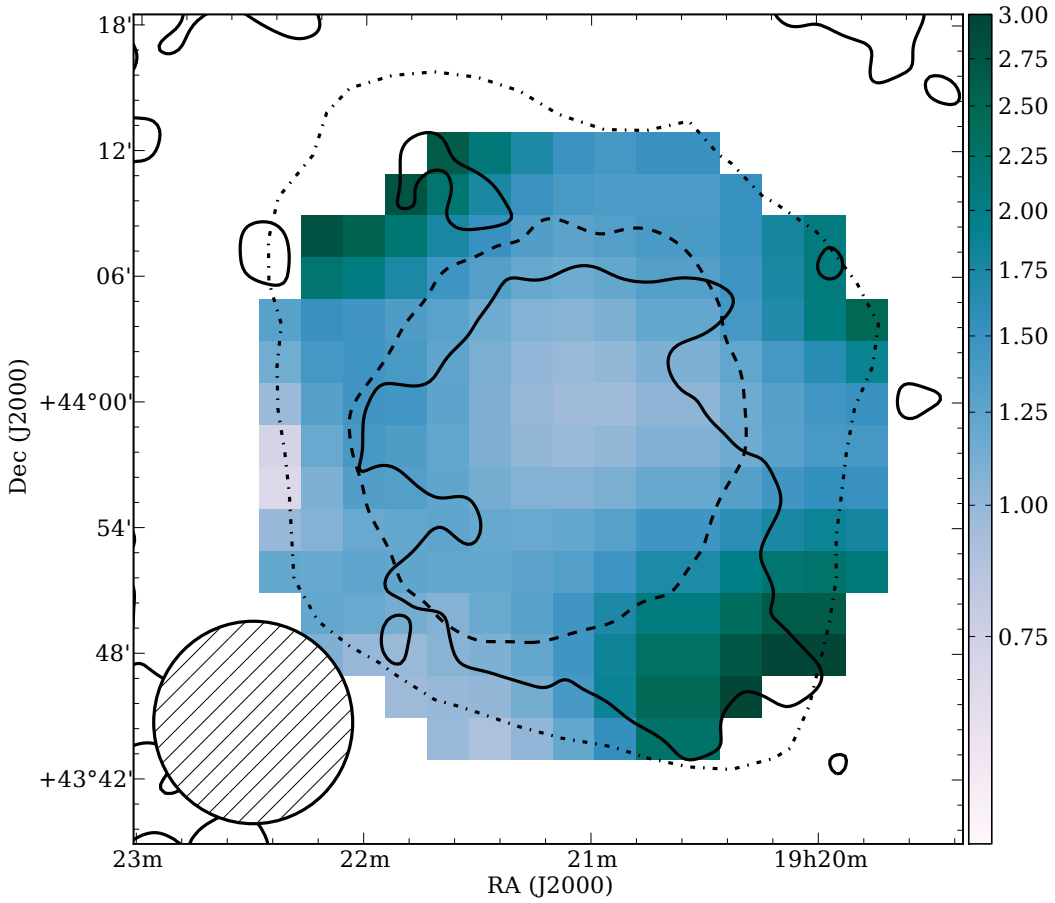

Figure 4.6: 1.4 GHz radio emission from GBT divided by $0.5 - 2$ keV X-ray emission, arbitrary units. The X-ray image was convolved and binned to the GBT resolution and grid size. Colors are on a square root scale. GBT (dot-dashed) and VLA (solid) radio 3σ contours, and X-ray contour (dashed) at 30 counts s^{-1} deg^{-2}, smoothed with a $120''$ Gaussian kernel, overlaid in black.

Chapter 5

Conclusions

5.1 Summary

The mechanisms by which relativistic particles produce nonthermal emission in astrophysical environments are well-known. Cosmic-ray electrons can synchrotron radiate in the presence of magnetic fields, observable at GHz frequencies, and can IC scatter photons to X-ray and gamma-ray energies. Cosmic-ray protons can collide with low energy particles, resulting in the production of neutral pions that decay to gamma rays and charged pions that decay to cosmic-ray electrons. However, the origins of these cosmic rays, and the mechanisms for how these cosmic rays get accelerated, are varied in galaxy clusters, and in some cases, not well-understood. I study three of these sources of nonthermal emission, namely star formation in galaxies, dark matter annihilation, and the cosmic rays in the ICM responsible for radio halos, in order to better understand and constrain the various processes that are responsible for cosmic ray production in galaxy clusters.

Galaxies are themselves reservoirs of cosmic rays that can produce emission in the radio and gamma-ray bands. In star-forming galaxies, these cosmic rays are accelerated primarily by supernovae. Thus, the rate of star formation in a galaxy, which can be traced by its infrared emission, is correlated with its nonthermal emission at both radio and gamma-ray energies. The detection of several star-forming galaxies by *Fermi* allows for the determination of a quantitative re-

lationship between the gamma-ray luminosity and the star formation rate in a galaxy (Ackermann et al. 2012b). As I show in Chapter 2, this relationship can be used to predict the gamma-ray emission from star-forming galaxies in clusters. I derive lower limits on the gamma-ray emission in clusters by summing the predicted gamma-ray emission from star formation in cluster member galaxies, and show that for some nearby clusters, these lower limits are only about an order of magnitude lower than the upper limits on diffuse emission from the ICM. As upper limits improve over time, the gamma-ray emission from star formation in galaxies will become a more dominant fraction of the total cluster emission.

Dark matter annihilation can result in the production of cosmic rays, which can then produce nonthermal emission across a wide range of energy bands in cluster environments. While the nondetection of gamma rays from clusters is typically used to constrain dark matter annihilation, an alternative way to place limits on dark matter matter annihilation is through the nondetection of radio emission from clusters. As I show in Chapter 3, the limits on the annihilation cross section for a handful of nearby galaxy clusters are comparable to or better than the limits derived from the nondetection of gamma rays, particularly for cool-core clusters which have stronger magnetic fields than non-cool-core clusters. This study shows that, despite astrophysical uncertainties, radio nondetections and marginal detections can effectively constrain dark matter annihilation in clusters, and that this method is complementary to dark matter analyses in other energy bands.

The observation of radio halos in some clusters indicates that they host a population of cosmic-ray electrons and magnetic fields that are distributed throughout the ICM. However, this nonthermal component is controlled by a cluster's thermal components, as demonstrated by the relationship between the properties of a radio halo and the merger state of a cluster. In Chapter 4, I use observations from the VLA and *XMM-Newton* to describe how the unusual, two-component morphology of the radio halo in A2319 is shaped by cluster dynamics. The faint, 2 Mpc region, observed completely with the GBT and partially recovered with the VLA, is likely the result of large-scale turbulence driven throughout the cluster volume

by the merger. The large extent and flatness of this emission, as compared to the X-ray emission, suggest that a hadronic origin for the cosmic rays responsible for the radio emission is unlikely. The bright, 800 kpc "core", however, may be more closely related to the motion of the cluster core. An off-axis merger would have disturbed the cluster core from its equilibrium position while leaving it intact. The motion of this core could result in a X-ray cold front, and could drive turbulence in this region that would accelerate cosmic rays to sufficient energies to produce the observed radio "core". This is the first such observation of a multicomponent radio halo. A detailed analysis of the radio spectral index, especially one that showed a spatial variation across the two halo components, would provide further evidence for the multicomponent structure of the halo. This study demonstrates the power for multiwavelength studies in understanding the complex interactions between a cluster's thermal and nonthermal components.

5.2 Cosmic Rays in the ICM of Clusters

Prior to the launch, and early in the mission, of *Fermi*, numerous studies predicted that gamma-ray emission from cosmic rays in galaxy clusters would be detectable in the $\gtrsim 100$ MeV energy regime (e.g., Blasi et al. 2007; Pfrommer 2008; Jeltema et al. 2009; Pinzke & Pfrommer 2010). However, diffuse gamma-ray emission from galaxy clusters has not yet been detected. The lack of a detection after five years of operation by *Fermi* (Huber et al. 2013; Ackermann et al. 2014; Griffin et al. 2014), and several years of observations by very-high-energy gamma-ray telescopes such as MAGIC (Aleksić et al. 2012), VERITAS (Arlen et al. 2012), and H.E.S.S. (Abramowski et al. 2012), has strongly constrained the potential nonthermal processes in galaxy clusters.

In particular, a scenario in which radio halos are generated by secondary electrons produced by collisions of cosmic-ray protons with intracluster gas seems increasingly unlikely. In their most recent search for gamma-ray emission from galaxy clusters, the *Fermi* LAT Collaboration constrain the dynamical importance of cosmic-ray protons in clusters. Applying a universal model for the cosmic-ray

proton content to a sample of 50 galaxy clusters, Ackermann et al. (2014) derive a maximum acceleration efficiency of cosmic-ray protons of $< 21\%$ and constrain the cosmic-ray proton pressure to $< 1.4\%$ of the thermal pressure.

I contributed to the selection of the sample of clusters used in Ackermann et al. (2014). Starting with the HIFLUGCS sample of galaxy clusters (Reiprich & Bohringer 2002), I investigated how the cumulative signal-to-noise ratio changed as a function of number of clusters. I used the predicted gamma-ray emission from cosmic rays from Jeltema et al. (2009) as my signal for this study. For the background, I used the photon counts from *Fermi*-LAT in a 10° region centered on the X-ray center of the cluster. I showed that the cumulative signal-to-noise increased monotonically as the number of clusters in the sample increased. This implied that using the largest possible sample of clusters would yield the best constraints on cosmic-ray-induced gamma-ray emission from clusters (or the best chance for detection).

Individual upper limits on gamma-ray emission are also derived in Ackermann et al. (2014) for each cluster in the sample. Depending on the cluster, these new limits are $\sim 10 - 80\%$ lower than those derived in Ackermann et al. (2010b) from 18 months of data from *Fermi*. As I show in Chapter 2, nonthermal emission from star formation in cluster galaxies will become a more meaningful gamma-ray source in clusters, as upper limits on the diffuse emission continue to improve over time.

Recent studies on diffuse radio emission from clusters also put tension on a hadronic origin for cosmic rays in clusters, and demonstrate the power of multi-wavelength observations to constrain nonthermal processes. Jeltema & Profumo (2011) assumes a hadronic origin for the radio halos in a small sample of clusters, and found that in order to produce the observed level of radio emission while also not overproducing gamma rays relative to upper limits, the magnetic fields must be comparable or higher than those inferred from Faraday rotation in those clusters. A multiwavelength study of the Coma Cluster shows that the flatness of the spatial distribution of the radio halo relative to the X-ray emission would require a cosmic-ray proton distribution that would produce more gamma-ray emission

than the current upper limits (Brunetti et al. 2012).

The bimodality observed in the distribution of clusters with and without halos suggests that radio halos may be transient phenomena (Brunetti et al. 2009). In this picture, an initially relaxed cluster will be subject to a major merger event. Turbulence driven by this merger accelerates cosmic-ray electrons to sufficient energies to produce a radio halo. As the cluster relaxes once again, turbulence dissipates and the synchrotron emission fades to levels that are too low to detect with the current generation of radio telescopes. The robust detection of diffuse radio emission from a sample of 105 stacked clusters, which individually show no radio emission, supports this "on/off" hypothesis for radio halos (Brown et al. 2011b). This scenario can also be replicated in simulations of cluster mergers, assuming a reacceleration model for the cosmic-ray electrons in the cluster (Donnert et al. 2013).

However, the recent detections of a two-component radio halo in the merging cluster A2319 described in Chapter 4, and the detection of giant radio halos from A2142 (Rossetti et al. 2013; Farnsworth et al. 2013) and CL $1821+643$ (Bonafede et al. 2014), both of which were previously characterized as relaxed clusters, indicate that the mechanisms that drive radio emission and cosmic ray acceleration in clusters are more complex than previously thought. These clusters may all be in various intermediate stages of mergers; perhaps they were off-axis events, or mergers with large subcluster mass ratios (or both). These complex merger events may drive radio emission in different ways throughout the cluster, as the energy from the merger gets distributed throughout the ICM. With its improved sensitivity, the recently upgraded VLA will likely detect more such examples of radio emission from clusters that does not fit cleanly into the prevailing merger–halo narrative. New and planned radio telescopes, described in the next section, will also likely play a key role in revealing complex radio emission from these clusters. These discoveries of complex radio emission demonstrate the importance of multiwavelength studies, and of including both single-dish and interferometric radio observations in these studies, in understanding the interplay between the thermal and nonthermal components of clusters.

5.3 Future Work

5.3.1 The Next Generation of Radio Telescopes

New and future radio telescopes are expected to provide significant clarity on the subject of the origins of radio emission in galaxy clusters. The recently-upgraded VLA has already unveiled complex radio emission in A2319 (Storm et al. 2015), and will continue to provide detailed, sensitive images of radio emission in clusters. Looking towards the future, the radio astronomy community is working towards the Square Kilometer Array (SKA), planned to start science operations in 2019 (Aharonian et al. 2013). In the interim, there are several SKA pathfinders in the GHz frequency range that are near or in early science operations, such as Apertif, which is an upgrade to WSRT (Verheijen et al. 2008), and ASKAP, the Australian Square Kilometre Array Pathfinder (Johnston et al. 2008). The Low Frequency Array (LOFAR) is a newly constructed radio interferometer that will offer views of the mostly unexplored low-frequency radio sky, with observations in the $\sim 10 - 240$ MHz range (van Haarlem et al. 2013). These instruments all list understanding the nature of diffuse radio emission in clusters as a key science goal and are expected to detect hundreds of new radio halos, increasing the number of detected halos by a factor of ~ 10 (Cassano et al. 2009, 2012).

While these new telescopes individually will provide more sensitive imaging of diffuse radio emission in clusters, significant advances will likely come from combining the data at low and high frequencies. Different origin models for radio halos predict different spectra; the spectral index of a radio halo is a key way to discriminate between models. However, very few radio halos have robust measurements of their spectra indices (Feretti et al. 2012). In particular, the "on/off" scenario predict that radio halos should have flatter spectra during the most active phases of the merger, and as the turbulence in the ICM fades, the spectral index of the radio emission will get steeper. This scenario predicts a population of ultra-steep-spectrum sources ($\alpha \gtrsim 1.5$, where $S_\nu \propto \nu^{-\alpha}$) that are not detectable at $\sim$ GHz with current instruments. However, this population of sources would be easily detectable at the low frequencies probed by LOFAR (Cassano et al.

2009). Observations with LOFAR would therefore be able to conclusively test this "on/off" hypothesis.

5.3.2 Dark Matter Constraints with New Radio Telescopes

The next generation of radio telescopes also has the potential to strongly constrain dark matter in clusters. As I show in Chapter 3, nondetections and marginal detections of diffuse radio emission from clusters can provide constraints on the annihilation of dark matter that are competitive with limits from the nondetection of gamma rays. However, nondetections or marginal detections from the more sensitive radio telescopes such as LOFAR, ASKAP and Apertif would yield substantially more constraining limits on dark matter annihilation in clusters.

The optimal sample of clusters to choose for dark matter studies in the radio is also nontrivial to determine. The signal from dark matter depends on both the physical size of the emitting region of an object, and the distance of that object, and therefore its angular size. For some fixed physical emitting size, the dark matter signal decreases with increasing redshift, as the angular size decreases. The dark matter signal also depends on the integral of the dark matter density squared, which falls off as a function of radius. Integrating to larger radii adds only a marginal amount of signal. However, this is largely unimportant for dark matter studies with *Fermi*-LAT, because diffuse emission from clusters is not resolved (except for very large and nearby sources, such as the Virgo Cluster). Thus, in order to maximize the potential dark matter signal, gamma-ray searches for dark matter are typically limited to nearby sources ($z \lesssim 0.1$). The sample of clusters for analysis in Chapter 3 was also limited to this redshift cut, as a primary goal of that work was to compare the annihilation limits from radio directly with those from gamma rays, for some of the same objects.

However, radio interferometers have sufficient resolution to spatially resolve diffuse emission from clusters. A complication to this is that the sensitivity of radio interferometers depends on the angular size of the emission region, and therefore is worse at very low redshifts as opposed to moderate redshifts ($0.1 \lesssim z \lesssim 0.5$)

for a fixed physical emission region. This property of interferometers implies that there is some optimal redshift range and optimal physical size over which to integrate a signal in radio studies of dark matter. Additionally, the frequency of the observation plays a role in sample selection: different observing frequencies probe different parts of the cosmic-ray electron spectrum produced by dark matter annihilation.

I plan to investigate the parameters of the optimal cluster sample for constraining dark matter using radio observations, with the goal of making predictions for constraints from the next generation of radio telescopes. In Figure 5.1, I show preliminary estimates of the cross section limits that can be achieved with new radio telescopes. In this figure, I compare the limits on the annihilation cross section derived in Chapter 3 for Coma, and the limits from a nondetection of a cluster with Apertif or ASKAP, with the same mass, magnetic field, and redshift of Coma. Here, a "nondetection" means a flux at the sensitivity threshold of the telescope (which happens to be about the same for Apertif and ASKAP, as predicted by Cassano et al. 2012). The factor of ~ 10 increase in in the limits for dark matter masses $10 - 1000$ GeV illustrates the power of new radio telescopes to constrain dark matter annihilation in clusters.

The lack of a detection of gamma-ray emission from *Fermi* has greatly pushed forward our understanding of nonthermal processes in galaxy clusters. At the opposite end of the spectrum, the next generation of radio telescopes will guide us towards even greater understanding. The next decade will be an exciting time for the study of nonthermal emission in galaxy clusters.

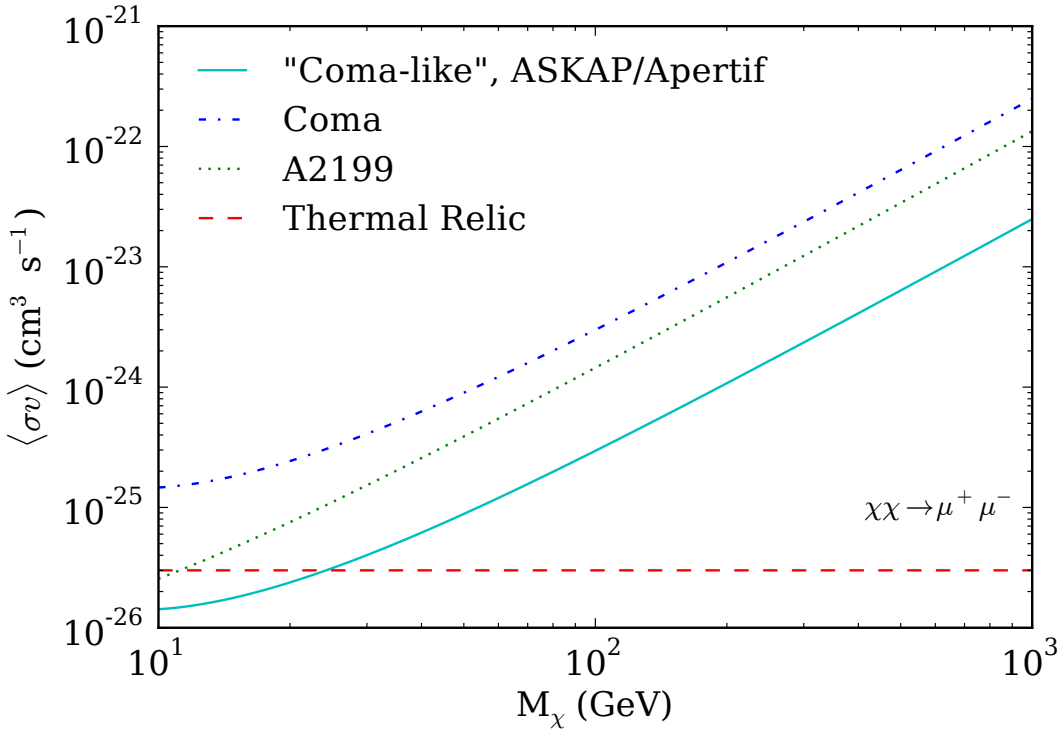

Figure 5.1: Limits on the cross section for dark matter annihilating to muons. The limits from Coma (blue) A2199 (green) are from (Storm et al. 2013), while the limits for the "Coma-like" (cyan) are those predicted based on nondetection of a cluster with Apertif or ASKAP at 1.4 GHz, with the same mass, magnetic field, and redshift of Coma. The red dashed line is the approximate cross section required to match the observed relic density of dark matter.

Bibliography

Abdo, A. A., Ackermann, M., Ajello, M., et al. 2009, Physical Review Letters, 103, 1

—. 2010a, Journal of Cosmology and Astroparticle Physics, 2010, 014

—. 2010b, The Astrophysical Journal, 709, L152

—. 2010c, Astronomy & Astrophysics, 523, A46

—. 2010d, Astronomy & Astrophysics, 523, L2

—. 2010e, Astronomy & Astrophysics, 512, A7

Abramowski, A., Acero, F., Aharonian, F., et al. 2012, The Astrophysical Journal, 750, 123

Acciari, V. A., Aliu, E., Arlen, T., et al. 2009, Nature, 462, 770

Acero, F., Aharonian, F., Akhperjanian, A. G., et al. 2009, Science, 326, 1080

Ackermann, F.-L. C. M., Ajello, M., Albert, A., et al. 2012a, Physical Review D, 86, 1

Ackermann, M., Ajello, M., Allafort, A., et al. 2010a, Journal of Cosmology and Astroparticle Physics, 2010, 025

—. 2010b, The Astrophysical Journal, 717, L71

Ackermann, M., Ajello, M., Albert, A., et al. 2011, Physical Review Letters, 107, 1

Ackermann, M., Ajello, M., Allafort, A., et al. 2012b, The Astrophysical Journal, 755, 164

Ackermann, M., Ajello, M., Albert, A., et al. 2013, Physical Review D, 88, 1

—. 2014, The Astrophysical Journal, 787, 18

Ackermann, M., Albert, A., Anderson, B., et al. 2015, ArXiv:1503.02641, 1

Actis, M., Agnetta, G., Aharonian, F., et al. 2011, Experimental Astronomy, 32, 193

Aharonian, F., Akhperjanian, A. G., Anton, G., et al. 2009a, Astronomy & Astrophysics, 502, 437

—. 2009b, Astronomy & Astrophysics, 495, 27

Aharonian, F., Arshakian, T. G., Allen, B., et al. 2013, ArXiv:1301.4124, 150

Ajello, M., Rebusco, P., Cappelluti, N., et al. 2009, The Astrophysical Journal, 690, 367

Aleksić, J., Antonelli, L. A., Antoranz, P., et al. 2010, The Astrophysical Journal, 710, 634

Aleksić, J., Alvarez, E. a., Antonelli, L. a., et al. 2012, Astronomy & Astrophysics, 541, A99

Ando, S., & Nagai, D. 2012, Journal of Cosmology and Astroparticle Physics, 2012, 017

Arlen, T., Aune, T., Beilicke, M., et al. 2012, The Astrophysical Journal, 757, 123

Ascasibar, Y., & Markevitch, M. 2006, The Astrophysical Journal, 650, 102

Bai, L., Rieke, G. H., Rieke, M. J., et al. 2006, The Astrophysical Journal, 639, 827

Baldi, A., Forman, W., Jones, C., et al. 2009, The Astrophysical Journal, 707, 1034

Beck, R., & Krause, M. 2005, Astronomische Nachrichten, 326, 414

Berezinsky, V. S., Blasi, P., & Ptuskin, V. S. 1997, The Astrophysical Journal, 487, 529

Bertone, G., Hooper, D., & Silk, J. 2005, Physics Reports, 405, 279

Blanton, E. L., Sarazin, C. L., McNamara, B. R., & Wise, M. W. 2001, The Astrophysical Journal, 558, L15

Blasi, P., & Colafrancesco, S. 1999, Astroparticle Physics, 12, 169

Blasi, P., Gabici, S., & Brunetti, G. 2007, International Journal of Modern Physics A, 22, 681

Bonafede, A., Feretti, L., Murgia, M., et al. 2010, Astronomy and Astrophysics, 513, A30

Bonafede, A., Intema, H. T., Bruggen, M., et al. 2014, Monthly Notices of the Royal Astronomical Society: Letters, 444, L44

Book, L. G., & Benson, A. J. 2010, The Astrophysical Journal, 716, 810

Bringmann, T., Huang, X., Ibarra, A., Vogl, S., & Weniger, C. 2012, Journal of Cosmology and Astroparticle Physics, 2012, 054

Bringmann, T., Vollmann, M., & Weniger, C. 2014, Physical Review D, 90, 22

Brown, M. J. I., Jannuzi, B. T., Floyd, D. J. E., & Mould, J. R. 2011a, The Astrophysical Journal, 731, L41

Brown, S., Emerick, A., Rudnick, L., & Brunetti, G. 2011b, The Astrophysical Journal, 740, L28

Brown, S., & Rudnick, L. 2011, Monthly Notices of the Royal Astronomical Society, 412, 2

Brunetti, G., Blasi, P., Cassano, R., & Gabici, S. 2004, Monthly Notices of the Royal Astronomical Society, 350, 1174

Brunetti, G., Blasi, P., Reimer, O., et al. 2012, Monthly Notices of the Royal Astronomical Society, 426, 956

Brunetti, G., Cassano, R., Dolag, K., & Setti, G. 2009, Astronomy and Astrophysics, 507, 661

Brunetti, G., & Jones, T. W. 2014, International Journal of Modern Physics D, 23, 1430007

Brunetti, G., & Lazarian, A. 2007, Monthly Notices of the Royal Astronomical Society, 378, 245

—. 2011a, Monthly Notices of the Royal Astronomical Society, 410, 127

—. 2011b, Monthly Notices of the Royal Astronomical Society, 412, 817

Brunetti, G., Setti, G., Feretti, L., & Giovannini, G. 2001, Monthly Notices of the Royal Astronomical Society, 320, 365

Bryan, G. L., & Norman, M. L. 1998, The Astrophysical Journal, 495, 80

Buote, D. A. 2001, The Astrophysical Journal, 553, L15

Buote, D. A., Gastaldello, F., Humphrey, P. J., et al. 2007, The Astrophysical Journal, 664, 123

Carilli, C. L., & Taylor, G. B. 2002, Annual Review of Astronomy and Astro-

physics, 40, 319

Cassano, R., Brunetti, G., Norris, R. P., et al. 2012, Astronomy & Astrophysics, 548, A100

Cassano, R., Brunetti, G., Röttgering, H. J. A., & Brüggen, M. 2009, Astronomy and Astrophysics, 509, A68

Cassano, R., Brunetti, G., & Setti, G. 2006, Monthly Notices of the Royal Astronomical Society, 369, 1577

Cassano, R., Brunetti, G., & Venturi, T. 2011, Journal of Astrophysics & Astronomy, 32, 519

Cassano, R., Ettori, S., Giacintucci, S., et al. 2010, The Astrophysical Journal, 721, L82

Cassano, R., Ettori, S., Brunetti, G., et al. 2013, The Astrophysical Journal, 777, 141

Cavagnolo, K. W., Donahue, M., Voit, G. M., & Sun, M. 2009, The Astrophysical Journal Supplement Series, 182, 12

Cavaliere, A., & Fusco-Femiano, R. 1976, Astronomy & Astrophysics, 49, 137

Chen, Y., Reiprich, T. H., Böhringer, H., Ikebe, Y., & Zhang, Y.-Y. 2007, Astronomy and Astrophysics, 466, 805

Chung, S. M., Eisenhardt, P. R., Gonzalez, A. H., et al. 2011, The Astrophysical Journal, 743, 34

Chung, S. M., Gonzalez, A. H., Clowe, D., Markevitch, M., & Zaritsky, D. 2010, The Astrophysical Journal, 725, 1536

Clarke, T. E., Blanton, E. L., & Sarazin, C. L. 2004, The Astrophysical Journal, 616, 178

Clarke, T. E., Kronberg, P., & Bohringer, H. 2001, The Astrophysical Journal, 547, L111

Clowe, D., Bradac, M., Gonzalez, A. H., et al. 2006, The Astrophysical Journal, 648, L109

Colafrancesco, S., & Marchegiani, P. 2009, Astronomy and Astrophysics, 502, 711

Colafrancesco, S., Profumo, S., & Ullio, P. 2006, Astronomy and Astrophysics, 455, 21

—. 2007, Physical Review D - Particles, Fields, Gravitation and Cosmology, 75, 1

Condon, J. J. 1992, Annual Review of Astronomy and Astrophysics, 30, 575

Condon, J. J., Cotton, W. D., Greisen, E. W., et al. 1998, The Astronomical Journal, 115, 1693

Coppin, K. E. K., Geach, J. E., Smail, I., et al. 2011, Monthly Notices of the Royal Astronomical Society, 416, 680

Dale, D. a., & Helou, G. 2002, The Astrophysical Journal, 576, 159

Davies, J. I., Baes, M., Bendo, G. J., et al. 2010, Astronomy & Astrophysics, 518, L48

Dennison, B. 1980, The Astrophysical Journal, 239, L93

Dirsch, B., Schuberth, Y., & Richtler, T. 2005, Astronomy and Astrophysics, 433, 43

Dolag, K., Bartelmann, M., & Lesch, H. 2002, Astronomy and Astrophysics, 387, 383

Dolag, K., Schindler, S., Govoni, F., & Feretti, L. 2001, Astronomy and Astrophysics, 378, 777

Donnert, J., Dolag, K., Brunetti, G., & Cassano, R. 2013, Monthly Notices of the Royal Astronomical Society, 429, 3564

Donnert, J., Dolag, K., Lesch, H., & Müller, E. 2009, Monthly Notices of the Royal Astronomical Society, 392, 1008

Doria, A., Gitti, M., Ettori, S., et al. 2012, The Astrophysical Journal, 753, 47

Dugger, L., Jeltema, T. E., & Profumo, S. 2010, Journal of Cosmology and Astroparticle Physics, 2010, 015

Dunn, R. J. H., Allen, S. W., Taylor, G. B., et al. 2010, Monthly Notices of the Royal Astronomical Society, 197, 180

Eckert, D., Produit, N., Paltani, S., Neronov, A., & Courvoisier, T. J.-L. 2008, Astronomy and Astrophysics, 479, 27

Egami, E., Misselt, K. a., Rieke, G. H., et al. 2006, The Astrophysical Journal, 647, 922

Eilek, J. A., & Owen, F. N. 2002, The Astrophysical Journal, 567, 202

Ensslin, T. A., Vogt, C., Clarke, T. E., & Taylor, G. B. 2003, The Astrophysical

Journal, 597, 870

Faber, S. M., & Dressler, A. 1977, The Astronomical Journal, 82, 187

Fabian, A. 1994, Annual Review of Astronomy and Astrophysics, 32, 277

Farnsworth, D., Rudnick, L., Brown, S., & Brunetti, G. 2013, The Astrophysical Journal, 779, 189

Feretti, L., Giovannini, G., & Böhringer, H. 1997, New Astronomy, 2, 501

Feretti, L., Giovannini, G., Govoni, F., & Murgia, M. 2012, The Astronomy and Astrophysics Review, 20, 54

Ferrari, C., Govoni, F., Schindler, S., Bykov, A. M., & Rephaeli, Y. 2008, Space Science Reviews, 134, 93

Fujita, Y., Hayashida, K., Nagai, M., et al. 2008, Publications of the Astronomical Society of Japan, 60, 1133

Gao, L., Frenk, C. S., Jenkins, A., Springel, V., & White, S. D. M. 2012a, Monthly Notices of the Royal Astronomical Society, 419, 1721

Gao, L., Navarro, J. F., Frenk, C. S., et al. 2012b, Monthly Notices of the Royal Astronomical Society, 425, 2169

Geringer-Sameth, A., & Koushiappas, S. 2012, Physical Review D, 86, 23

Geringer-Sameth, A., & Koushiappas, S. M. 2011, Physical Review Letters, 107, 1

Ghizzardi, S., Rossetti, M., & Molendi, S. 2010, Astronomy and Astrophysics, 516, A32

Giacintucci, S., Markevitch, M., Brunetti, G., et al. 2014a, The Astrophysical Journal, 795, 73

Giacintucci, S., Markevitch, M., Venturi, T., et al. 2014b, The Astrophysical Journal, 781, 9

Giacintucci, S., O'Sullivan, E., Vrtilek, J., et al. 2011, The Astrophysical Journal, 732, 95

Giovannini, G., Tordi, M., & Feretti, L. 1999, New Astronomy, 4, 141

Gitti, M., Brighenti, F., & McNamara, B. R. 2012, Advances in Astronomy, 2012, 1

Gondolo, P., Edsjö, J., Ullio, P., et al. 2004, Journal of Cosmology and Astropar-

ticle Physics, 2004, 008

Goto, T. 2005, Monthly Notices of the Royal Astronomical Society, 356, L6

Govoni, F., & Feretti, L. 2004, International Journal of Modern Physics D, 13, 1549

Govoni, F., Markevitch, M., Vikhlinin, A., et al. 2004, The Astrophysical Journal, 605, 695

Govoni, F., Dolag, K., Murgia, M., et al. 2010, Astronomy & Astrophysics, 522, A105

Green, A. M., Hofmann, S., & Schwarz, D. J. 2005, Journal of Cosmology and Astroparticle Physics, 2005, 003

Griffin, R. D., Dai, X., & Kochanek, C. S. 2014, The Astrophysical Journal, 795, L21

Han, J., Frenk, C. S., Eke, V. R., Gao, L., & White, S. D. M. 2012a, arXiv:1201.1003, 30

Han, J., Frenk, C. S., Eke, V. R., et al. 2012b, Monthly Notices of the Royal Astronomical Society, 427, 1651

Harris, D., & Miley, G. 1978, Astronomy & Astrophysics Supplement Series, 34, 117

Harvey, D., Massey, R., Kitching, T., Taylor, A., & Tittley, E. 2015, Science, 347, 1462

Hektor, A., Raidal, M., & Tempel, E. 2013, The Astrophysical Journal, 762, L22

Hooper, D., Belikov, A. V., Jeltema, T. E., et al. 2012, Physical Review D, 86, 103003

Hooper, D., & Linden, T. 2011, Physical Review D - Particles, Fields, Gravitation and Cosmology, 84, 1

Hooper, D., & Profumo, S. 2007, Physics Reports, 453, 29

Hu, W., & Kravtsov, A. V. 2003, The Astrophysical Journal, 584, 702

Huang, X., Vertongen, G., & Weniger, C. 2012, Journal of Cosmology and Astroparticle Physics, 2012, 042

Huber, B., Tchernin, C., Eckert, D., et al. 2013, Astronomy & Astrophysics, 560, A64

Hudson, D. S., Mittal, R., Reiprich, T. H., et al. 2010, Astronomy and Astrophysics, 513, A37

Jeltema, T., Kehayias, J., & Profumo, S. 2009, Physical Review D, 80, 023005

Jeltema, T. E., & Profumo, S. 2008, Journal of Cosmology and Astroparticle Physics, 2008, 003

—. 2011, The Astrophysical Journal, 728, 53

Johnston, S., Taylor, R., Bailes, M., et al. 2008, Experimental Astronomy, 22, 151

Jones, C., Forman, W., Vikhlinin, A., et al. 2002, The Astrophysical Journal, 567, L115

Jungman, G., Kamionkowski, M., & Griest, K. 1996, Physics Reports, 267, 195

Kennicutt, R. C. 1998, Annual Review in Astronomy and Astrophysics, 36, 189

Kim, K.-T., Kronberg, P. P., Dewdney, P. E., & Landecker, T. L. 1990, The Astrophysical Journal, 355, 29

Kuchar, P., & Enß lin, T. a. 2011, Astronomy & Astrophysics, 529, A13

Kuntz, K. D., & Snowden, S. L. 2008, Astronomy and Astrophysics, 478, 575

Kunz, M. W., Schekochihin, a. a., Cowley, S. C., Binney, J. J., & Sanders, J. S. 2011, Monthly Notices of the Royal Astronomical Society, 410, 2446

Laganá, T. F., Andrade-Santos, F., & Lima Neto, G. B. 2010, Astronomy and Astrophysics, 511, A15

Lenain, J.-P., Ricci, C., Türler, M., Dorner, D., & Walter, R. 2010, Astronomy & Astrophysics, 524, A72

Liang, H., Hunstead, R. W., Birkinshaw, M., & Andreani, P. 2000, The Astrophysical Journal, 544, 686

Linden, T., Hooper, D., & Yusef-Zadeh, F. 2011, The Astrophysical Journal, 741, 95

Longair, M. S. 2011, High Energy Astrophysics, 3rd edn. (Cambridge University Press)

Macías-Ramírez, O., Gordon, C., Brown, A. M., & Adams, J. 2012, Physical Review D, 86, 5

Markevitch, M. 1996, The Astrophysical Journal, 465, L1

Markevitch, M., & Vikhlinin, A. 2007, Physics Reports, 443, 1

Martig, M., & Bournaud, F. 2008, Monthly Notices of the Royal Astronomical Society: Letters, 385, L38

McDonald, M., Veilleux, S., Rupke, D. S. N., Mushotzky, R., & Reynolds, C. 2011, The Astrophysical Journal, 734, 95

Miller, N. A., Hornschemeier, A. E., Mobasher, B., et al. 2009, The Astronomical Journal, 137, 4450

Molendi, S., De Grandi, S., Fusco-Femiano, R., et al. 1999, The Astrophysical Journal, 525, L73

Molendi, S., & Pizzolato, F. 2001, The Astrophysical Journal, 560, 194

Murgia, M., Eckert, D., Govoni, F., et al. 2010, Astronomy and Astrophysics, 514, A76

Murgia, M., Govoni, F., Feretti, L., et al. 2004, Astronomy and Astrophysics, 424, 429

Murgia, M., Govoni, F., Markevitch, M., et al. 2009, Astronomy and Astrophysics, 499, 679

Nagai, D., & Kravtsov, A. V. 2005, The Astrophysical Journal, 618, 557

Navarro, J. F., Frenk, C. S., & White, S. D. M. 1996, The Astrophysical Journal, 462, 563

—. 1997, The Astrophysical Journal, 490, 493

Nevalainen, J., Eckert, D., Kaastra, J., Bonamente, M., & Kettula, K. 2009, Astronomy and Astrophysics, 508, 1161

Nezri, E., White, R., Combet, C., et al. 2012, Monthly Notices of the Royal Astronomical Society, 425, 477

Noutsos, A. 2012, Space Science Reviews, 166, 307

Oegerle, W. R., Hill, J. M., & Fitchett, M. J. 1995, The Astronomical Journal, 110, 32

O'Hara, T. B., Mohr, J. J., Bialek, J. J., & Evrard, A. E. 2006, The Astrophysical Journal, 639, 64

O'Hara, T. B., Mohr, J. J., & Guerrero, M. A. 2004, The Astrophysical Journal, 604, 604

Pérez-Torres, M. a., Zandanel, F., Guerrero, M. a., et al. 2009, Monthly Notices

of the Royal Astronomical Society, 396, 2237

Petrosian, V. 2001, The Astrophysical Journal, 557, 560

Pfrommer, C. 2008, Monthly Notices of the Royal Astronomical Society, 385, 1242

Pinzke, A., & Pfrommer, C. 2010, Monthly Notices of the Royal Astronomical Society, 409, 449

Poole, G. B., Fardal, M. a., Babul, a., et al. 2006, Monthly Notices of the Royal Astronomical Society, 373, 881

Profumo, S. 2008, Physical Review D, 77, 1

Profumo, S., Sigurdson, K., & Kamionkowski, M. 2006, Physical Review Letters, 97, 1

Reddy, N. a., & Yun, M. S. 2004, The Astrophysical Journal, 600, 695

Reiprich, T. H., & Bohringer, H. 2002, The Astrophysical Journal, 567, 716

Ricker, P. M., & Sarazin, C. L. 2001, The Astrophysical Journal, 561, 621

Rieke, G. H., Alonso-Herrero, a., Weiner, B. J., et al. 2009, The Astrophysical Journal, 692, 556

Roediger, E., Lovisari, L., Dupke, R., et al. 2012, Monthly Notices of the Royal Astronomical Society, 420, 3632

Rossetti, M., Eckert, D., De Grandi, S., et al. 2013, Astronomy & Astrophysics, 556, A44

Rubin, V. C., & Ford, W. Kent, J. 1970, The Astrophysical Journal, 159, 379

Rudaz, S., & Stecker, F. W. 1991, The Astrophysical Journal, 368, 406

Rudnick, L., & Blundell, K. M. 2003, The Astrophysical Journal, 588, 143

Rudnick, L., & Lemmerman, J. a. 2009, The Astrophysical Journal, 697, 1341

Ryu, D., Kang, H., Cho, J., & Das, S. 2008, Science (New York, N.Y.), 320, 909

Sanders, D. B., & Mirabel, I. F. 1996, Annual Review of Astronomy and Astrophysics, 34, 749

Santos, J. S., Rosati, P., Tozzi, P., et al. 2008, Astronomy and Astrophysics, 483, 35

Sarazin, C. 1986, Reviews of Modern Physics, 58, 1

Siffert, B. B., Limone, A., Borriello, E., Longo, G., & Miele, G. 2011, Monthly Notices of the Royal Astronomical Society, 410, 2463

Snowden, S. L., Mushotzky, R. F., Kuntz, K. D., & Davis, D. S. 2008, Astronomy and Astrophysics, 478, 615

Spekkens, K., Mason, B. S., Aguirre, J. E., & Nhan, B. 2013, The Astrophysical Journal, 773, 61

Springel, V., White, S. D. M., Jenkins, A., et al. 2005, Nature, 435, 629

Storm, E., Jeltema, T. E., Profumo, S., & Rudnick, L. 2013, The Astrophysical Journal, 768, 106

Storm, E., Jeltema, T. E., & Rudnick, L. 2015, Monthly Notices of the Royal Astronomical Society, 448, 2495

Struble, M. F., & Rood, H. J. 1999, The Astrophysical Journal Supplement Series, 125, 35

Subramanian, K., Shukurov, A., & Haugen, N. E. L. 2006, Monthly Notices of the Royal Astronomical Society, 366, 1437

Sugawara, C., Takizawa, M., & Nakazawa, K. 2009, Publications of the Astronomical Society of Japan, 61, 1293

Taylor, G., Barton, E., & Ge, J. 1994, The Astronomical Journal, 107, 1942

Taylor, G. B., Fabian, A. C., & Allen, S. W. 2002, Monthly Notices of the Royal Astronomical Society, 334, 769

Taylor, G. B., Gugliucci, N. E., Fabian, a. C., et al. 2006, Monthly Notices of the Royal Astronomical Society, 368, 1500

Totani, T. 2004, Physical Review Letters, 92, 12

Vacca, V., Murgia, M., Govoni, F., et al. 2012, Astronomy & Astrophysics, 540, A38

van Haarlem, M. P., Wise, M. W., Gunst, A. W., et al. 2013, Astronomy & Astrophysics, 556, A2

Venturi, T., Giacintucci, S., Brunetti, G., et al. 2007, Astronomy & Astrophysics, 463, 937

Venturi, T., Giacintucci, S., Dallacasa, D., et al. 2008, Astronomy & Astrophysics, 484, 327

Verheijen, M. A. W., Oosterloo, T. A., van Cappellen, W. A., et al. 2008, AIP Conference Proceedings, 1035, 265

Villegas, D., Jordán, A., Peng, E. W., et al. 2010, The Astrophysical Journal, 717, 603

Völk, H. 1989, Astronomy & Astrophysics, 218, 67

Volk, H., Aharonian, F., & Breitschwerdt, D. 1996, Space Science Reviews, 75

Vollmer, B., Soida, M., Chung, A., et al. 2008, Astronomy & Astrophysics, 483, 89

Weniger, C. 2012, Journal of Cosmology and Astroparticle Physics, 2012, 007

Wik, D. R., Sarazin, C. L., Zhang, Y.-Y., et al. 2012, The Astrophysical Journal, 748, 67

Wik, D. R., Hornstrup, A., Molendi, S., et al. 2014, The Astrophysical Journal, 792, 48

Yan, P.-F., Yuan, Q.-R., Zhang, L., & Zhou, X. 2014, The Astronomical Journal, 147, 106

Yun, M. I. N. S., Reddy, N. A., & Condon, J. J. 2001, The Astrophysical Journal, 554, 803

ZuHone, J. a., Markevitch, M., Ruszkowski, M., & Lee, D. 2013, The Astrophysical Journal, 762, 69

Zwicky, F. 1933, Helvetica Physica Acta, 6, 110